

# **Morphology and Morphology Formation of Injection Molded PP-based Nanocomposites**

Von Fachbereich Maschinenbau und Verfahrenstechnik  
der Technischen Universität Kaiserslautern  
zur Verleihung des akademischen Grades

**Doktor-Ingenieur (Dr.-Ing.)**

genehmigte

**Dissertation**

von

Herrn

**M.Eng. Buncha Suksut**

aus Nakhon Ratchasima, Thailand

Tag der Einreichung:	20 April 2016
Tag der mündlichen Prüfung:	24 Juni 2016
Hauptreferent:	Prof. Dr.-Ing. Alois K. Schlarb
Korreferent:	Prof. Dr.-Ing. Volker Altstädt
Prüfungsvorsitzender:	Prof. Dr.-Ing. Martin Böhle
Dekan:	Prof. Dr.-Ing. Jörg Seewig

Kaiserslautern 2016

**D 386**

## **Acknowledgement**

This dissertation is the result of my four years of work in the Chair of Composite Engineering (CCe, Fachbereichs Maschinenbau und Verfahrenstechnik) at University of Kaiserslautern, Germany with the support of many people.

I would like to express my deep gratitude to Prof. Dr.-Ing. Alois K. Schlarb for giving me the opportunity of PhD studies under his supervision, and the trust he placed in me. The success of this work was impossible without his extensive supports, encouragements, knowledge, and experiences.

I would also like to thank all members of CCe. Special thanks are also extended to Dr. Leyu Lin for his valuable suggestion and guidance throughout the period of my study.

Many thanks to Dr. Lösch, Mr. Reuscher, and Ms. Zeuner from IFOS Kaiserslautern, Dr. Wolff from NSC Kaiserslautern for their help in SEM measurements, Mr. Maurer and Mr. Hubertus from INM Saarbrücken, Mr. Kornpanom from Chulalongkorn Bangkok for their support in WAXD/SAXS measurements as well as my students for their help in some experiments.

I would like to convey my heartfelt thanks to all my friends in Thailand for their constant support and encouragement particularly Aods and Aof.

Finally, I would like to express my deep sense of gratitude to my parents for their support and encouragement filled with love and affection inspired me throughout the course of this study.



## Table of Contents

<b>Table of Contents.....</b>	<b>I</b>
<b>Abstract.....</b>	<b>IV</b>
<b>Kurzfassung.....</b>	<b>V</b>
<b>List of Abbreviations and Symbols.....</b>	<b>VIII</b>
<b>1. Introduction.....</b>	<b>1</b>
<b>2. State of the Art.....</b>	<b>3</b>
2.1 Polymer Nanocomposites.....	3
2.2 Polypropylene Nanocomposites.....	4
2.2.1 Polypropylene.....	4
2.2.2 Particulate-Filled Polypropylene.....	5
2.2.3 Crystallization Effects of Nanoparticle-Filled Polypropylene.....	8
2.3 Polymer Crystallization.....	9
2.3.1 Structure Development and Crystallization in Injection Molding.....	14
2.3.2 Quiescent Crystallization.....	15
2.3.3 Morphology of Injection Molded Sample.....	21
2.4 Polymer Deformation in Term of Spherulites.....	25
<b>3. Objective of the Study.....</b>	<b>29</b>
<b>4. Experimental Procedures.....</b>	<b>30</b>
4.1 Materials.....	30

---

4.1.1	Polypropylene.....	30
4.1.2	Nanofillers.....	30
4.2	Preparation of Nanocomposites.....	31
4.2.1	Extrusion.....	31
4.2.2	Injection Molding.....	32
4.3	Preparation of Testing Specimens.....	32
4.3.1	Thin Sections.....	33
4.3.2	Etched Specimens.....	34
4.3.3	Ion-polished Specimens.....	35
4.3.4	Fractured Surfaces.....	35
4.4	Simulation of Injection Molding.....	35
4.5	Characterization of the Morphological Structure.....	36
4.5.1	Optical Microscopy.....	36
4.5.2	Electron Scanning Microscopy.....	37
4.5.3	X-Ray Analysis.....	37
4.6	Characterization of the Crystallization.....	38
4.6.1	Polarized Light Microscope Equipped with Heating Stage.....	38
4.6.2	Differential Scanning Calorimetry.....	39
4.6.3	Flash Differential Scanning Calorimetry.....	41
4.7	Characterization of the Mechanical Properties.....	42
<b>5.</b>	<b>Results and Discussion.....</b>	<b>43</b>
5.1	Simulation of Injection Molding.....	43
5.2	Quiescent Crystallization Kinetics.....	45
5.2.1	Isothermal Crystallization Analysis.....	45
5.2.2	Non-Isothermal Crystallization Analysis.....	56
5.2.3	Melting Behaviors and Recrystallization during Heating.....	64

---

5.2.4 Spherulitic Development.....	67
5.3 Morphology of Injection Molded Samples.....	70
5.3.1 Skin-Core Morphology.....	70
5.3.2 Distribution of Spherulite Size.....	73
5.3.3 Distribution of Lamellar Morphology.....	78
5.3.4 Distribution of Nanoparticles.....	81
5.3.5 Distribution of the Nanoparticle Orientation.....	84
5.3.6 Distribution of Crystallinity.....	86
5.3.7 Distribution of Spherulite Form.....	87
5.3.8 Distribution of Lamellar Thickness.....	88
5.4 Deformation Behaviors.....	91
5.4.1 Tensile Properties.....	91
5.4.2 Spherulitic Deformation.....	95
<b>6. Summary.....</b>	<b>100</b>
<b>7. References.....</b>	<b>102</b>
<b>List of Publications.....</b>	<b>123</b>
<b>Appendix.....</b>	<b>126</b>
<b>Curriculum Vitae .....</b>	<b>134</b>

## Abstract

The mechanical properties of semi-crystalline polymers depend extremely on their morphology, which is dependent on the crystallization during processing. The aim of this research is to determine the effect of various nanoparticles on morphology formation and tensile mechanical properties of polypropylene under conditions relevant in polymer processing and to contribute ultimately to the understanding of this influence.

Based on the thermal analyses of samples during fast cooling, it is found that the presence of nanoparticle enhances the overall crystallization process of PP. The results suggest that an increase of the nucleation density/rate is a dominant process that controls the crystallization process of PP in this work, which can help to reduce the cycle time in the injection process. Moreover, the analysis of melting behaviors obtained after each undercooling reveals that crystal perfection increases significantly with the incorporation of  $\text{TiO}_2$  nanoparticles, while it is not influenced by the  $\text{SiO}_2$  nanoparticles.

This work also comprises an analysis of the influence of nanoparticles on the microstructure of injection-molded parts. The results clearly show multi-layers along the wall thickness. The spherulite size and the degree of crystallinity continuously decrease from the center to the edge. Generally both the spherulite size and the degree of crystallinity decrease with higher the  $\text{SiO}_2$  loading. In contrast, an increase in the degree of crystallinity with an increasing  $\text{TiO}_2$  nanoparticle loading was detected.

The tensile properties exhibit a tendency to increase in the tensile strength as the core is reached. The tensile strength decreases with the addition of nanoparticles, while the elongation at break of nanoparticle-filled PP decreases from the skin to the core. With increasing  $\text{TiO}_2$  loading, the elongation at break decreases.

## Kurzfassung

Die mechanischen Eigenschaften von thermoplastischen teilkristallinen Kunststoffen sind stark an ihre Morphologie gekoppelt, welche wiederum von der Orientierung der Makromoleküle, den Eigenspannungen und insbesondere von der supermolekularen Struktur, erzeugt durch die Kristallisation während der Verarbeitung abhängt.

Ziel dieser Untersuchung ist, den Einfluss verschiedener Nanopartikel auf die Morphologie und Morphologiebildung und lokale mechanische Eigenschaften von Polypropylen zu untersuchen. Das Hauptaugenmerk der Arbeit liegt dabei auf der Untersuchung von Proben, die unter praxisrelevanten Bedingungen hergestellt wurden. Daher wurde ein Großteil der Untersuchungen an spritzgegossenen Probekörpern oder an im Labor unter praxisrelevanten Abkühlbedingungen hergestellten Proben vorgenommen. Die Untersuchungen sollen letztendlich dazu beitragen den Zusammenhang zwischen praxisrelevanter Verarbeitung, Morphologie und Eigenschaften für die Klasse der polymerbasierten teilkristallinen Nanokomposite exemplarisch aufzuklären und letztendlich besser verstehen zu können.

Untersucht wurde Polypropylen gefüllt mit unterschiedlichen Gehalten an nanoskaligem Siliziumdioxid  $\text{SiO}_2$  als Beispiel für einen sphärischen Partikel und Titandioxid  $\text{TiO}_2$ , beispielhaft für einen nadelförmigen Partikeln. Diese wurden in einem zweistufigen Extrusionsverfahren in einem Doppelschneckenextruder compoundiert und anschließend zu Platten mit einer Wandstärke von 4 mm spritzgegossen. Der Einfluss der Nanopartikel auf Kristallisation, Morphologie und ausgewählte mechanische Eigenschaften wurden weitreichend untersucht. Mittels dynamischer Differenzkalorimetrie (Differential Scanning Calorimetry, DSC) wurden charakteristische Umwandlungstemperaturen sowie die Kristallisationsgrade bei unterschiedlichen Abkühlgeschwindigkeiten, insbesondere auch bei hohen Abkühlgeschwindigkeiten mittels Flash-DSC, untersucht. Lichtmikroskopie, Elektronenmikroskopie sowie Groß- und Kleinwinkelröntgenstreuung wurden für die Bestimmung der Morphologie verwendet, während Mikrozugversuche zur Bestimmung der schichtweisen – und damit morphologieabhängigen – Eigenschaften durchgeführt wurden. Darüber hinaus wurden

mittels Heiztisch und Durchlichtmikroskopie Untersuchungen bei isothermen und nicht-isothermen Abkühlbedingungen durchgeführt.

Mittels des Programmpakets Moldflow wurden Füllsimulationen unter unterschiedlichen Randbedingungen durchgeführt. Dadurch konnten praxisrelevante Abkühlgeschwindigkeiten über die Wandstärke der spritzgegossenen Probekörper bestimmt werden. Diese Geschwindigkeiten liegen in einem Bereich von bis zu 0,8 mm neben der Werkzeugwand zwischen 1 K/s bis 2800 K/s und damit weit oberhalb der Abkühlgeschwindigkeiten, die mit einer Standard-DSC untersucht werden können. Aus diesem Grund kam für diese Untersuchungen auch eine Flash-DSC zum Einsatz.

Anhand der DSC-Untersuchungen konnten abhängig von der Abkühlgeschwindigkeit verschiedene Morphologien in den Materialien nachgewiesen werden. Bei reinem Polypropylen sowie bei SiO<sub>2</sub>-gefülltem PP bildet sich die  $\alpha$ -Phase bei Abkühlgeschwindigkeiten von 0,03 K/s bis 700 K/s aus. Bei Abkühlgeschwindigkeiten kleiner 1 K/s bilden sich zudem eine  $\beta$ -Struktur aus. Bei Geschwindigkeiten zwischen 100 K/s bis 700 K/s ist thermoanalytisch zudem eine Mesophase nachweisbar. Oberhalb 700 K/s ist keine Kristallisation mehr feststellbar. TiO<sub>2</sub>-gefülltes Polypropylen kristallisiert dagegen in einem weiten Abkühlgeschwindigkeitsbereich zwischen 0,03 K/s bis 2500 K/s ausschließlich in der  $\alpha$ -Form. Isotherme Untersuchungen bestätigen, dass bei hohen Kristallisationstemperaturen eine heterogene Keimbildung den Kristallisationsprozess dominiert, wobei bei niedrigen Temperaturen die  $\beta$ -Struktur dominiert werden, während bei niedrigen Temperaturen materialabhängig die homogene Keimbildung (mesophase) kristallisationsbestimmend ist.

Beim erneuten Aufschmelzen von zuvor bei unterschiedlichen Abkühlgeschwindigkeiten kristallisierten Proben zeigt sich, dass ausschließlich TiO<sub>2</sub>-Nanopartikel zu höheren Schmelztemperaturen führen, was auf eine perfektere Kristallisation schließen lässt. SiO<sub>2</sub>-Nanopartikel zeigen diesen Einfluss nicht.

Untersuchungen der Sphärolithbildung im Heiztisch unter dem Polarisationsmikroskop bestätigen, dass nicht Wachstum den Kristallisationsprozess aller untersuchten Materialien bestimmt, sondern vorrangig die Dichte und Geschwindigkeit der Nukleierung. Insgesamt führt dies jedoch zu einer schnelleren Kristallisation, was

gegebenenfalls die Entformungszeit reduziert und somit Potenziale zur Zykluszeitverkürzung in der Praxis aufzeigt.

Außerdem wird der Einfluss von Nanopartikeln auf die Mikrostruktur von Spritzgussteilen untersucht. Es konnte eine Mehrschichtstruktur entlang der Wandstärke gezeigt werden. Die relative Dicke des Bereichs hoher Orientierung nimmt mit der Zugabe von Nanopartikeln zu. Sphärolithgröße und Kristallisationsgrad nehmen vom Zentrum zur Formteiwand kontinuierlich ab. Beide nehmen ebenfalls mit zunehmendem SiO<sub>2</sub>-Gehalt ab. Im Gegensatz dazu nimmt der Kristallisationsgrad mit dem Gehalt an TiO<sub>2</sub>-Nanopartikeln zu.

Aufgrund der hohen Scherungen und der hohen Abkühlgeschwindigkeit ist die Bildung der  $\beta$ -Phase der PP-Sphärolithe entlang der Wand unterdrückt, wohingegen sie im Kern deutlich sichtbar ist. Die hohen Scherungen haben auch Auswirkungen auf die Verteilung und die Orientierung der Nanopartikel über die Wandstärke. Im Kern ist die Konzentration an Nanopartikeln höher als zur Wand hin. Darüber hinaus sind die Nanopartikel im Kern zufällig orientiert, wohingegen sie an der Wand in Fließrichtung orientiert sind.

Die Mikrozugversuche zeigen, dass die Morphologie tatsächlich das mechanische Verhalten bestimmt. Unterschiedliche Schichten über die Wandstärke mit unterschiedlicher supermolekularer Struktur zeigen insbesondere Unterschiede in der Zugfestigkeit als auch in ihren Deformationsverhalten. Bei ungefüllten Polypropylen nimmt die Zugfestigkeit von der die Werkzeugwand kontaktierenden Schicht in Richtung Kern zu. Dies ist auf den höheren Kristallisationsgrad und eine größere Sphärolithgröße von Rand zum Zentrum der Proben zurückzuführen. Bei PP-Nanokompositen nimmt die Zugfestigkeit mit der Zugabe von Nanopartikeln abgrundsätzlich ab. Der Trend von Rand zur Mitte der Wand bleibt aber identisch.

Bei reinem Polypropylen treten erste Risse und letztendlich das Versagen der Proben vorzugsweise im Sphärolithzentrum und an den Sphärolithgrenzen auf. Bei gefüllten Polypropylen wird das Versagen bevorzugt an der Partikel/Matrix-Grenzfläche eingeleitet. Statistisch verteilt sind aber auch Risse an den Sphärolithgrenzen und in den Zentren der Sphärolithe erkennbar.

## List of Abbreviations and Symbols

### Abbreviations

CaCO <sub>3</sub>	Calcium carbonate
DSC	Differential scanning calorimetry
G	Growth rate
PA	Polyamide
PP	Polypropylene
SAXS	Small-angle X-ray scattering
SEM	Scanning electron microscopy
SiO <sub>2</sub>	Silica dioxide
TA	Thermo-analytical
TiO <sub>2</sub>	Titanium dioxide
WAXD	Wide-Angle X-Ray Diffraction

### Symbols

$A$	[m <sup>2</sup> ]	Surface area
$b_0$	[m]	Layer thickness
$\sigma$	[J/m <sup>2</sup> ]	Layer surface free energy
$\sigma_e$	[mJ/m <sup>2</sup> ]	Fold surface free energy
$C_0$	[-]	Malkin exponent
$C_1$	[-]	Malkin crystallization rate coefficient
$G_0$	[-]	Pre-exponential factor
$G_{crystal}$	[J]	Free enthalpies of the crystal
$G_{melt}$	[J]	Free enthalpies of the melt
$G_{PP}$	[μm/s]	Growth rate of neat PP

$G_{\text{nPP}}$	[ $\mu\text{m/s}$ ]	Growth rate of spherulite PP in a nanocomposite
$I_i(s)$	[a.u.]	Intensity
$k_a$	[-]	Avrami Isothermal rate constant of crystallization
$k_B$	[J/K]	Boltzmann's constant
$k_t$	[-]	Tobin Isothermal rate constant of crystallization
$K_g$	[K <sup>2</sup> ]	Nucleation parameter
$L$	[nm]	Long period of oriented semi-crystalline polymer
$l_c$	[nm]	Thickness of crystalline lamellar
$n_a$	[-]	Avrami exponent
$n_t$	[-]	Tobin exponent
$q$	[ $\text{\AA}$ ]	Scattering vector
$R$	[J/(mol K)]	Gas constant
$X_c$	[%]	Degree of crystallinity
$X(t)$	[-]	Time-dependent relative crystallinity
$T_{\text{cc},\alpha}$	[ $^{\circ}\text{C}$ ]	Cold-crystallization of $\alpha$ -phase
$T_{\text{cc},\text{m}}$	[ $^{\circ}\text{C}$ ]	Cold-crystallization of mesophase
$T_g$	[ $^{\circ}\text{C}$ ]	Glass transition temperature
$T_i$	[ $^{\circ}\text{C}$ ]	Isothermal crystallization temperature
$T_m$	[ $^{\circ}\text{C}$ ]	Melting temperature
$T_{m,\alpha}$	[ $^{\circ}\text{C}$ ]	Melting point of the $\alpha$ -phase
$T_{m,\beta}$	[ $^{\circ}\text{C}$ ]	Melting temperature of the $\beta$ -phase
$T_m^0$	[ $^{\circ}\text{C}$ ]	Equilibrium melting temperature
$T_p$	[ $^{\circ}\text{C}$ ]	Peak of crystallization temperature
$T_{\infty}$	[ $^{\circ}\text{C}$ ]	Theoretical temperature at which all motion associated with viscous flow ceases
$t_{1/2}$	[s]	Crystallization half-time
$U^*$	[J/mol]	Transport activation energy

$v_f$	[%]	Volume percentage of filler loading
$f$	[-]	Correction factor related to temperature
$\Delta E$	[kJ/mol]	Crystallization activation energies
$\Delta G$	[J]	Gibbs free energy
$\Delta G_c$	[J]	Bulk free energy change
$\Delta H$	[J]	Enthalpy of crystallization
$\Delta S$	[J/K]	Entropy of crystallization
$\Delta h_f$	[J/m <sup>3</sup> ]	Heat of fusion per unit volume of crystal
$\Delta T$	[°C]	Degree of supercooling
$\phi$	[K/s]	Cooling rate
$\beta$	[-]	Stability parameter
$B$	[-]	Parameter during homogeneous nucleation
$B^*$	[-]	Parameter during heterogeneous nucleation
$\gamma$	[J/m <sup>2</sup> ]	Specific surface free energy

## 1. Introduction

In recent years, nanocomposites have emerged as a new type of composite materials. Increased attention has been paid to polymer nanocomposites because of their remarkable property improvements when compared to conventional polymers [1]. Normally, filler particles affect the final mechanical properties in two ways: reinforcement and crystallization. The former usually depends on the shape, primary particle size, aggregate size and the modulus of the fillers [2, 3]. The latter relies on the primary size of the particles, surface modification, shape and concentration of the fillers [3].

Due to its most widely used and fastest growing classes of thermoplastic polymers in numerous industries, polypropylene (PP) is of high interest. It exhibits a good balanced between physical and mechanical properties as well as easy processability at a relatively low cost. However, the use of PP is still limited by its comparatively low modulus and stiffness in comparison with engineering plastics [4]. To overcome these limitations, one of most useful methods is the incorporation of reinforcing fillers such as glass, carbon, and aramid fibers as well as natural fibers [5] to enhance the properties of polymeric materials. Research also has been investigated the use of inorganic nanoparticles such as calcium carbonate ( $\text{CaCO}_3$ ) [2], titania ( $\text{TiO}_2$ ) [6], and silica ( $\text{SiO}_2$ ) [7] to improve mechanical and functional properties of plastics. The mechanical properties such as impact strength, elastic modulus and tensile strength increased with increasing nanoparticle loading with the properties reaching a maximum for loadings of either 9.2 vol.% for  $\text{CaCO}_3$ , 1.38 vol.% for  $\text{TiO}_2$  or 1.36 vol.% for  $\text{SiO}_2$ .

In general, the final properties of products produced from semi-crystalline polymers are highly depending on the morphological structure. As it is well-known, the morphology of such products is governed by the respective crystallization process during the production [8]. Therefore, knowledge of the microstructure and a good understanding of the crystallization behavior can provide essential data / fundamental information to predict the final properties of plastic components [9].

Most of the investigations on crystallization are obtained from thermal analysis. The usual conditions of these thermal instruments are very far from the extreme condition in industrial processing. Therefore, it is very difficult to describe the real crystallization process during production using conventional approaches. Recently, new high performance tools appeared which can help to gain breakthrough knowledge in the field of polymer crystallization in a much wider temperature/supercooling range than conventional approaches. To the best of my knowledge, data about the crystallization behaviour of PP nanocomposites are only available in a narrow temperature and cooling ranges. Therefore, the aim of this work is to expand the studies of the crystallization behaviour of PP nanocomposites on industrially relevant conditions.

## 2. State of the Art

### 2.1 Polymer Nanocomposites

In the last few decades, polymer nanocomposites have been attracting increased attention as high performance materials. Nanocomposites can be defined as a multiphase solid material where one of the phases has at least one dimension in the range 1-100 nanometers (nm) [10]. A polymer nanocomposite consists of a polymer with nanofillers dispersed in the polymer matrix. There are three categories of nanofillers depending on how many dimensions are in the nanometric range, including:

- One-dimensional nanolayers, e.g., clays (layered silicates), layered double hydroxides (LDHs)
- Two-dimensional nanotubes, mainly carbon nanotubes, (CNTs), cellulose whiskers
- Three-dimensional particulates such as silica dioxide ( $\text{SiO}_2$ ), calcium carbonate ( $\text{CaCO}_3$ ), metal oxides (e.g. titanium dioxide ( $\text{TiO}_2$ ), iron oxide ( $\text{Fe}_2\text{O}_3$ ), aluminium oxide ( $\text{Al}_2\text{O}_3$ ))

Compared with conventional composites based on micron-sized fillers, polymer nanocomposites based on nanoscale fillers have attracted great attention because of their superior property improvements [1]. This is because the area of the interface between the matrix and fillers is usually an order of magnitude greater than that of a conventional composite. Therefore, with an increase in the surface area to volume ratio with decreasing particle size, even at low concentrations major effects on the macro-scale properties of the composites can be obtained [11].

Compared to the conventional micro-composites, the nanoscopic dimensions and inherent extreme aspect ratios of the nanofillers result in the following interrelated characteristics, which distinguish the obtained nanocomposites [12]:

- Low-percolation threshold
- Particle-particle correlation (orientation and position) arising at low-volume fraction
- Large number density of particles per particle volume
- Extensive interfacial area per volume of particles
- Short distances between particles
- Comparable size scales among the rigid nanoparticles inclusion, distance between particles, and the relaxation volume of polymer chains

Usually, the first two characteristics are hard to observe for spherical nanoparticles because of the small/low-aspect ratio.

## 2.2 Polypropylene Nanocomposites

### 2.2.1 Polypropylene

In the early 1950s, G. Natta succeeded in preparing polypropylene (PP) using the Ziegler catalyst [13]. The stereoregular nature of PP is determined by the position of the methyl side-group ( $-\text{CH}_2\text{CH}(\text{CH}_3)-$ ) along the polymer backbone. There are three typical stereo-configurations that can be distinguished in PP, i.e.:

- Isotactic, in which the methyl group of the  $-\text{CH}_2\text{CH}(\text{CH}_3)-$  mer unit are along the same side as the main chain
- Syndiotactic, in which the methyl units are on opposite sides
- Atactic, in which adjacent methyl units are randomly arranged on both sides of the main chain

As a consequence of the stereo-regularity in a polymer in isotactic polypropylene (iPP) and syndiotactic polypropylene (sPP), the chain can adopt a stable, specific overall conformation. This allows crystallization of the chain. In contrast, atactic polypropylene (aPP) is not crystalline as a periodically repeating unit cell cannot be formally defined [14]. There are four different crystal modifications of PP primarily depending on the crystallization conditions, namely a monoclinic  $\alpha$ -, a trigonal  $\beta$ -, an orthorhombic  $\gamma$ - and a mesomorphic structure [15]. The monoclinic  $\alpha$ -PP is the stable and predominant phase, while the other three crystalline phases can be prepared only under specific conditions. The  $\beta$ -phase is thermodynamically metastable. The crystallization of  $\beta$ -phase can occur in a temperature gradient [16-17], or in the presence of shearing forces [18-19], or when applying selective nucleating agents [20-22]. The  $\gamma$ -phase can be observed in low molecular weight PP and/or under high pressure [23]. A mesophase occurs in quenching and is thermally stable up to 60°C. At higher temperature it is transformed into the  $\alpha$ -phase [18]. These phases have an impact on the crystallization kinetics and the final microstructure. Nowadays, PP is the most widely used and fastest growing class of thermoplastic polymers found in various industries. It exhibits a good balance between physical and mechanical properties as well as an ease of processability at relatively low cost. However, the use of PP is still limited by its comparatively low modulus and stiffness compared to engineering plastics [4].

### 2.2.2 Particulate-Filled Polypropylene

The incorporation of nanofiller is the most widely used technique to enhance the performance of PP. Normally, nanofillers affect the final properties of products in two ways, by,

- Acting as reinforcement
- Affecting the crystallization polymer matrix and composite morphology

The former usually depends on the filler characteristics, such as, shape, primary particle size, aggregate size and the modulus of the fillers [2, 3]. The latter relies on the primary size of the particles, surface modification, shape and concentration of the fillers [3]. Many nanoparticles are used in PP matrix for specific purpose such as  $\text{CaCO}_3$  [2, 24-25],  $\text{SiO}_2$  [3, 7, 26-28],  $\text{TiO}_2$  [6, 29-30].

As compared to conventional fillers, nanoparticles exhibit an enormous surface area being larger by several orders of magnitude. This surface area acts as an interface for stress transfer, but is also responsible for the strong tendency of the nanoparticles to form agglomerates. To achieve excellent properties of polymer nanocomposites, good dispersion and uniform distribution of nanoparticles in the polymer matrix are often required. The dispersion of nanoparticles in polymer melt depends on both extrinsic (e.g. screw configuration, extrusion temperature, screw speed, etc.) and intrinsic (e.g. compatibility between polymer matrix and nanoparticles, viscosity of polymer melt, surface free energy of particles, etc.) variables [24]. The biggest challenge in the nanoparticle-based composites is the intrinsic strength of their agglomerates, which prevents good filler dispersion in the polymer matrix, a key attribute for any reinforcement. The number of articles on improved dispersion of nanoparticles in polymer matrices is increasing every year. One of the most important approaches in this respect is the surface modification of nanoparticles. For instance, Zuiderduin et al. dealt with the dispersion improvement of  $\text{CaCO}_3$  in PP using steric acid [25]. As a result, the impact properties of the PP matrix were improved. On the other hand, Zhang, et al. demonstrated that the  $\text{CaCO}_3$  nanoparticles, treated with fatty acid, exhibited a poor dispersion in the PP matrix. They overcame this problem by adding a small amount of nonionic modifier, which has a long alkyl chain with one hydroxyl end group, during melt extrusion. The polar hydroxyl end group is adsorbed on the surface of  $\text{CaCO}_3$  and the long alkyl chain is compatible with PP molecular chains. It helps to reduce the particle/particle interaction by lowering the surface free energy of  $\text{CaCO}_3$ , leading to

better dispersion of  $\text{CaCO}_3$  particles. This caused a decrease in the size of  $\text{CaCO}_3$  agglomerates, resulting in an increase in the notch Izod impact strength of the PP matrix [24].

Silica is a fine, white, amorphous powder, which is odorless and tasteless.  $\text{SiO}_2$  nanoparticles exhibit hydrophilicity and a very high surface energy due to their extremely high surface area. Their surface is completely covered by the numerous silanol groups due to their manufacturing process [31]. Because the  $\text{SiO}_2$  nanoparticles are inherently hydrophilic, whereas the PP is hydrophobic, surface modification of  $\text{SiO}_2$  nanoparticles beforehand is necessary in order to be compatible with the PP. However, this method is not always successful. Bikiaris et al. revealed that  $\text{SiO}_2$  nanoparticles treated with dimethyldichlorosilane produced larger aggregates compared to untreated nanoparticles, resulting in a decrease in mechanical properties [27]. The use of a compatibilizer such as maleic anhydride grafted polypropylene is an alternative in order to improve the dispersion quality of  $\text{SiO}_2$  in the PP matrix [28].

Because of their photocatalytic potential, ion-exchange ability, semiconducting properties, and large specific surface area,  $\text{TiO}_2$  nanoparticles have been used in many applications [6, 29]. Depending on the thermal and physical treatment, the  $\text{TiO}_2$  exhibits three different crystal structures: rutile (tetragonal), anatase (tetragonal), and brookite (orthorhombic). The anatase can be used as a photocatalyst, while rutile can be used as a white pigment in industry [32-34]. Due to their high mechanical strength,  $\text{TiO}_2$  nanoparticles can be used as a reinforcement material for PP [6, 30]. However, like other nano-sized fillers (e.g.  $\text{CaCO}_3$ ,  $\text{SiO}_2$ ), because of the poor compatibility of hydrophilic  $\text{TiO}_2$  nanoparticles with a hydrophobic PP matrix,  $\text{TiO}_2$  nanoparticles incorporated into polymer matrix easily form agglomerates. Apart from the chemical treatment of nanoparticles, a mechanical approach has been introduced to achieve a homogeneous distribution of nanoparticles. Knör [35] reported the improvement of the

Charpy impact strength and tensile strength of PA/TiO<sub>2</sub> nanocomposites because of TiO<sub>2</sub>-well dispersed in PA by using two-step melting extrusion.

### **2.2.3 Crystallization Effects of Nanoparticle-Filled Polypropylene**

Besides the reinforcement effect, nanoparticles can act as a nucleating agent for polymer matrix. Variations in the solidification conditions usually cause simultaneous variation in the spherulite size, lamellar thickness, and degree of crystallinity, and the presence of nanofiller is considered to change these morphological properties. The crystallization effects of nano-sized particles have been studied in polymer systems with the addition of several materials. Many researchers found that the presence of nanoparticles facilitated faster crystallization of polymer. For instance, Chan, et al. reported an increase in the crystallization temperature of PP with the incorporation of 44 nm of average particle size CaCO<sub>3</sub> [2]. Zhou et al. found the same phenomenon in the case of PP filled with SiO<sub>2</sub> nanoparticles [7]. The effects of surface modification of nanoparticles on crystallization in PP matrix were studied [7, 28, 36-37]. The investigation of nanocomposites also showed a decrease of the spherulite size of polymer matrix caused by the nucleation effect of nanofillers [36-37]. The reduction of spherulite size is caused by an increase of a number of the heterogeneous nuclei density. Also, some authors revealed the increase in crystallinity [27] and spherulite growth rate [37] due to the presence of nanoparticles. The polymer/nanoparticle adhesion is lowered by the surface modification of nanoparticles, resulting in a reduction of the constraint effect of the nanoparticles on the PP molecular chain. This is because part of the surface modifier also acts as a plasticizer for PP, increasing the free volume of PP. Thus, the activation energy required for the transport of PP molecular segments to the crystallization is decreased, resulting in an increase in

spherulite growth rate [24]. In contrast, the decrease in both crystallinity and growth rate was reported [38-39].

## 2.3 Polymer Crystallization

Crystallization is a phenomenon that takes place when a polymer, having the ability to be ordered (chemical and structural regularity), is cooled below the equilibrium melting point. The overall crystallization process of semi-crystalline polymers from the molten state can take place in two main stages: primary crystallization and secondary crystallization.

The primary crystallization stage consists of two major steps: nucleation and crystal growth. Nucleation, which is the step where the molecules dispersed in a system form nuclei, is classified as a homogeneous (thermal nucleation) or a heterogeneous process (athermal nucleation). From a thermodynamic point of view, the crystallization from the quiescent melt is driven by the change of free enthalpy (Gibbs free energy) of crystallization:

$$\Delta G = G_{crystal} - G_{melt} \quad (1)$$

$$\Delta G = \Delta H - T\Delta S \quad (2)$$

where  $\Delta G$  is the change of free enthalpy (Gibbs free energy) of crystallization,  $G_{crystal}$  and  $G_{melt}$  are the free enthalpies of the crystal and the melt, respectively.  $\Delta H$  and  $\Delta S$  are the enthalpy and entropy of crystallization. Crystallization becomes possible as soon as  $\Delta G$  assume negative values [40]. As can be seen in equation (2), in order for the total Gibbs free energy to be negative, then the  $\Delta H$  needs to be negative or weakly positive and  $\Delta S$  needs to be positive.

The nucleation of polymer melt occurs below melting temperature, ( $T_m$ ). The random tangled molecules in melt align and form small ordered regions, which are called

nuclei [41]. The formation of nuclei depends on the degree of supercooling ( $\Delta T = T_m^\circ - T_c$ ).  $T_m^\circ$  is the equilibrium melting temperature of crystalline polymer, which is the theoretical required temperature to completely melt an ideal crystal, and  $T_c$  is the temperature of crystallization.

Figure 2.1 shows a schematic of the change in the Gibbs free energy of liquid and a crystal with temperature. For thermodynamic consideration, a crystal is in a lower free energy state than the liquid when the temperature is below the melting point of the polymer. The process of nuclei formation is spontaneous below the  $T_m^\circ$ , but this process has an activation energy. At  $T_m^\circ$ , a condition of equilibrium exists between the crystal and liquid as both phases have the same value of Gibbs free energy, thus  $\Delta G = 0$ .

A crystal has a small size with a large specific surface area (measured in  $\text{cm}^2/\text{g}$ ) in the beginning. The free enthalpy of crystallization is represented as:

$$\Delta G = \Delta G_c - \sum A\gamma \quad (3)$$

where  $\Delta G_c$  is the bulk free enthalpy change,  $A$  is a surface area, and  $\gamma$  represents the specific surface free energy. The values of  $\gamma$  are positive for all temperatures of interest to crystallization.

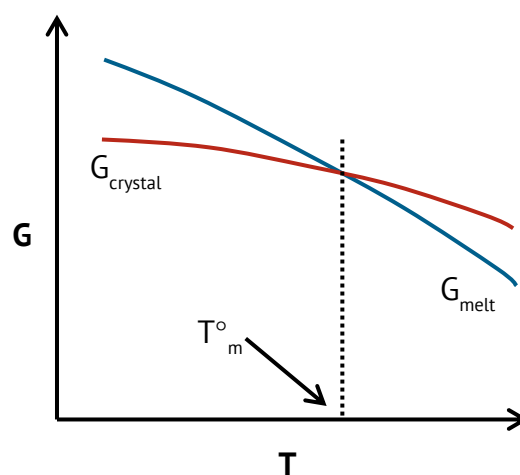


Figure 2.1: Gibbs free energy of crystallization and melt as a function of temperature.

Primary nucleation is the step of the formation of a growing crystal from the amorphous state. Figure 2.2 represents a schematic of the nucleation process. Before a nucleus of critical size is developed, a primary nucleus is formed via a path of positive  $\Delta G$ . The maximum in  $\Delta G$  corresponds to the critical size of the nucleus. Nuclei to the left are called subcritical nuclei or embryos and to the right of this maximum are the supercritical nuclei as long as their  $\Delta G$  is still positive. Nuclei with a negative  $\Delta G$  are called stable nuclei or small crystals. The free enthalpy barrier to crystallization can only be overcome by local random fluctuation of order. The larger the required size of the nucleus, the longer the time needed for the nucleation process [40].

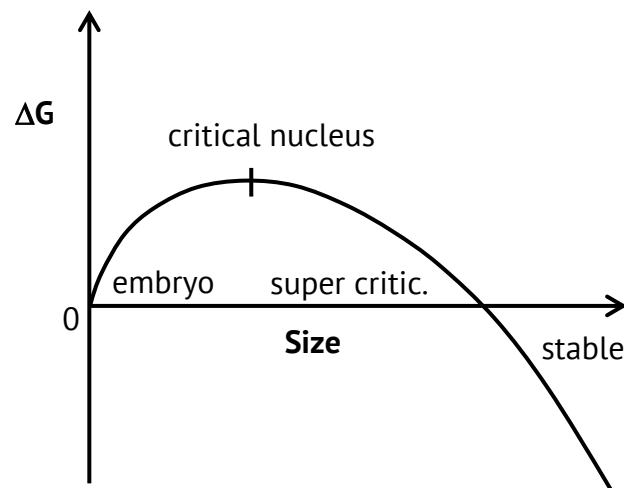


Figure 2.2: Schematic diagram for the free energy of formation of nucleus.

In homogeneous nucleation, nuclei are created by random statistical fluctuations of the local structure of the polymer. In contrast, in heterogeneous nucleation, nuclei are introduced by the presence of foreign particles such as impurities and nucleating agents. A foreign surface reduces frequently the nucleus size (lower free enthalpy barrier) needed for crystal growth. This is due to the creation of the interface between polymer crystal and the substrate may be less hindered than the creation of the corresponding free polymer crystal surface.

Once the nucleation starts, the second process can take place. The second step in the crystallization process is the crystal growth where the nuclei grow. With decreasing temperature, the thermodynamic driving force for crystallization increases. As this occurs, the viscosity of the melt increases and the mobility of the chain decreases (kinetic factor). These opposing influences of lowering the temperature result in a maximum of the rate of nucleation and growth of the nuclei between melting temperature ( $T_m$ ) and glass transition temperature ( $T_g$ ) [42]. As schematically depicted in Figure 2.3, rates of the two processes increase with decreasing temperature below the  $T_m$ , and is generally recognized to decrease again as the  $T_g$  approaches. The maximum of the nucleation rate is expected to appear at a lower temperature than that of the growth rate.

The growth of nuclei can take place in one, two, or three dimensions with the crystals developing in the form of rods, discs or spheres, respectively, depending on crystallization conditions [41]. The lamellar crystals often aggregate into supermolecular structures known as spherulites.

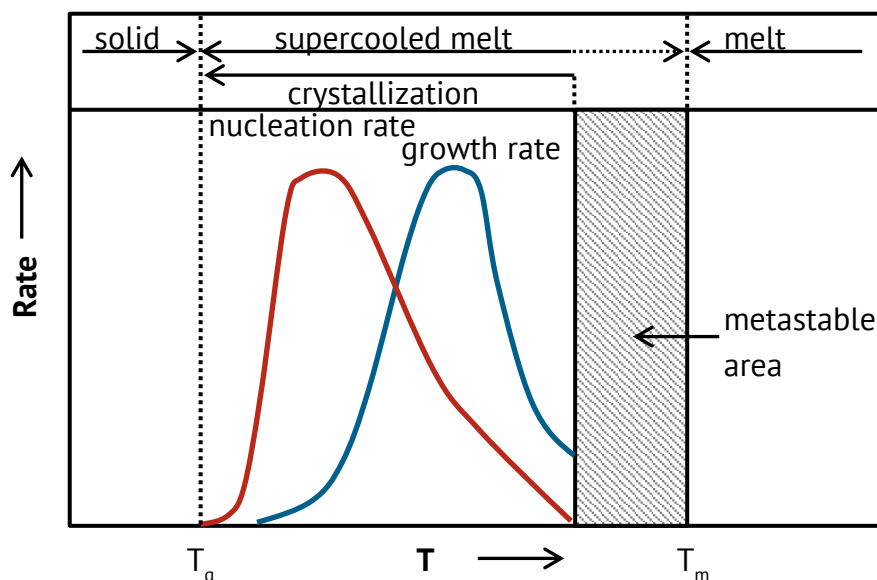


Figure 2.3: Temperature dependence of the nucleation rate and the growth rate on cooling from the melt [42].

For crystallization from a polymer melt, the regions between lamellae remain amorphous. This amorphous phase is composed of molecule loops, entanglements and chain ends and constitutes a weak linkage within the polymer [43]. Figure 2.4 shows examples of schematic representation of spherulitic formation and spherulites of polyethylene obtained from polarized light microscopy. The change of the spherulite radius at a given crystallization temperature, the so-called growth rate ( $G$ ), is usually linear with time. Spherulite growth stops when impingement by neighboring spherulites occurs. Therefore, crystallization is a process that takes place in two distinct steps, which are considered separately [41]. The polymer molecular weight and the degree of supercooling govern the lamellae thickness: longer molecules and higher crystallization temperatures lead to thicker crystallites.

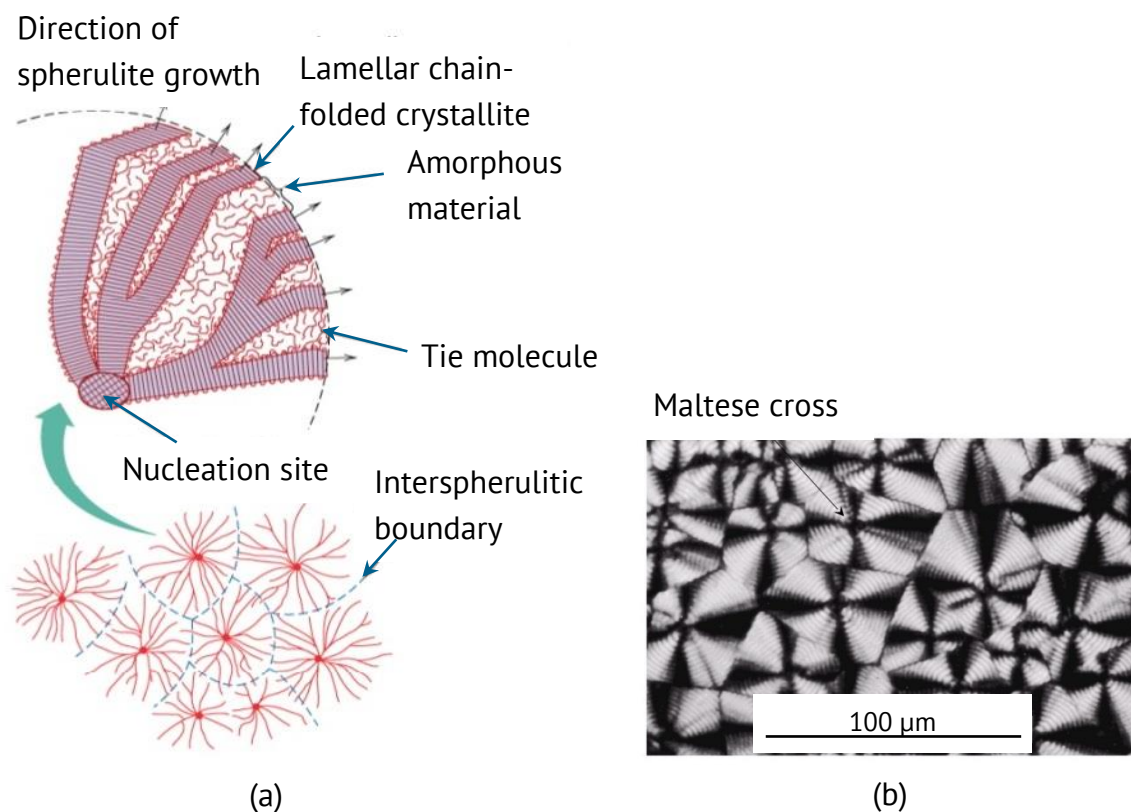


Figure 2.4: Spherulites: (a) schematic representation of spherulitic formation and (b) micrograph of spherulitic structure of polyethylene under polarized light microscope [47].

Secondary crystallization is mainly related to the process of lamellar thickening or further perfection of initially poorly crystallized macromolecules and is called crystal perfection [44-46]. It may be viewed as a slow process of completion of the crystallization process in polymer and has been demonstrated to have immense implications on the time-dependent properties of polymers.

### **2.3.1 Structure Development and Crystallization in Injection Molding**

Injection molding is one of the most important polymer processing operations in the manufacturing of polymeric products. This is because of its high degree of automation, high productivity and good dimensional stability of moldings. There are three main stages, namely filling, packing and cooling, in the injection molding process of thermoplastics. During the molding cycle, high shear and normal stresses, and temperature gradient are developed in the polymer melt. It is well known that the ultimate physical, optical and mechanical properties of semi-crystalline polymers are highly dependent on the morphological structure, which is governed by the respective crystallization during the production. Crystallization of semi-crystalline polymers is influenced by the thermo-mechanical history during the injection molding. Different structures are formed during processing, depending on the conditions and usually the final morphology of a product consists of a combination of these structures. Crystalline structures start to grow from small objects called nuclei, which have a certain degree of order. The number and type of the nuclei formed is dependent on the amount of strain experienced during flow. In a quiescent condition the absence of shear stress in the center of a product results in a spherulitical structure, while in the high shear stress regions at the cavity walls an oriented structure can be present. Knowledge of the mechanism of morphological structure development during injection molding is crucial in order to optimize the final properties of products. It is important to understand the

crystallization kinetics under processing conditions to describe the morphological structure development in the molding. This requires for the simulation of an injection molding process of semi-crystalline polymers [48-49].

### 2.3.2 Quiescent Crystallization

By using thermo-analytical (TA) data, analysis of quiescent crystallization kinetics is usually performed under either isothermal or non-isothermal conditions. In polymer processing operations such as injection molding, for instance, crystallization from the melt occurs under non-isothermal conditions. Therefore, the study of structure development in the melt processing of polymers is investigated under non-isothermal conditions. On the other hand, isothermal studies are used to elucidate the mechanism of crystallization, which is necessary for assisting with process optimization and for understanding process-structure-property relations in polymers.

#### Isothermal Crystallization

Investigation of isothermal crystallization kinetics is usually carried out using data obtained from exothermic crystallization. This is based on the assumption that the evolution of crystallinity is directly proportional to the heat evolved during the progress of crystallization [50]. By integrating the heat evolved during crystallization, the relative degree of crystallinity as a function of crystallization time  $X(t)$  can be defined as follows [51]:

$$X(t) = Q_t/Q_\infty = \int_0^t \left(\frac{dH}{dt}\right) dt / \int_0^\infty \left(\frac{dH}{dt}\right) dt \quad (4)$$

where  $Q_t$  and  $Q_\infty$  are the heat generated at time  $t$  and at an infinite time  $t_\infty$ , respectively.  $dH$  is the heat evolution of crystallization during an infinitesimal time

interval  $dt$ . In order to quantitatively describe the macroscopic development of crystallinity under quiescent isothermal conditions, a number of macrokinetic models have been proposed [52-60].

The classical method proposed by Avrami is used mostly to analyze the time-dependent relative crystallinity  $X(t)$ . According to Avrami,  $X(t)$  is related to the crystallization time ( $t$ ), by the expression [52-54]:

$$X(t) = 1 - \exp(-k_a t^{n_a}) \quad (5)$$

where  $n_a$  is the Avrami exponent, which is a constant depending on the mechanism of nucleation and the form of crystal growth, while  $k_a$  is the isothermal rate constant of crystallization which is related to the nucleation and growth rates.

This is based on a simplified assumption that nucleation is unique and the crystal growth rate is constant (at a given temperature). Another assumption is that there is no interaction with neighboring crystals (free growing in all directions) and there is no volume change during crystallization [61]. Ideally, the value of the Avrami exponent, which provides information on the nucleation mechanism and the crystal growth geometry, should be an integer, ranging from 1 to 4 [62]. However, fractional values of  $n_a$  are usually observed to provide the best fit with experimental findings. This is due to the fact that crystallization is far too complicated for such a simple assumption [63]. With a mix of thermal and athermal nucleation mechanisms, fractional values for  $n_a$  are normally observed [4, 40]. Therefore, many studies [55-60] have attempted to develop this model by refining the above assumption.

Because the Avrami model is only appropriate for the primary stage of crystallization, Tobin [55-57] proposed a way to improve the Avrami model so that it could be applied to the later stages of crystallization, which attempts to take the concept of impingement of crystals into consideration, is specified as;

$$X(t) = \frac{k_t t^{n_t}}{1 + k_t t^{n_t}} \quad (6)$$

where  $k_t$  is the Tobin crystallization rate constant and  $n_t$  is the Tobin exponent. Based on equation (3),  $n_t$ , which can be either an integer or a noninteger, is mainly governed by different types of nucleation and growth mechanisms [57].

Malkin [58] developed an equation which is able to take into account the suggestion that the overall rate of crystallization is a result of the appearance of primary nuclei and changes to the crystal growth rate during crystallization. The kinetic expression is as follows:

$$X(t) = 1 - \frac{C_0 + 1}{C_0 + \exp(C_1 t)} \quad (7)$$

where  $C_0$  is the Malkin exponent, which is directly related to the ratio of the linear growth rate,  $G$ , to the nucleation rate,  $N$ , i.e.  $C_0 \propto G/N$ , while  $C_1$  is the Malkin crystallization rate coefficient, which is directly connected to the overall crystallization rate,  $C_1 = aN + bG$ , where  $a$  and  $b$  are specific constants. The unit of  $C_1$  is given in (time)<sup>-1</sup>.

While the Avrami equation and its modifications [52-60] are used to describe the bulk crystallization kinetics of polymers, the Lauritzen-Hoffmann theory [64] suggests that crystallization is controlled by nucleation and transport of the macromolecules in the melt. This theory relates the radial growth rate ( $G$ ) to the rate of secondary nucleation and the rate of lateral growth. Lauritzen-Hoffmann theory assumes that a free energy barrier associated with nucleation has an energetic origin and it provides the general expression for the  $G$  of a linear polymer crystal with folded chains:

$$G = G_0 \exp\left[\frac{-U^*}{R(T_c - T_\infty)}\right] \exp\left[\frac{-K_g}{T_c(\Delta T)f}\right] \quad (8)$$

where  $G_0$  is the pre-exponential factor,  $U^*$  is the transport activation energy, (6280 J/mol for PP)  $\Delta T = T_m^\circ - T_i$  is the supercooling range ( $T_m^\circ$  is the equilibrium melting

temperature of an ideal crystal that is perfect and has an infinite crystal size),  $R$  is the gas constant (8.314 J/(mol K)).  $f$  is the correction factor related to temperature, usually described as  $f = 2T_i / (T_m^\circ + T_i)$  to account for the variation in the heat of fusion per unit volume of crystal,  $\Delta h_f$  ( $1.93 \times 10^8$  J/m<sup>3</sup> for PP).  $T_\infty$  is the theoretical temperature at which all motion associated with viscous flow ceases, defined as  $T_\infty = T_g - 30$  K.  $K_g$  is the nucleation constant and can be expressed as

$$K_g = \frac{j b_0 \sigma \sigma_e T_m^\circ}{k_B (\Delta h_f)} \quad (9)$$

where  $j = 4$  for regime I and III growth and  $j = 2$  for regime II.  $b_0$  is the layer thickness ( $6.26 \times 10^{-10}$  m for PP),  $\sigma$  is the layer surface free energy ( $1.15 \times 10^{-2}$  J/m<sup>2</sup> for PP),  $\sigma_e$  is the fold surface free energy,  $k_B$  is Boltzmann's constant ( $1.38 \times 10^{-23}$  J/K) [65].

Using a theoretical approach, it can be shown that the linear growth rate  $G$  can be considered proportional to the reciprocal crystallization half-time,  $1/t_{1/2}$ . The number of nuclei is assumed to be independent of temperature and all sites become active simultaneously [66]. The Lauritzen-Hoffmann equation can be adapted to describe the temperature dependence of the overall crystallization rate:

$$\left(\frac{1}{t_{1/2}}\right) = \left(\frac{1}{t_{1/2}}\right)_0 \exp\left[\frac{-U^*}{R(T_i - T_\infty)}\right] \exp\left[\frac{-K_g}{T_i(\Delta T)f}\right] \quad (10)$$

Ideally, the growth of spherulite occurs in a 3D environment. It is worth noting that the growth rate values measured by optical microscopy are obtained under a confined 2D environment. This is because the spherulites grow between microscope glass and cover slides. There is doubt whether a limited number of 2D measurements can really represent the true 3D spherulite growth in large numbers. In contrast, DSC analysis allows 3D spherulite growth and the experimental data provide a more macro-scale representation of the real situation [67]. As is well known, the rate of crystallization of a polymer strongly depends on the degree of supercooling,  $\Delta T$ .

One of the well-known methods for the determination of  $T_m^\circ$  of a polymer is the Hoffman-Weeks plot. Here, this method is used to determine  $T_m^\circ$  by the plot of  $T_m$  versus  $T_i$  according to the following equation [68-69],

$$T_m^\circ - T_m = \theta(T_m^\circ - T_i) \quad (11)$$

where  $\theta = 1/\gamma$  is the stability parameter which depends on the crystal thickness. It is assumed that  $\gamma = l/l^*$ , where  $l$  and  $l^*$  are the thicknesses of a mature crystallite and that of the critical crystalline nucleus at  $T_i$ , respectively. In equation (9),  $\theta$  may assume all values between 0 and 1,  $\theta = 0$  implies  $T_m = T_m^\circ$ , whereas,  $\theta = 1$  implies  $T_m = T_i$ . Thus, the crystals are most stable for  $\theta = 0$  and are intrinsically unstable for  $\theta = 1$ .  $T_m^\circ$  is determined from the intersection of the plot  $T_m$  versus  $T_i$  and a line representing the thermodynamic condition where  $T_m = T_c$ ; that is, the crystal is perfect and in thermodynamic equilibrium with the melt [69-70].

### **Non-isothermal Quiescent Crystallization**

Basically, in real industrial processing such as injection molding the morphological development occurs during non-isothermal crystallization from the molten state of absorbable semi-crystalline polymers. The morphological development under non-isothermal crystallization is strongly dependent on the cooling rate. For the high cooling rates, the lower temperatures favor nuclei formation resulting in a higher number of spherulites and therefore, small sizes. Nucleation can even be bypassed if the polymer melt is quickly quenched to a temperature below the glass transition temperature and can result in an entirely amorphous phase. In order to optimize the condition in an industrial process, the qualitative evaluation of non-isothermal crystallization is necessary [71]. In order to describe the temperature dependence of

the overall crystallization rate, the Lauritzen-Hoffman equation was applied to experimental data obtained from the non-isothermal condition [72].

### Crystallization Activation Energy

The crystallization of polymer is controlled by two main factors: one is the static factor, which is related to the free energy barrier for nucleation and the other is the dynamic factor, which is related to the activation energy for the transport of crystalline units across the phase [73]. The Kissinger method [74] is one of the most extensively used methods to obtain the kinetic parameters in several fields, such as glass transition, thermal decomposition, curing process and crystallization [75]. Considering that the heating rate greatly influences the peak temperature of the phase transition process, Kissinger proposed an expression derived from the variation of peak temperature versus heating rate. Based on the Kissinger method, the crystallization activation energy of polymer can be estimated by calculating the variation of crystallization peak temperature as a function of the cooling rate:

$$\frac{d\left[\ln\left(\frac{\phi}{T_p^2}\right)\right]}{d\left(\frac{1}{T_p}\right)} = -\frac{\Delta E}{R} \quad (12)$$

where  $T_p$ ,  $R$  and  $\phi$  are the peak of crystallization temperature, the universal gas constant and cooling rate, respectively. The plot of  $\ln\frac{\phi}{T_p^2}$  versus  $\frac{1}{T_p}$  should be a straight line with a slope of  $-\frac{\Delta E}{R}$ .

### Crystallization of Polymer by Fast Scanning DSC

The most investigations of crystallization were obtained from conventional DSC, where the fastest applied cooling rate could not exceed 1 K/s [76]. Experimental data about

crystallization are only available in a narrow cooling and temperature range. This often leads to crystallization at low supercooling of the melt, which is related to the crystallization of sample in the center of the wall cavity. At this location, the material cools down very slow. The cooling rate increases from the center to the wall cavity. At other locations, crystallization investigation at cooling conditions relevant in polymer processing, which is beyond the capability of standard DSC, is not possible. Consequently, to reach higher cooling rates high performance DSCs are required. Notable developments include the ultra-fast scanning calorimeters [77-78] and flash DSC 1 [79]. The development of such high performance DSCs has helped the breakthrough knowledge in the field of polymer crystallization in a much wider temperature/supercooling range than on application of DSC. This technique has given new insights on crystallization, melting behaviors, glass transition and structural reorganization under sufficiently fast cooling of various polymers such as PA 6 [80], PA 11 [81-82], PBT [83-84], PET [84], PLA [85-86], PTFE [87], PB [86, 88] and iPP [83, 86, 89-92].

### **2.3.3 Morphology of Injection Molded Samples**

#### **Unfilled Polypropylene**

In most polymer processing operations such as injection molding the morphology and crystallization of semi-crystalline polymers are affected mainly by the thermo-mechanical history during processing [93]. Figure 2.5 schematically gives the melt flow behaviors during the filling stage of injection molding.

In injection molding, shear and temperature gradients during the crystallization of semi-crystalline polymers have to be taken into account. During processing, flow is considered to be a huge factor to improve the crystallization rate of the polymer by

initiating the formation of nuclei [94]. As a consequence, this allows the morphology of the polymers and thus the final properties of products to be influenced [95].

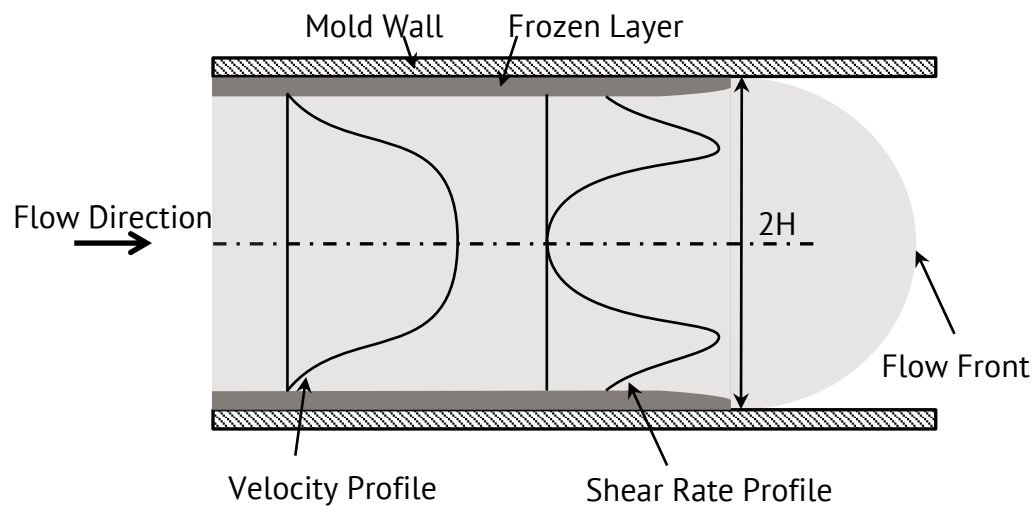


Figure 2.5: A schematic of flow profile during the injection process.

Crystallization from the melt can occur under either quiescent or shear induced-conditions. During the filling of molten polymer into a cavity, the polymer is subjected to high shear stress at the cavity wall, which causes a special orientation of the molecular chains. In addition, the cavity wall, which is in direct contact with the cooled mold, leads to a high cooling rate. These conditions, high shear stress and high cooling rate, result in a skin layer (or shear-induced crystallization layer), which forms at the surface of the part. Conversely, in the core of the component, due to a relatively low cooling rate and low shear stress, the effect of shear on crystallization can be neglected. Therefore, the crystallization of the polymer is considered to be three-dimensional under the quiescent condition to form a spherulitic microstructure [48, 93, 96]. Figure 2.6 presents typical skin-core morphology of iPP.

The first demonstration of a skin-core morphology of injection molded PP was displayed by Kantz and co-worker in 1972 [48]. The following year, Fitchmun et al. [98] also extensively investigated the detailed morphology of injection molded PP using

optical microscopy (OM) and scanning electron microscopy (SEM) analysis. Typically, a multilayer structure of the skin-core of injection molded samples of PP is observed throughout their thickness and at least three distinct layers can be identified [48, 99]. The skin layer is usually considered to be a highly oriented molecular chain and a very thin layer. The core layer is a region, which allows complete relaxation of the chain molecules and the growth of spherulites. The area is located between the skin and core layers, typically called the intermediate layer, shear or transition zone. In this region, the number of layers can vary depending on the author's definition [48, 98]. In addition, it is possible to separate a multilayer structure into either four [93, 99-100], five [101-102] or six layers [95].



Figure 2.6: Skin-Core morphology of polypropylene [97].

The final morphology was characterized in terms of distribution along the sample thickness of lamellar thickness, long periods, molecular orientation, and degree of crystallinity and dimension of spherulites. Although the skin-core morphology is strongly influenced by the shear distribution and temperature gradient during the injection of the melt, the morphological parameters through the thickness sample, such

as lamellar thickness, and long periods are mainly influenced by the cooling conditions [103]. The lamellae were thinner in the skin layer than in the core layer [104]. The distribution of crystallinity was controversial. Zhu and co-workers reported that a higher amount of shear force at the skin gave a higher degree of crystallinity compared to the core layer [104-105]. In contrast, Meister and Drummer revealed that the degree of crystallinity in the core was higher than in the skin layer [96]. However, Pantani and co-workers revealed that the degree of crystallinity along the thickness of the sample was almost constant [106]. Micrographs obtained from both optical and electron microscopy confirmed the distribution of spherulites size along the thickness. The spherulites decreased from the core to the skin layer [49, 106-107].

### **Particulate-filled Polypropylene**

Although the shear-induced crystallization of polymer has already been well described, only a few researchers have studied the shear-induced crystallization of polymer nanocomposites so far. Among these, Radhakrishnan [108] found that besides the cooling rate, the type and concentration of filler and its thermal conductivity had an influence on the thickness of the skin-core morphology. Higher thermal conductivity led to larger heat transfer and a faster cooling rate. This resulted in the skin layer being thicker than the original polymer. A similar phenomenon was reported by Moretti et al. [109]. Conversely, Somnuk et al. [110] found a decrease in the thickness of the skin layer of PP/vetiver grass composites. They pointed out that this was due to the large particles of vetiver fiber obstructing the normal flow of the polymer and hindering the chain mobility.

## 2.4 Polymer Deformation in Term of Spherulites

The understanding of the macroscopic mechanical behavior of semi-crystalline polymers requires the knowledge of the deformation mechanisms that occurs at different scales from the microscopic to the nanoscopic [111]. It is clear that the existence of a microstructure on a variety of dimensional levels affects the micromechanical behavior, which appears to be extremely complex [112]. It is by now well established that the deformation modes operative in semi-crystalline polymer involve both the amorphous and the crystalline components. The discussion on the deformation proceeds from the single crystals scale [113] to the spherulitic [112, 114] and then to the macroscopic scale. At the spherulitic scale, the deformation of a spherulitic structure in a semi-crystalline polymer has been well reviewed by Bowden and Young [115] and Lin and Argon [116]. Spherulites primarily are composed of radially stacked crystalline lamellae separated from each other by interlamellar amorphous regions and held together by tie molecules. The aggregation of space-filling spherulites forms bulk polymers. Therefore, how spherulites behave under applied stresses is one of the most important considerations in understanding the plastic deformation of semi-crystalline polymers, and in linking the macroscopic properties to microscopic structure and deformation modes [116].

The experimental investigation of the deformation has been performed using direct microscopic observations under optical and electron microscopy and X-ray diffraction on either cast films or microtomed sections from bulk samples [117-118]. When an external force is applied to a polymer, it is deformed. The internal distribution of forces depends on the location within the spherulite; therefore, the response of the spherulites to deformation is non-uniform and highly recoverable. The deformation of spherulites can occur in the crystalline region, in the amorphous region and between spherulites. The initial deformation occurs via deformation of the amorphous

component. At low loading condition, the material shows elastic behavior, therefore an almost complete reversibility of deformation is observed from these mechanisms. This is due to either the rubber nature of the amorphous tie molecules linking adjacent lamellae or the residual stresses of the surrounding undeformed regions. [112, 116].

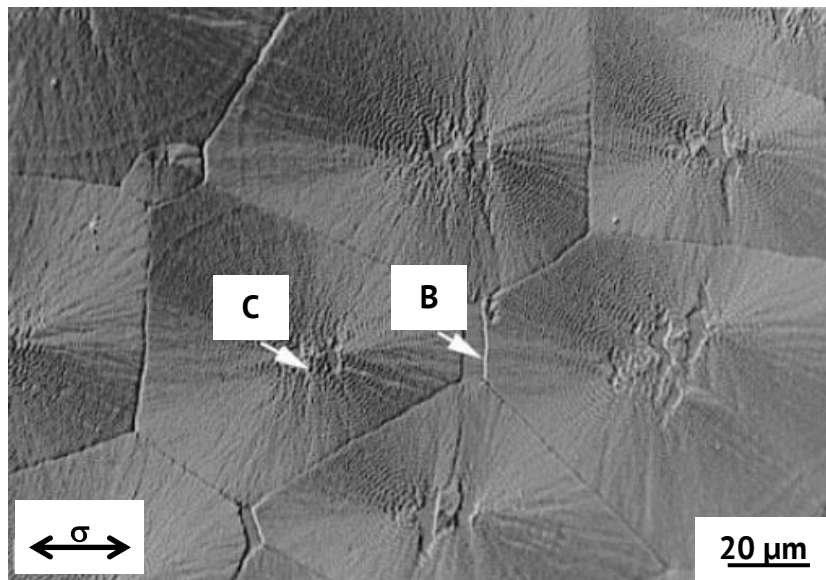


Figure 2.7: Optical micrograph of LLDPE sample deformed to 20% strain. B and C represent the spherulite boundaries and the spherulite centers where crack initiated [112].

The difference in deformation processes is like to be due to a variation of stress within the spherulite. The plastic deformation in spherulites initiates in regions with high stress concentration. These regions may be either the spherulite center or the spherulite boundary [114, 119]. Due to the branching of the lamellae, there are fewer lamellae available to carry the force approaching the spherulite center. This results in a concentration in stress at the nucleus. Although, there is no branching effect at the spherulite boundaries, they may be considered to act as tie points for the lamellae of neighboring crystals. This again results in a concentration of stress but not as severe as that at the nucleus [119].

Normally, the deformation takes place first in the center of the spherulite perpendicular to the tensile direction. In some cases, the deformation sets in first at the boundaries between the spherulites, which were perpendicular to the tensile direction as shown in Figure 2.7. Further stretching results in the deformation proceeding with the spherulite becoming elongated parallel to the tensile direction [115, 120]. However, the whole of the spherulite is found to deform and eventually a fibre structure is produced at higher elongation. Consequently, the spherulites themselves become more separated at higher elongation.

It has been reported the effect of spherulite size on the mechanical properties of semi-crystalline polymer. Starkweather and Brooks revealed the yield point of polyethylene increased by decreasing the spherulite size at a constant degree of crystallinity [121]. Way et al. showed that the yield stress of PP goes through a maximum at a critical spherulite size [122]. However, in the absence of foreign substance an increase in the degree of crystallinity is usually accompanied by an increased spherulite size. The tensile yield increased linearly with increasing crystallinity as well as with increasing spherulite size. In semi-crystalline polymer composite, Maiti and Mahapatro [123] claimed that the increased yield stress was correlated with an increasing crystallinity. They showed that a crystallinity increase associated with additions of foreign substance.

However, the discussion above is based on the deformation of thin film. This lacks the constraints of more general deformation in bulk sample. In general, there are two main processes of plastic deformation of solid polymer, crazing and shear yielding. Crazing is cavity formation process which occurs under an applied tensile stress and leads to brittle failure at small strains. On the other hand, shear yielding is distortional deformation occurring at constant volume and accompanied by necking [124]. Since this work focus on the deformation of thin section with a thickness of 30  $\mu\text{m}$  (plane

stress state), the deformation in bulk sample with a thickness of 4 mm (plane strain state) will not go into the details.

### **3. Objective of the Study**

There is a lack of studies on the crystallization behavior of PP-based nanocomposites at high supercooling (low temperature/high cooling rate) as are used in the real processing. Thus, this work focuses on investigations of crystallization behavior of PP-based nanocomposites at industrially relevant supercooling. Further, the resulting morphologies developed during injection molding are related to selective mechanical properties.

The main objectives of this work are:

- To monitor quiescent crystallization behavior of PP-based nanocomposites under industrial processing conditions and describe the influence of nanoparticle on these crystallization behaviors.
- To analyze the influence of processing history and nanoparticles on the microstructure of injection molded-parts of PP-based nanocomposites. In this work the morphological distribution throughout the thickness of the samples and the reasons for these distributions are described and investigated.
- To determine the mechanical properties of the thin section throughout the thickness of the samples and evaluate the influence of nanoparticles on the mechanical properties.
- To characterize the spherulitic deformation during mechanical testing and clarify the effect of nanoparticles on the deformation.

## 4. Experimental Procedures

### 4.1 Materials

#### 4.1.1 Polypropylene

Commercial polypropylene (PP HD120MO, Borealis GmbH, Burghausen, Germany) was used as a matrix material in the present work. The specification of the PP referred to the information of the supplier is listed in Table 4.1.

Table 4.1: Specifications of the PP matrix used in this work [125]

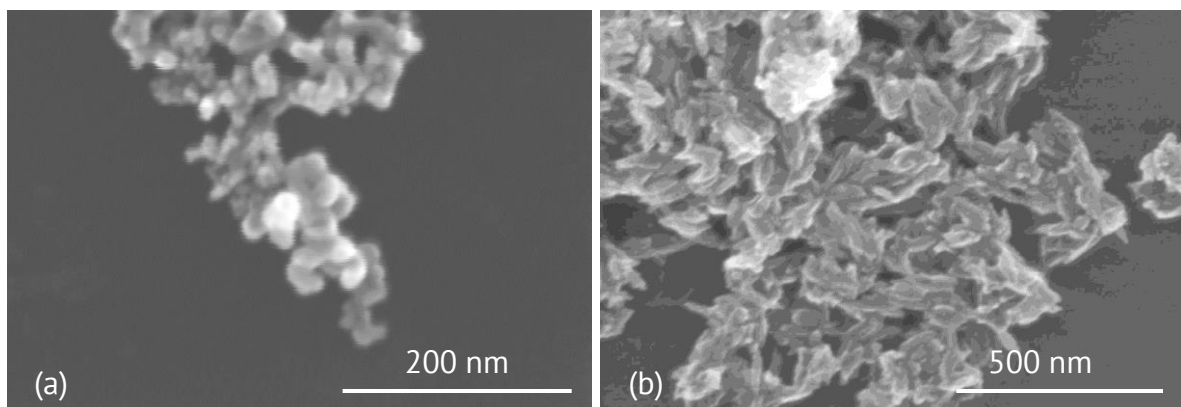
Properties		
Density	g/cm <sup>3</sup>	0.908
Young's modulus	MPa	1500
Tensile strength	MPa	33.5
Charpy notched impact strength (23°C)	kJ/m <sup>2</sup>	4
Melt flow rate	cm <sup>3</sup> /10 min	8.8
Melting point	°C	165
Thermal conductivity (solid)	W/m·K	0.22
Thermal conductivity (melt)	W/m·K	0.13
Heat capacity	J/g·K	2.2

#### 4.1.2 Nanofillers

Two types of nanofillers, namely silicon dioxide (SiO<sub>2</sub>) nanoparticles (Aerosil R8200, Evonik Degussa GmbH, Hanau-Wolfgang, Germany) and titanium dioxide (TiO<sub>2</sub>) nanoparticles (Hombitec RM130 F, Huntsman GmbH, Duisburg, Germany), were used as inorganic nanofillers. Their specifications referred to the information of manufacturers and literatures are listed in Table 4.2. Figure 4.1 presents the high resolution SEM images of the nanoparticles.

Table 4.2: Specifications and properties of the nanofillers [125-127]

Specifications and Properties		Fillers	
		SiO <sub>2</sub>	TiO <sub>2</sub>
Diameter of primary particles	nm	12, spherical	15, acicular
Special surface	m <sup>2</sup> /g	160±25	50 - 100
Surface treatment	-	Hexamethyldisilazane	Al, stearic acid
Density	g/cm <sup>3</sup>	2	4
Young's modulus	GPa	73	244
Heat capacity at 20°C	J/g·K	0.7	18.2
	W/m·		
Thermal conductivity (solid)	K	1.4	6.5
Refractive index, n	-	1.6	2.5
Surface tension	mJ/m <sup>2</sup>	33	700

Figure 4.1: SEM images of nanoparticles: (a) SiO<sub>2</sub> powder, (b) TiO<sub>2</sub> powder.

## 4.2 Preparation of Nanocomposites

### 4.2.1 Extrusion

In order to obtain homogeneous nanoparticle dispersion, a two-step extrusion procedure was adopted for the compounding of nanocomposites. The procedure was described by Knör et al [35] in detail. A masterbatch was first extruded by a co-rotating

twin-screw extruder (Theysohn, Theysohn Extrusionstechnik GmbH, Salzgitter, Germany) at a screw speed of 160 rpm. The diameter of the screw was 30 mm and the L/D (length/diameter) ratio was 40. The temperatures were set from 190°C near the hopper to 210°C at the die. During the melt extrusion, the ventilation was kept on to remove trapped air in the compounds. In the second step, the extruded compounds were then diluted to designed nanocomposites as shown in Table 4.3.

Table 4.3: Sample designation and composition of PP-based nanocomposites

Designation	Composition, vol.%		
	PP	SiO <sub>2</sub>	TiO <sub>2</sub>
PP-V0	100	-	-
PP-S-V1	99	1	-
PP-S-V4	96	4	-
PP-T-V1	99	-	1
PP-T-V4	96	-	4

### 4.2.2 Injection Molding

After extrusion, the neat PP and its nanocomposites were injection molded (Arburg Allround 420C, ARBURG GmbH + Co KG, Loßburg, Germany) to 50x50x4 mm<sup>3</sup> plates. The temperatures were set from 170°C near the hopper to 190°C at the nozzle. A mold temperature of 40°C and an injection rate of 10 ccm/s were used.

### 4.3 Preparation of Testing Samples

To prepare the samples for the investigation of morphology and thermal analyses, the center part of injection molded plate was cut into rectangular cuboids (see Figure 4.2). The rough surface was then removed by a rotation microtome (Hyrax M 25, Carl Zeiss MicroImaging GmbH, Jena, Germany) equipped with a steel blade to yield a smooth surface.

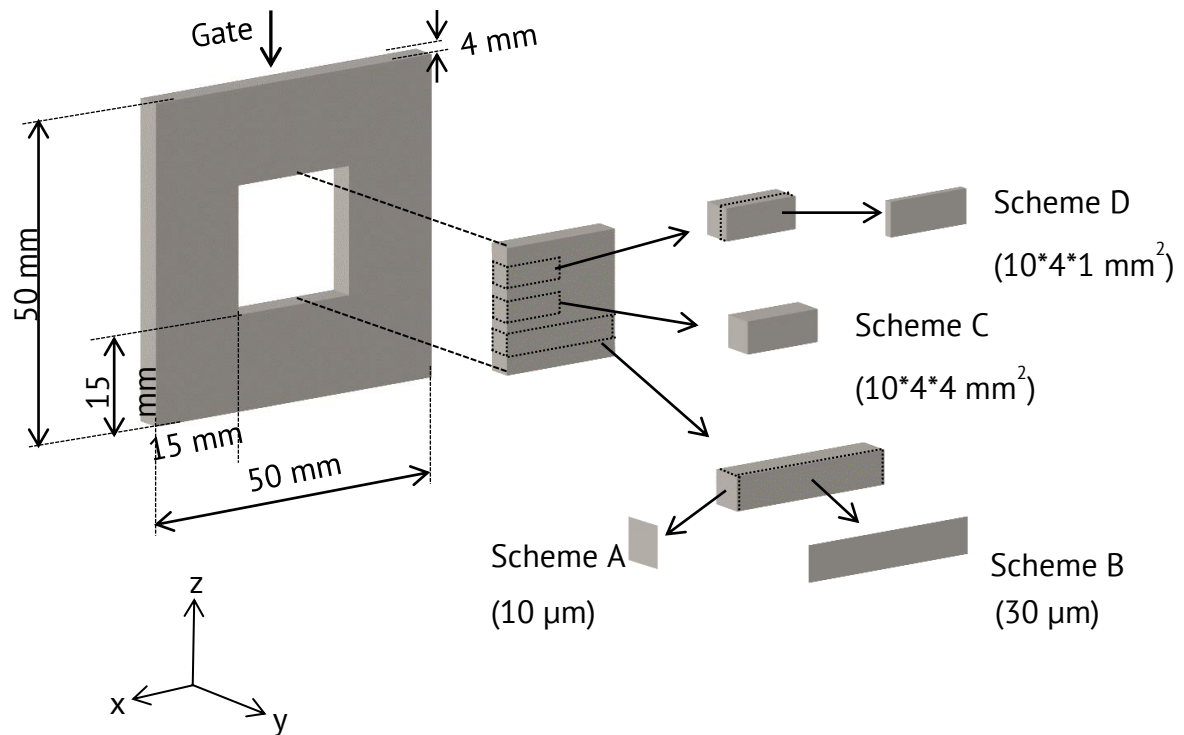


Figure 4.2: Cutting of sample procedures.

- Scheme A: for optical investigation
- Scheme B: for calorimetric and X-ray investigations, and micro-tensile testing
- Scheme C: for etching preparation
- Scheme D: for ion polishing

### 4.3.1 Thin Sections

Two cutting procedures were used to section the samples. These cutting procedures are shown in schematic A and B of Figure 4.2. To examine the skin-core morphology, thin sections of 10  $\mu\text{m}$  were cut from the rectangular cuboids perpendicular to the flow direction as illustrated in schematic A of Figure 4.2.

For the study of the degree of crystallinity and its distribution and the mechanical properties, thin sections of 30  $\mu\text{m}$  were cut from the center part of the injection-molded plate along the thickness direction (y), Figure 4.2 (Scheme B).

### 4.3.2 Etched Samples

Rectangular samples prepared in accordance to section 4.3 (schematic C of Figure 4.2) were subjected to chemical etching based on a procedural description of Basset and Olley [128] and Shahin et al [129]. In this experiment, an etchant formulation with 0.7% weight/volume of potassium permanganate crystals of a mixture of 2:1 by volume 98% sulphuric acid and 85% phosphoric acid was used. The permanganic etchant solution was prepared by adding 1.47 gram of potassium permanganate crystal to a mixture of sulphuric acid and phosphoric acid which had previously been cooled down to room temperature. The mixture was then stirred with magnetic stirrer until the permanganate crystals were thoroughly dissolved (about 30 minutes) to give a concentrated deep green solution. The samples were then introduced to the etchant and stirred rigorously for 18 hours at room temperature, followed by 6 hours at 60°C.

Near the end of etching period, washing solution was prepared by mixing 2:7 by volume of concentrated sulphuric acid and distilled water, the solution was allowed to cool to room temperature. To 10 parts volume of this solution, 1 part volume of 30% hydrogen peroxide was added and stirred. The resulting solution was then cooled down with an ice bath. At the end of etching period, the etchant and the samples were poured into the cold washing solution and were shaken for 3 minutes to yield clear liquid. The samples were further washed with distilled water and finally with methanol using ultrasonic bath.

### 4.3.3 Ion-polished Samples

A sample of 1 mm thickness (see Figure 4.2, scheme D) was cross-section polished using ion milling system (E-3500, Hitachi, Krefeld, Germany) for overnight. The depth of polished area is about 300  $\mu\text{m}$ . A silver glue was placed on all sides of the samples to prevent the charging of the electron beam during SEM analysis.

### 4.3.4 Fractured Surface

Rectangular samples prepared in accordance to section 4.3 were used to prepare cryofractured samples in order to reveal the dispersion and orientation of nanoparticles in the matrix. The samples were prepared by dipping each sample in liquid nitrogen for 30 minutes until it was frozen to retain nanoparticles dispersion behavior in the matrix and to minimize non-structure artifacts due to plastic deformation. The samples were then broken with a pair of pliers. Fractured samples were prepared for neat as well as for all concentration of filled PP.

## 4.4 Simulation of Injection Molding

A simple simulation was performed by using the commercial software package, Moldflow, in order to predict the cooling rate along the sample thickness in the injection mold process. In present work, Moldflow is used for simulating the filling of the injection molding. All physical properties of the polymer used in the simulation were taken from the Moldflow database, except for the viscosity, which was taken from the report of Lin [124]. The 3D model was first created by a CAD program (Creo), and was meshed by creating triangular elements (1002237 elements) as demonstrated in

figure 4.3a. The measurement of cooling was performed at the center of the injection molded part just right behind the melt front as shown in figure 4.3b.

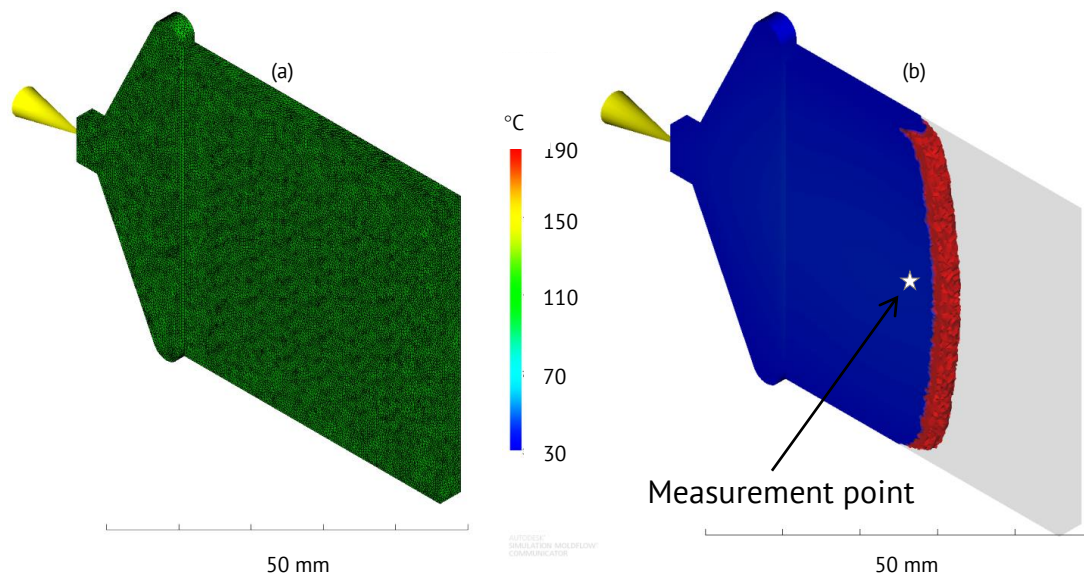


Figure 4.3: 3D mesh model (a) and measurement point (b) used in the simulation

## 4.5 Characterization of the Morphology

### 4.5.1 Optical Microscopy

Thin sections which have been prepared in according to 4.3.1 scheme A were immersed in oil between glass slide and cover slide and characterized with an optical microscope (ECLIPSE LV100, Nikon GmbH, Düsseldorf, Germany) using polarized light in transmission mode. A minimum of three thin sections was investigated for each composition.

The etched surfaces of samples (Figure 4.2, scheme C) were also investigated by an optical microscope using reflection light microscopy equipped with differential interference contrast (DIC). At least three etched samples were examined. To obtain the average spherulite size, a minimum of 50 spherulites was measured for each composition.

### 4.5.2 Electron Scanning Microscopy

Both etched and ion-polished surfaces of samples were investigated by scanning electron microscopy (SU8000, Hitachi, Japan). After the SEM images of ion-polished samples were recorded, they were analyzed by MATLAB image processing software in order to determine the area covered by nanoparticle agglomerates at each location along wall thickness. The images were firstly converted to a binary image and then the pixels with certain grey level were selected by a defined threshold, and finally the nanoparticles covered area was calculated from the pixel numbers.

### 4.5.3 X-Ray Analysis

Wide-angle X-ray diffraction (WAXD) and small-angle X-ray scattering (SAXS) were performed using a Xenocs Xeuss 2.0 (Xenocs, Sassenage, France) with an integrate X-ray microfocus & X-ray optics. The CuK $\alpha$  radiation source (wavelength of 1.5418 Å) was utilized at room temperature.

To evaluate the SAXS data, the one-dimensional scattering function was obtained by the Lorentz correction:

$$I_1(s) = 4\pi q^2 I(s) \quad (13)$$

where  $I_1(s)$  is the one-dimensional scattering function,  $I(s)$  is the measured intensity function, and  $q$  is scattering vector.

The long period ( $L$ ) is related with the position of the scattering peak, which can be calculated using the Bragg's law:

$$L = \frac{2\pi}{q_{\max}} \quad (14)$$

The thickness of crystalline lamellar,  $l_c$ , can also be determined as follows [130];

$$l_c = X_c L \quad (15)$$

## 4.6 Characterization of the Crystallization

### 4.6.1 Polarized Light Microscope Equipped with Heating Stage

In order to study the spherulitic development of the materials, thin section of 10  $\mu\text{m}$  (Figure 4.2, scheme A) were applied onto a glass substrate and covered by a cover slip. Then the materials were analyzed under transmitted light using an optical microscope (ECLIPSE LV100, Nikon GmbH, Düsseldorf, Germany).

The solidification process of the materials as obtained from non-isothermal crystallization and the spherulite growth rate as obtained from isothermal crystallization were observed by the same polarized light microscope equipped with a heating stage (LTS 420, Linkam Scientific Instruments, Surrey, England). The development of the spherulitic structure was recorded by a CCD camera.

The samples were heated to 200°C at a rate of 20 K/min and held for 3 min at this temperature. Then, for non-isothermal crystallization the material was cooled to 30°C at 20 K/min.

For isothermal crystallization, the samples were cooled at the rate of 20 K/min to various given crystallization temperatures (130°C, 132°C and 134°C) and held constant until completion of crystallization was observed. The radial growth rate of the spherulites was calculated using the recorded movies to measure the size of PP spherulites as a function of time. Five spherulites of each sample were characterized.

Each crystallization experiment was performed at least 3 times in order to verify the reproducibility of the experiment.

### 4.6.2 Differential Scanning Calorimetry

The thermal properties were determined using DSC (TA Q20, TA instruments, Eschborn, Germany) equipped with the Refrigerated Cooling Systems 90 (RCS90). An indium was used as a reference material to calibrate both the temperature scale and the melting enthalpy before the samples were measured in alternate runs. The calorimeter was purged with nitrogen gas throughout the measurement. The weight of each sample, see Figure 4.2 (schematic B), was 5 to 10 mg, which corresponds to 3-5 thin sections. Each sample was placed in an aluminium pan and the pan was then completely sealed with an aluminium lid.

In order to ensure the complete melting of the previous crystals and to erase their process history, preliminary experiments have been done under non-isothermal condition. In this experiment, the neat PP samples were heated to a holding temperature of 220°C at a rate of 10 K/min. The samples were held at 220°C for a specified holding time, ranging from 1 to 30 minutes, before being cooled at a rate of 10 K/min to 0°C. The crystallization temperature,  $T_p$ , defined as the peak of DSC exotherm during cooling scan, is used to indicate the effect of the holding conditions on the melt completion of the previous crystals. A variation of the holding time did not affect the crystallization temperature when the holding time beyond 3 min. Therefore, the holding time for 3 minutes was chosen in this work.

### Isothermal Crystallization

For isothermal investigation, the samples were heated to 220°C at a rate of 20 K/min. The holding time of 3 minutes at 220°C was selected to remove the processing history. The samples were then quenched at a rate of 40 K/min to various isothermal crystallization temperatures ( $T_i$ ) within the range of 128°C - 134°C, and kept constant

at that temperature until the crystallization was completed. The heat evolved during the isothermal crystallization ( $H_c$ ) was recorded as a function of time. The time required for each isothermal crystallization conditioning depended on the value that had been chosen for  $T_i$ .

After the crystallization completed, the samples were heated to 220°C at a rate of 20 K/min to observe its melting behavior. The melting temperature ( $T_m$ ) of the samples was obtained from the maximum of the endothermic peaks. The equilibrium melting temperature ( $T_m^\circ$ ) was determined from Hoffman-Weeks plot using the extrapolation plot of  $T_p$  and  $T_m$ .

### Non-isothermal Crystallization

The microtomed sample was initially heated from 0 to 220°C at the rate of 10 K/min. To minimize thermal degradation each sample was used only one time. Dependence of cooling rate studies was performed at a specified cooling rate, ranging from 2 to 40 K/min. The degree of crystallinity was calculated using the following equation:

$$(\%X_c) = (\Delta H_f / \Delta H_f^\circ w) \times 100 \quad (16)$$

where  $\Delta H_f$  is the heat of fusion of the sample (J/g),  $\Delta H_f^\circ$  is the heat of fusion of a theoretically 100% crystalline PP (209 J/g) [130], and  $w$  is the mass fraction of PP in the nanocomposite.

DSC melting endotherms was used to calculate the lamellar thickness distribution by using Gibbs-Thomson equation [132]:

$$T_m = T_m^\circ \left(1 - \frac{2\sigma_e}{\Delta H_f L}\right) \quad (17)$$

All parameters are the same meaning as discussed previously. According to the literature [133], 185.2 °C and 0.07 m/J<sup>2</sup> are used for  $T_m^\circ$  and  $\sigma_e$ , respectively, which was used in this work.

### 4.6.3 Flash Differential Scanning Calorimetry

Crystallization experiments were performed using a power compensation differential fast scanning chip calorimetry (FLASH DSC 1, Mettler Toledo, Gießen, Germany) in combination with a Huber Intracooler TC100. Samples were cut from the center part of injection-molded plate. Dry nitrogen was used as a purge gas at a rate of 30 mL min<sup>-1</sup>. The sample was placed directly on the sensor. In order to provide a good thermal contact between the sample and the sensor, the sample was molten at heating rate of 0.1 K/s before the actual experiments. Therefore, the information on the original state (processing history) of the test sample is lost. The recommended procedures were described in details in literatures [134-135]. Samples with a thickness of about 10-20 µm and lateral dimension of about 50 µm were prepared.

### Isothermal Crystallization

To study the isothermal crystallization of material, the test sample was heated to 220°C at a rate of 1000 K/s and kept at that temperature for 0.1 seconds to remove the processing history. The samples were then quenched at a rate of 4000 K/s to the target isothermal crystallization temperatures ( $T_i$ ) within the range of 0°C - 150°C, and kept constant at that temperature until the crystallization was completed.

### **Non-isothermal Crystallization**

Samples were heated to 220°C at a rate of 1000 K/s, and were kept at this temperature for 0.1 s, then cooled to -90°C at various cooling rates. The desired cooling rate range was between 0.5 to 4000 K/s. The crystallization temperature ( $T_p$ ) was determined by the maximum exothermal crystallization peak.

### **4.7 Characterization of the Mechanical Properties**

With the thin section prepared in according to 4.3.1, (Figure 4.2, scheme A), micro-tensile tests were conducted using a micro-tensile testing machine (Kammrath & Weiss GmbH, Dortmund, Germany) using a cross-head speed of 20  $\mu\text{m/s}$ . During the micro-tensile testing, the load value was saved as a function of time through a PC-controlled microprocessor connected to the computer. At the same time, the deformation of sample was recorded by a CCD camera of light microscope. The values of all the mechanical parameters were determined as averages over five samples for each material.

## 5. Results and Discussion

### 5.1 Simulation of Injection Molding

In the present work, Moldflow is used for simulating the filling of the injection molding. All physical properties of the polymer used in the simulation were taken from the Moldflow database, except for the viscosity, which was taken from the report of Lin [125]. Figure 5.1 shows the Moldflow simulated temperature distribution across the sample thickness of PP-V0 at the center of the molding at the end of the simulation. In this case, the cooling starts as the flow front hits the 50% of filling stage.

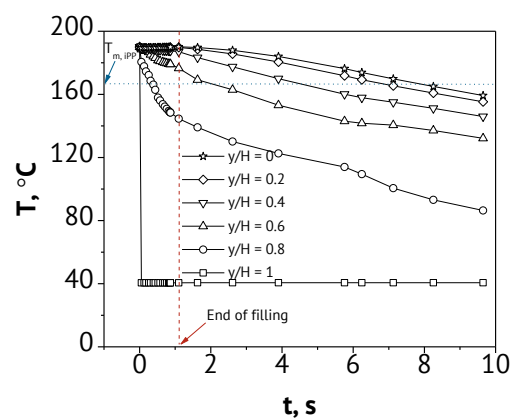


Figure 5.1: Temperature distribution as a function of time through the thickness of the 4 mm thick cavity predicted by Moldflow for neat PP.

Based on the temperature profile, the cooling rate distribution across the sample thickness as a function of time can be calculated and is listed in table 5.1. As it can be seen in table 5.1, during the molding cycle, when a polymer melt gets into contact with the cold wall of the mold, the material is subjected to cools very rapidly. In this case the crystallization can be investigated by using flash differential scanning calorimetry (above 1 K/s). The material cools down more slowly towards the center of the polymer

product. At the core of the component, the cooling rate at this location is in a range of conventional DSC performance (less than 1 K/s). Therefore, the crystallization can be investigated by using conventional DSC.

Table 5.1 Cooling rate (K/s) along the thickness of an injection molded neat PP plate ( $y/H = 0$  = center of the plate;  $y/H = 1$  = layer attached to the mold cavity) at a flow length of 50% as a function of time

t, s	y/H ratio					
	1	0.8	0.6	0.4	0.2	0
0.0	2873.9	182.6	28.6	16.2	11.6	9.4
0.1	1436.9	109.5	16.3	8.5	5.7	4.7
0.2	0.0	46.0	11.7	1.7	0.2	0.3
0.3	0.0	49.6	20.1	1.3	0.2	0.4
0.4	0.0	46.3	16.2	2.2	0.2	0.6
0.5	0.0	47.5	14.2	3.3	0.5	0.8
0.6	0.0	31.2	8.5	2.9	0.4	0.6
0.7	0.0	29.0	7.5	2.0	0.3	0.5
0.8	0.0	24.9	6.2	0.9	0.2	0.3
0.9	0.0	19.4	5.1	0.4	1.9	2.2
1.1	0.0	13.5	12.3	4.9	0.9	0.1
1.6	0.0	9.8	10.1	6.5	2.6	1.3
2.6	0.0	7.5	7.0	5.9	3.5	2.4
3.9	0.0	5.1	6.6	5.6	4.3	3.5
5.5	0.0	5.2	5.0	5.2	5.0	4.5
7.1	0.0	8.3	2.2	3.3	4.2	4.4
8.3	0.0	5.7	3.3	3.6	4.0	4.2
9.6	0.0	4.8	3.6	3.7	4.0	4.1

Due to a variation of cooling rate from the edge to the center of the polymer product, a combination of conventional and flash DSCs used in this work can cover a wide range of crystallization behaviors as the following section.

## 5.2 Quiescent Crystallization Kinetic

### 5.2.1 Isothermal Crystallization Analysis

#### Isothermal Crystallization Kinetics by Half-Time of Crystallization

Figure 5.2 and 5.3 show selected examples of the exothermic crystallization of neat and nano-filled PP at different temperatures obtained from conventional and flash DSCs, respectively. As is can be seen, with increasing nanoparticle loading as well as with decreasing crystallization temperature, the exothermic crystallization shifts towards shorter time. This implies that the time required to complete the crystallization is shorter and that the crystallization rate is faster when the nanoparticle loading is higher and the crystallization temperature is lower.

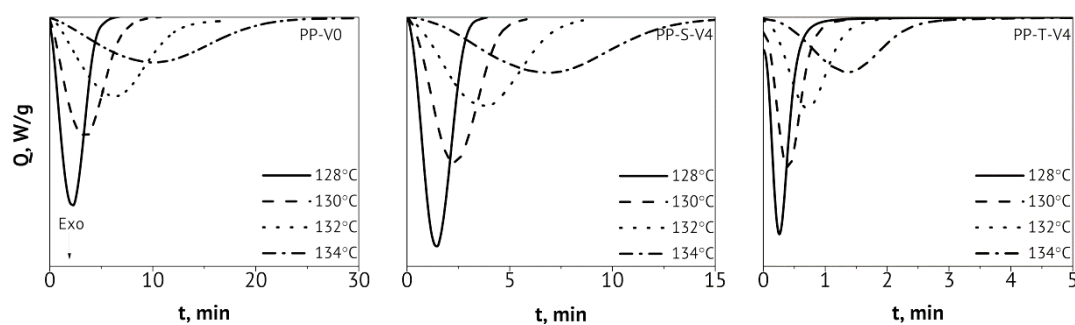


Figure 5.2: Typical crystallization exothermic data of materials under isothermal crystallization conditions measured with DSC.

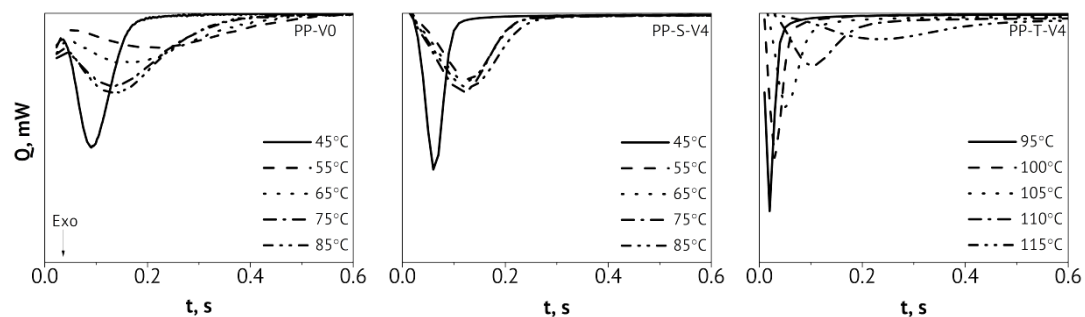


Figure 5.3: Typical crystallization exothermic data of materials under isothermal crystallization conditions measured with flash DSC.

From Figures 5.2 and 5.3, the half-time of crystallization ( $t_{1/2}$ ), defined as the time spent from the beginning of the crystallization process to the completion of half of the final total crystallization, can be determined as shown in Figure 5.4. It is important to note that the inverse of the half-time of crystallization ( $1/t_{1/2}$ ) is usually used to determine the overall rate of the crystallization process directly. A higher value of  $t_{1/2}$  means a slower rate of crystallization, and vice versa.

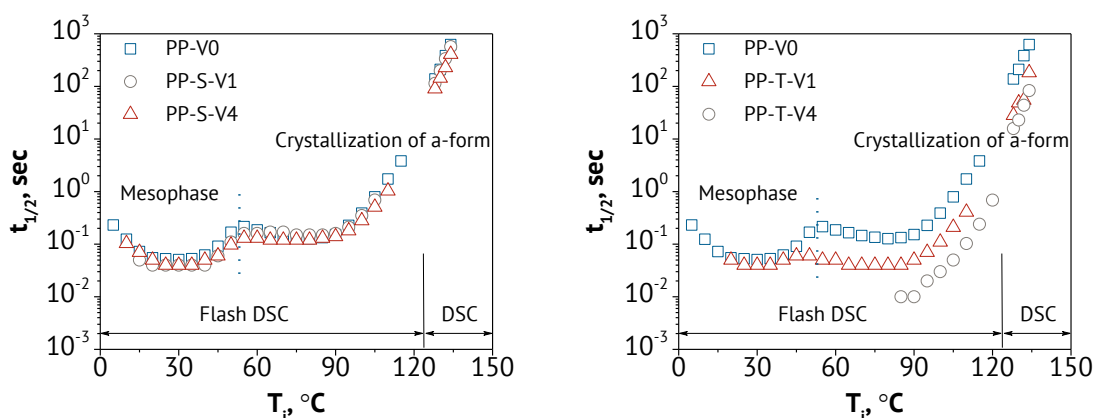


Figure 5.4: The  $t_{1/2}$  as a function of temperature for neat and nanoparticle-filled PP.

All materials exhibit a bimodal behavior, except PP-T-V4, corresponding to maximum rates of crystallization of the  $\alpha$ -phase (higher temperature) and the formation of a mesophase (lower temperature) [83, 136]. Crystallization is commonly occurred between the melting temperature and glass transition temperature.

At high temperature ( $T_i > 55^\circ\text{C}$ ), as expected, the  $t_{1/2}$  decreases with decreasing  $T_i$  in all cases. This shows that a lower  $T_i$  results in a faster crystallization rate due to an increase in supercooling,  $\Delta T = T_m^\circ - T_i$ . Supercooling is proportional to the free energy of melting which is the driving force for crystallization. With increasing supercooling,  $\Delta T$ , the  $t_{1/2}$  decreases due to the increasing thermodynamic driving force of crystallization, resulting in an increase in nucleation density and/or spherulite growth rate and consequently, an increase in the overall crystallization rate [137-138]. It

passes through a minimum, and then increases due to the decreasing mobility of chain segments [40]. Figure 5.4 also reveals that the presence of the nanoparticles increases the crystallization rate of  $\alpha$ -phase compared to the neat PP. The crystallization process of PP is only slightly faster in the presence of the SiO<sub>2</sub> nanoparticles, whereas the increase of the crystallization rate of PP is much more pronounced in the presence of the TiO<sub>2</sub> nanoparticles. This is in relation to the nucleating action of added nanoparticles especially of TiO<sub>2</sub>. When the nanoparticle loading is higher, the number of nuclei per unit PP volume increases, and therefore the crystallization rate increases [139]. However, the crystallization of PP-T-V4 is restricted up to the temperature of 85°C. At temperatures lower than 85°C, the crystallization is too fast to be quantified with flash DSC used in this work. This high temperature region can therefore be assigned to crystallization via heterogeneous nucleation.

At low temperature ( $T_i < 55^\circ\text{C}$ ), a faster crystallization process occurs. However, the increase of the crystallization rate at low temperature (or mesophase) is not influenced by the presence of nanoparticles. This is because homogeneous nucleation is dominant and orders of magnitude more stable homogeneous nuclei are present in this temperature range. The low temperature region represents the crystallization via homogeneous nucleation [84].

In addition, the transition from crystallization of  $\alpha$ -phase to mesophase formation, which is a change of the nucleation mechanism from heterogeneous nucleation at high temperature to homogeneous nucleation at low temperature, is at around 50-55°C. The temperature at the maximum rate of crystallization of the  $\alpha$ -phase and of the formation of the mesophase is about 80-85°C and 30°C, respectively. The results are in agreement with a previous report from Schawe [83]. However, the transition from crystallization of  $\alpha$ -phase to mesophase formation and the temperature of maximum

rate of crystallization of the  $\alpha$ -phase and of the formation of the mesophase are barely influenced by the presence of nanoparticles.

The dependency of the crystallization half-time of the  $\alpha$ -phase (temperature range 55°C to 150°C) on the filler content and the crystallization temperature can be mathematically described by the following equation:

$$t_{1/2} = e^{(a+bT^{1.5}+cv_f)} \quad , \text{ for SiO}_2\text{-filled PP} \quad (18)$$

$$t_{1/2} = e^{(a+bT^{2.5}+ce^{-v_f})} \quad , \text{ for TiO}_2\text{-filled PP} \quad (19)$$

where  $v_f$  and  $T$  are the volume percentage of filler loading and the given crystallization temperature, while

$a = -17.094452$ ,  $b = 0.015177269$ , and  $c = -0.11092523$ , for SiO<sub>2</sub>-filled PP, and

$a = -10.07733$ ,  $b = 6.946957$ , and  $c = 2.0846683$ , for TiO<sub>2</sub>-filled PP.

are specific constants, which are determined from the fitting of experimental data from figure 5.4. It can be clearly seen that the simple equation (18) and (19) allow to predict the temperature and the filler loading dependency of the crystallization of nanoparticle-filled PP. Either a decrease of crystallization temperature or an increase in filler loading can result in a decrease of the crystallization half-time.

### **Isothermal Crystallization Kinetics based on Avrami and Its Modification**

The fractional degree of crystallinity  $X(t)$  at time  $t$  was determined from the ratio of the peak area at  $t$  to the total area of an exothermic peak. A slow increase of crystallinity with time after most of the crystallization had taken place is observed and this is attributed to the presence of secondary crystallization [62]. This fractional crystallinity curve is fitted with macrokinetic model in order to obtain the information of kinetics. The crystallization kinetics of PP and its nanocomposites under isothermal conditions

for various modes of nucleation and growth can be well approximated by the well-known Avrami model and its modification, i.e. Tobin and Malkin models. As it can be seen in figure 5.5, the deviation of the fits from the experimental data using Tobin is obvious, while that based on Avrami and Malkin is much less pronounced.

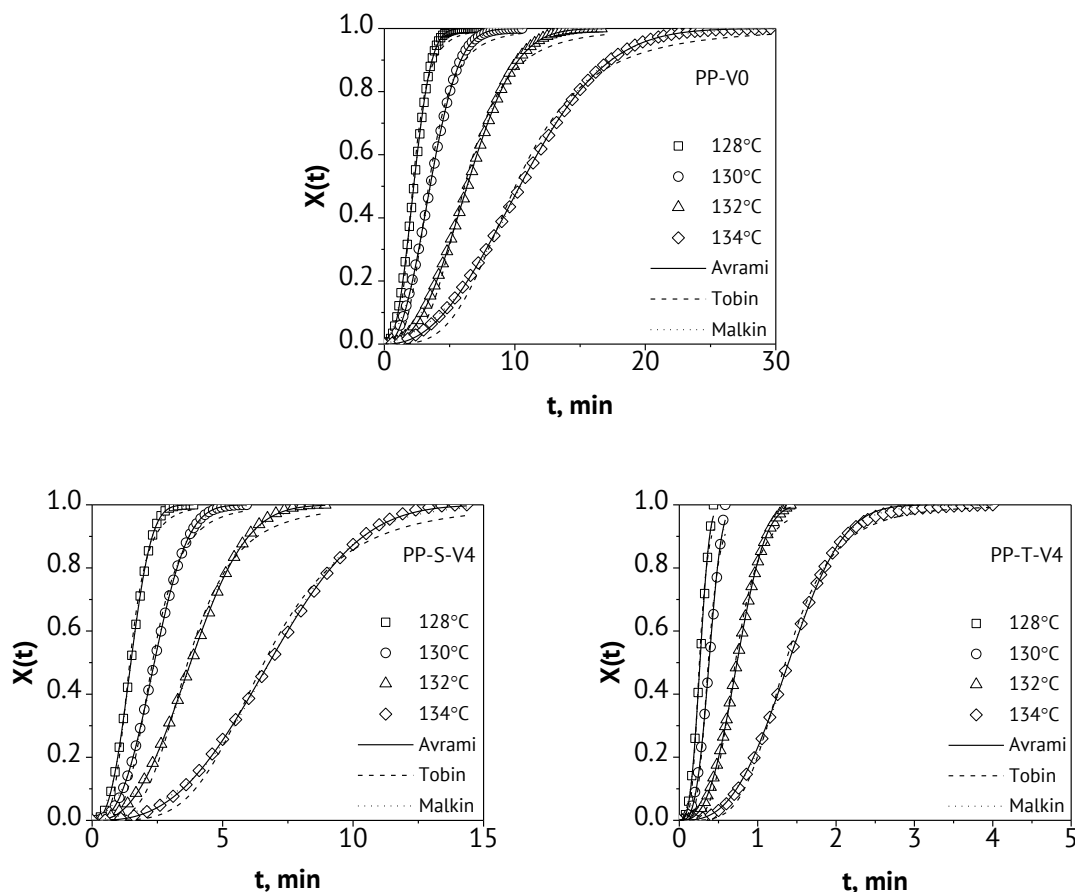


Figure 5.5: Relative crystallinity as a function of time of PP-V0, PP-S-V4, and PP-T-V4 for four crystallization temperatures and fit with well-known macrokinetic models.

Although the Tobin model takes growth impingement into account, the result is a less than satisfactory fit for the experimental data for all samples. In contrast, the Avrami model provides a good fit for the experimental data when  $X(t) < 0.9$ , but it overestimated the data when  $X(t) > 0.9$ . This deviation is due to the occurrence of secondary crystallization at a later stage [62]. However, the Malkin model seems to

provide a good fit for the experimental data when  $X(t) = 0.1 - 1.0$ , but this model overestimates the data when  $X(t) < 0.1$  (see Appendix).

The quality of the model predictions for the experimental data is quantitatively represented by the values of the correlation coefficient  $R^2$ , shown in table 5.2. The closer the value of  $R^2$  approximates 1, the better the quality of the fit.

Table 5.2 Summary of  $R^2$  parameter suggests the quality of the fit for neat,  $\text{SiO}_2$ -, and  $\text{TiO}_2$ -filled PP

Sample	$T_c$ , °C	Avrami	Tobin	Malkin
PP-V0	128	0.99995	0.99446	0.99967
	130	0.99997	0.99430	0.99972
	132	0.99996	0.99397	0.99967
	134	0.99993	0.99364	0.99976
PP-S-V1	128	0.99989	0.99282	0.99921
	130	0.99998	0.99478	0.99968
	132	0.99992	0.99319	0.99931
	134	0.99989	0.99289	0.99948
PP-S-V4	128	1	0.99522	0.99958
	130	1	0.99484	0.99961
	132	0.99993	0.99319	0.99954
	134	0.99991	0.99327	0.99930
PP-T-V1	128	0.99979	0.99368	0.99894
	130	0.99952	0.99739	0.99938
	132	0.99943	0.99829	0.9995
	134	0.99701	0.9995	0.9975
PP-T-V4	128	0.99887	0.99041	0.99746
	130	0.99762	0.9869	0.99593
	132	0.99995	0.99504	0.99937
	134	0.99961	0.99774	0.99970

For all samples, the  $R^2$  values obtained using the Tobin model is lower than those from the other two. This indicates that the Tobin model produces a poorer fit than the other

models. In addition, the  $R^2$  values of the Avrami model are higher than those of Malkin model. The conclusion which can be drawn based on the  $R^2$  values is that the Avrami model provides the best description over the entire range of the crystallinity data for all samples with the highest  $R^2$  values. However, in this case it has to be proven, that the model also fits at high cooling speeds or low crystallization temperatures, respectively.

According to the theory, Avrami exponent  $n_a$ , which plays a key role for the kinetic of the crystallization process, depends on whether the growth rate is constant with time and it also reflects whether a nucleation process takes place continuously or crystallization takes place on a certain number of active places [140]. In this work, the  $n_a$  can be extracted from the slope of the plot. Only the linear portion range from 0.1 to 0.9 is observed, whereas the curvature at the earlier and the later stage of crystallization is found. This deviation implies that the  $n_a$  is changed [141]. The difference in the local  $n_a$  of each stage of crystallization reflect the change in the nucleation rate and/or the growth morphology. At the earlier stage, the curvature implies the problems of establishing temperature and of establishing the steady state [140]. For this reason the small deviation can be seen in the application of Avrami model, and is even aggravated in the application of Malkin model. Furthermore, the curvature at the later stage attributes to the occurrence of secondary crystallization, which results from spherulite impingement at the latter stage of the primary crystallization, decreasing the crystallization rate. As mentioned earlier, Avrami model is based on a simplified assumption that there is free crystal growing in all directions. Therefore, the Avrami model is only appropriate for the primary stage of crystallization, and the deviation at the later stage is always present. On the other hand, the Malkin model attempts to take the concept of secondary crystallization into consideration. However, the Malkin model still underestimates slightly the experimental data at the later stage of crystallization. This underprediction could be due to an overemphasis of

the secondary crystallization effect and the mathematical simplification of Malkin model.

Table 5.3 The average values of  $n_a$  for the entire course of crystallization

Sample	$T_i, ^\circ\text{C}$			
	128	130	132	134
PP-V0	2.5	2.3	2.5	2.3
PP-S-V1	2.7	2.6	2.7	2.7
PP-S-V4	2.7	2.7	2.6	2.8
PP-T-V1	2.8	2.7	2.7	2.6
PP-T-V4	3.1	3.4	2.9	2.9

According to table 5.3, the average values of  $n_a$  are almost independent of the temperature for all samples. On the other hand, an incorporation of nanoparticles increases the values of  $n_a$ . This implies that the nanoparticle changes the mechanism of nucleation and the geometry of the growing crystals. Because of the change of instantaneous to sporadic nucleation, an increase in the value of  $n_a$  is usually observed [62]. In the three-dimensional heterogeneous crystal growth, the value of  $n_a$  would be close to 3. Though the value of  $n_a$  ranges between 2 and 3 ( $2 < n_a < 3$ ), suggest whether or not there is a heterogeneous nucleation with two-dimensional diffusion controlled growth [62, 144].

### **Isothermal Crystallization Kinetics based on the Lauritzen-Hoffman Theory**

As discussed above, the Avrami model can well describe the bulk crystallization kinetics of polymers, but it is a phenomenological model with no molecular-level description of the process taking place during crystallization. The Lauritzen-Hoffman theory suggests the crystallization is controlled by nucleation and transport of the macromolecules in

the melt. For polymer crystallization, the driving force mainly comes from the internal energy generated from the excess of thermodynamic free energy in the system, which comes from the transport of the molecules from the disordered phase to the ordered phase, and from the rotation and rearrangement of the molecules at the surface of the ordered phase [142].

In order to obtain the nucleation parameter in the polymer crystallization process, the equilibrium melting temperature ( $T_m^\circ$ ) is needed to calculate the degree of supercooling. Hoffman and Week plots are used to determine based on the observed linear relation between the  $T_m$  and  $T_c$ . Figure 5.6 shows the Hoffman-Weeks plots (equation (11)) of neat and nanoparticle-filled PP showing the extrapolation of the equilibrium melting temperature. The resulting data are listed in table 5.4.

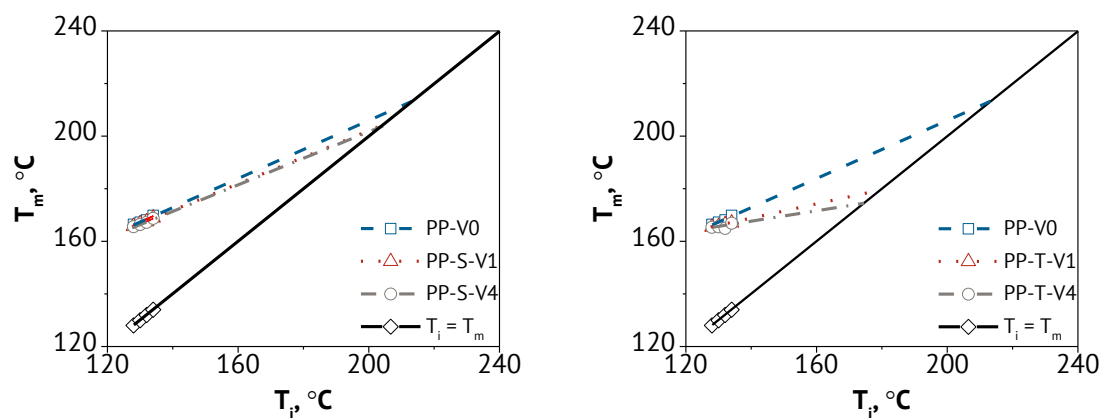


Figure 5.6: Hoffman-Weeks plots of neat and  $\text{SiO}_2$ -filled PP (left) and  $\text{TiO}_2$ -filled PP (right).

For neat PP, a  $T_m^\circ$  of  $213.6^\circ\text{C}$  is observed. This is in qualitative agreement with previous data ( $212\text{-}215^\circ\text{C}$ ) from literatures [4, 143]. It is clear that the incorporation of nanoparticles causes a decrease in  $T_m^\circ$  of PP. This can be concluded that increasing the nanoparticle content increases the number of defects between PP lamellae (less perfect crystals). Similar results were also observed when several fillers were added

into PP [4, 144-145]. However, the effect of SiO<sub>2</sub> on T<sub>m</sub><sup>o</sup> of PP is smaller than TiO<sub>2</sub>. The data are further useful in estimating the free surface energy of nucleation based on Lauritzen-Hoffman theory in the following section.

Table 5.4: Values of the equilibrium melting temperature, T<sub>m</sub><sup>o</sup> of neat and nanoparticle-filled PP

<b>Samples</b>	<b>T<sub>m</sub><sup>o</sup>, °C</b>
PP-V0	213.6
PP-S-V1	204.8
PP-S-V4	204.7
PP-T-V1	179.4
PP-T-V4	174.6

The above results reveal the effects of the nanoparticles on the entire crystallization rate ( $1/t_{1/2}$ ), which is known to include contributions from both nucleation and growth. In order to understand further the effect of the nanoparticles on the entire crystallization, the nucleation barrier (the work required for formation of nuclei) is evaluated using the Lauritzen-Hoffman theory. This is particularly relevant to the crystallization of the  $\alpha$ -phase. As described above, the crystallization of the  $\alpha$ -phase is controlled by the heterogeneous nucleation, while the homogeneous nucleation is dominant for the formation of the mesophase. Figure 5.7 demonstrates the Lauritzen-Hoffman plot according to equation (10) for isothermal crystallization of materials. As seen in figure 5.7, the experimental data can be reasonably fitted with a straight line for all materials. The nucleation parameter,  $K_g$ , can be obtained from the slope of the fitting line and the values are listed in table 5.4.

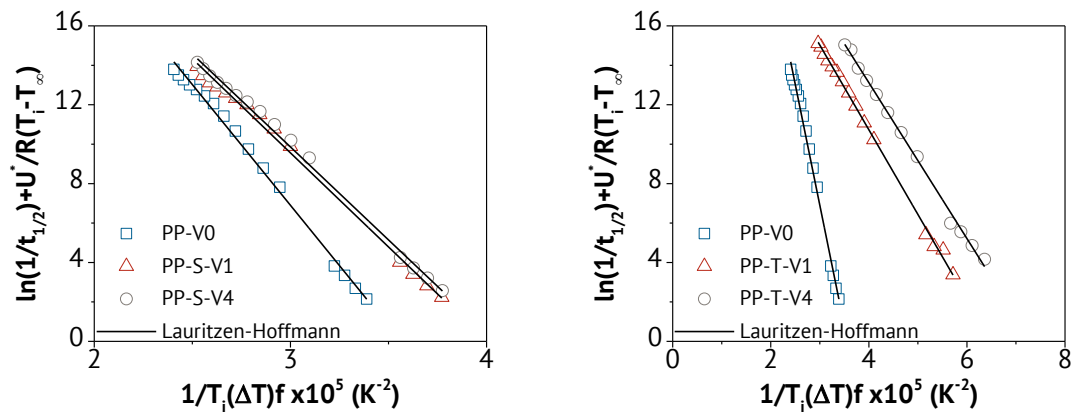


Figure 5.7: Lauritzen-Hoffman plots for neat and nanoparticle-filled PP

Table 5.5: Values of  $K_g$  and  $\sigma_e$  for neat and nanoparticle-filled PP

Sample	$K_g \times 10^{-5}, K^2$	$\sigma_e, \text{mJ/m}^2$
PP-V0	12.2	23.3
PP-S-V1	9.5	18.5
PP-S-V4	9.4	18.3
PP-T-V1	4.3	8.8
PP-T-V4	4.0	8.2

$K_g$  represents the free energy necessary to form a nucleus of critical size. The  $K_g$  value for neat PP is in good agreement with the  $K_g$  being about  $10 K^2$  of PP reported by Papageorgiou et al. [65]. A small decrease in  $K_g$  value of PP can be also observed with the addition of  $\text{SiO}_2$  nanoparticles. Moreover, the  $K_g$  decreases greatly with an incorporation of  $\text{TiO}_2$  nanoparticles by the factor of 3. The result implies that the presence of the nanoparticles reduces the work needed to create a new surface leading to faster crystallization rates [65]. The obtained  $K_g$  values can be used to calculate the fold surface free energy,  $\sigma_e$  of materials from equation (9) and the values are listed in table 5.5. As seen in table 5.5, the  $\sigma_e$  decreases with the addition of nanoparticles. A foreign surface frequently reduces the nucleus size needed for crystal growth. This is

because the creation of the interface between polymer crystal and substrate may be less hindered than the creation of the corresponding free polymer crystal surfaces. A heterogeneous nucleation path makes use of a foreign pre-existing surface to reduce the free energy opposing primary nucleation [146]. As a result, the value of  $\sigma_e$  is reduced, thereby giving rise to an increase in crystallization rate. In this study, the addition of 1 and 4 vol.% of  $\text{TiO}_2$  gives a 62 and 65% reduction in  $\sigma_e$  of PP. However, the reduction in  $\sigma_e$  is not so high with the addition of  $\text{SiO}_2$ , which gives 22 and 23% reduction for 1 and 4 vol.% of  $\text{SiO}_2$ . The results indicate that the nucleating effect of  $\text{TiO}_2$  in PP is much stronger than that of  $\text{SiO}_2$  in PP and the nanoparticle loading has less influence on the  $\sigma_e$  of PP.

## 5.2.2 Non-Isothermal Crystallization Analysis

### Effect of Cooling Rate on Crystallization

Figure 5.8 and 5.9 show the typical curves of heat flow as a function of temperature obtained during cooling at different cooling rates of neat PP, PP-S-V4 and PP-T-V4 using conventional and flash DSCs, respectively.

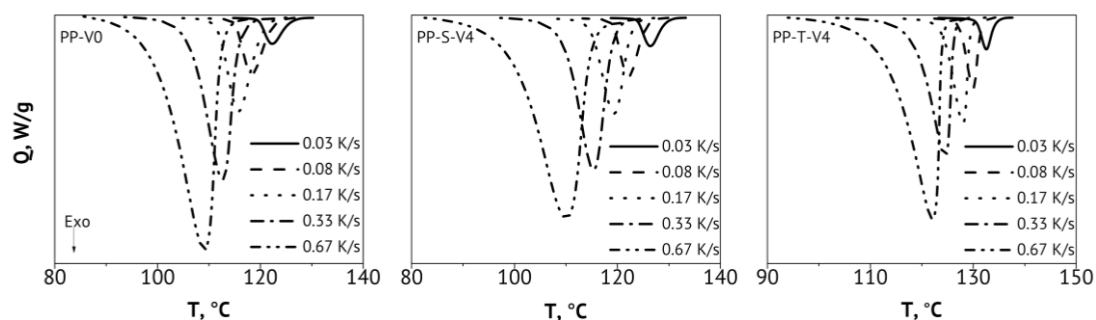


Figure 5.8: Cooling curves of neat PP, PP-S-V4 and PP-T-V4 measured with conventional DSC recorded at different cooling rates.

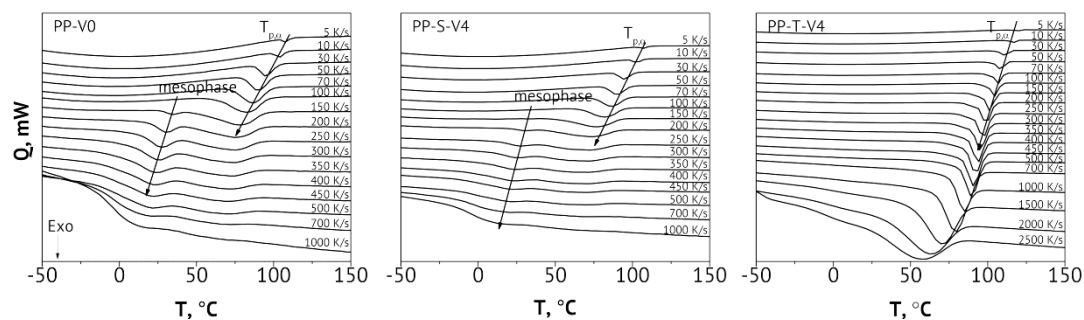


Figure 5.9: Cooling curves of neat PP, PP-S-V4 and PP-T-V4 measured with Flash DSC recorded at different cooling rates.

The plots show that in the case of neat PP only one crystallization process can occur at slower cooling rates. In addition, two different crystallization processes can be observed at cooling rates above 100 K/s. The first crystallization process, at high temperature, can be interpreted as the crystallization of the  $\alpha$ -phase of PP. The second one, at low temperature, is the formation of the mesophase [83, 136]. This observation is similar to SiO<sub>2</sub>-filled PP. However, in the case of TiO<sub>2</sub>-filled PP only the crystallization of  $\alpha$ -phase appears regardless of the cooling rate.

From the cooling curves in figure 5.8 and 5.9, the peak of crystallization temperature ( $T_p$ ) can be determined as shown in figure 5.10. It can be observed that the  $T_p$  decreases with increasing cooling rate for all materials. Since the crystallization process is time dependent, at lower cooling rate the macromolecular chains have enough time to change conformation. This fact results in a less energetic arrangement, and the crystallization occurs at higher temperature [147]. The results also indicate that the  $T_p$  of PP changes with the addition of nanoparticles. The  $T_p$  of PP in TiO<sub>2</sub>-filled PP is always higher than that of neat PP, independence of cooling rates. The results show acceleration of crystallization with incorporation of TiO<sub>2</sub> nanoparticles, irrespective of the cooling rate. In case of PP/SiO<sub>2</sub>, the nucleation effect can be observed only at the

cooling rate lower than 100 K/s. Obviously, the nucleation effect of TiO<sub>2</sub> nanoparticles is much more pronounced compared to the incorporation of SiO<sub>2</sub> nanoparticles.

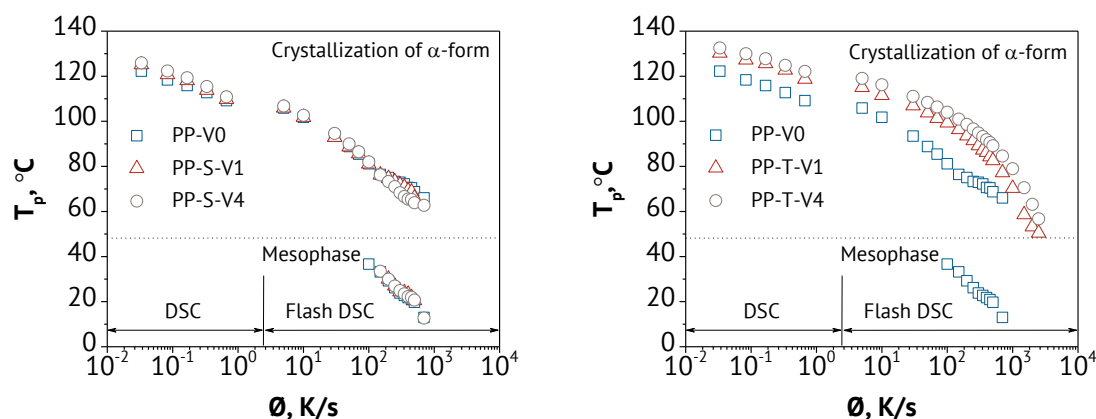


Figure 5.10: Peak of crystallization temperature versus the cooling rate of neat PP and its nanocomposites measured with DSC and Flash DSC.

Furthermore, the data of figure 5.8, 5.9 and 5.10 reveal that the mesophase of PP can be formed at a high cooling rate and it occurs only between about 10°C and 40°C. This is in a good agreement with literature [83, 92]. In addition, the formation of a mesophase is not influenced by the SiO<sub>2</sub> nanoparticles, while it is obstructed by the presence of TiO<sub>2</sub> nanoparticles. Beyond the cooling rate of 700 K/s, the observable crystallization and mesophase formation cannot be expressed in neat and SiO<sub>2</sub>-filled PP. However, crystallization still occurs at a cooling rate of up to approximately 2500 K/s in TiO<sub>2</sub>-filled PP. Therefore, it can be assumed that there is still sufficient molecular mobility to generate the ordering process.

The relationship of  $T_p$  of the  $\alpha$ -phase, filler content and cooling rate can be described by following equation:

$$T_p = a + b \ln \dot{\Theta} + c v_f \quad , \text{ for SiO}_2\text{-filled PP} \quad (20)$$

$$T_p = a + b \dot{\Theta}^{0.5} + c e^{-v_f} \quad , \text{ for TiO}_2\text{-filled PP} \quad (21)$$

whereas

$a = 108.53802$ ,  $b = -6.1889646$ , and  $c = -0.085241429$ , for  $\text{SiO}_2$ -filled PP, and

$a = 125.48139$ ,  $b = -1.5468542$ , and  $c = -20.027344$ , for  $\text{TiO}_2$ -filled PP.

are parameters to be determined from fitting of the experimental data from Figure 5.8. This simplification allows to predict the cooling rate and the filler loading dependency of the crystallization of nanoparticle-filled PP.

One can compare the results of isothermal crystallization in Figure 5.4 to the cooling rate dependence of crystallization in figure 5.10. With neat PP and the  $\text{SiO}_2$ -filled PP, the formation of a mesophase is faster than the crystallization of  $\alpha$ -phase. Therefore, the formation of the mesophase can occur during cooling in neat PP and the  $\text{SiO}_2$ -filled PP [83]. On the other hand, the absence of formation of a mesophase in PP-T-V4 indicates the much faster crystallization of the  $\alpha$ -phase during cooling compared to the rate of mesophase formation. However, in the case of PP-T-V1, the mesophase has enough time to be formed under the desired isothermal conditions while the given cooling rate is quicker than that of the rate of mesophase formation. Therefore, the mesophase of PP in  $\text{TiO}_2$ -filled PP cannot occur during non-isothermal conditions.

### **Non-isothermal Crystallization Kinetics based on the Lauritzen-Hoffman Theory**

In order to estimate the fold surface free energy under different cooling rates, the Lauritzen-Hoffmann equation for isothermal crystallization can be extended to non-isothermal data. Replacing crystallization half-time with peak crystallization time and isothermal crystallization temperature with peak crystallization temperature, the data from figure 5.10 are plotted in figure 5.11 according to equation (10).

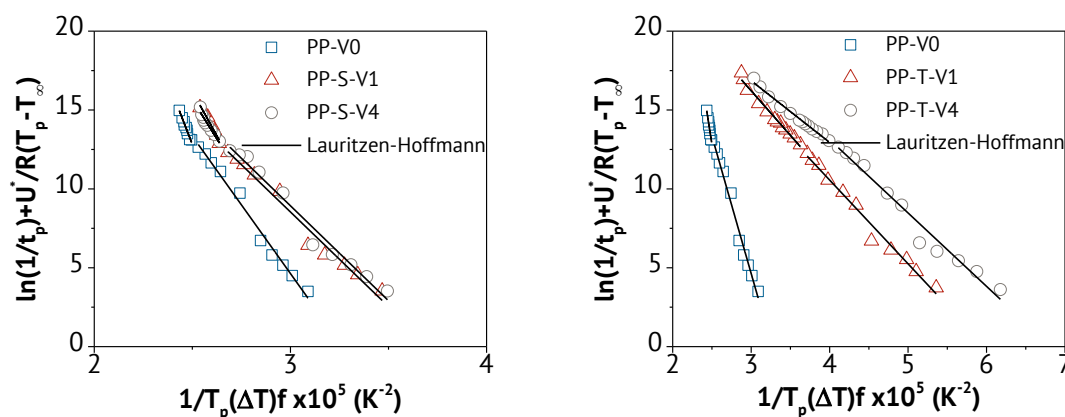


Figure 5.11: Lauritzen-Hoffman plot for non-isothermal crystallization.

One can see that the Lauritzen-Hoffman equation demonstrates discontinuities for neat and SiO<sub>2</sub>-filled PP. However, no such discontinuous variation can be seen for the TiO<sub>2</sub>-filled PP. The observed discontinuity may be attributed to a change in the crystallization mechanism. The Lauritzen-Hoffman values plotted for nanoparticle-filled PP shifted to the right because of the lower supercooling temperature,  $\Delta T$  at which crystallization occurred [148]. To verify any possible change in the crystallization mechanism, determination of parameters at the lower cooling rates and higher cooling rates were performed (results shown in table 5.6). It can be observed from table 5.6 that the values of  $K_g$  and  $\sigma_e$  display a significantly increase at the higher cooling range, which corresponds to a lower crystallization temperature range for neat and SiO<sub>2</sub>-filled PP. In contrast, no significant change in both  $K_g$  and  $\sigma_e$  values for TiO<sub>2</sub>-filled PP occurs.

As observed from table 5.6, both  $K_g$  and  $\sigma_e$  values significantly decrease with the addition of nanoparticles, irrespective of cooling range. However, the decrease in both parameters of PP in the presence of TiO<sub>2</sub> is much higher than in the presence of SiO<sub>2</sub>. This indicates that SiO<sub>2</sub> can act as mild nucleating agent for PP, while TiO<sub>2</sub> can act as very effective nucleating agent for PP. This conclusion is parallel to that obtained from the isothermal analysis.

Table 5.6: Parameters of Lauritzen-Hoffman from non-isothermal crystallization

Sample	$\emptyset$ Range, K/s	T Range, °C	$K_g \times 10^{-5}$ , K <sup>2</sup>	$\sigma_e$ , mJ/m <sup>2</sup>
PP-V0	0.03-100	81-122	17.4	33.1
	150-700	66-76	32.1	61.1
PP-S-V1	0.03-100	81-125	12.0	23.2
	150-700	63-76	22.6	43.8
PP-S-V4	0.03-100	82-126	12.0	23.3
	150-700	63-76	19.9	38.4
PP-T-V1	0.03-100	99-130	5.3	10.9
	150-2500	55-96	5.4	10.9
PP-T-V4	0.03-100	104-133	4.7	9.6
	150-2500	57-101	3.9	8.1

The two sets of data (obtained from isothermal and non-isothermal analyses) are similar. They follow the Lauritzen-Hoffman theory, but the  $K_g$  and  $\sigma_e$  values are not identical. This is because the rearranged and the standard Lauritzen-Hoffman equations differ in a term [148]. The isothermal and non-isothermal data obtained from flash DSC expand the values to much lower crystallization temperature and provide more reliable values of  $K_g$  and  $\sigma_e$  by regressing the Lauritzen-Hoffman equation to the experimental data over a wider temperature range.

### Crystallization Activation Energy

As previously stated, the crystallization of polymer is controlled by two factors: one is the static factor, which is related to the free energy barrier for nucleation and the other is the dynamic factor that is related to the activation energy ( $\Delta E$ ) for the transport of crystalline units across the phase. While the free energy barrier for nucleation is successfully predicted by Lauritzen-Hoffman as discussed above, the activation energy is obtained using the Kissinger method. According to the Kissinger method, the  $\Delta E$ , which is the energy required for the transportation of molecules from a molten state to

a growing crystal surface, for the non-isothermal crystallization of materials can be determined by measuring the decreasing in  $T_p$  as the cooling rate is increased. Figure 5.12 shows the plots based on the Kissinger method, and accordingly the crystallization activation energy could be determined by the slope of these plots,  $-\Delta E/R$ .

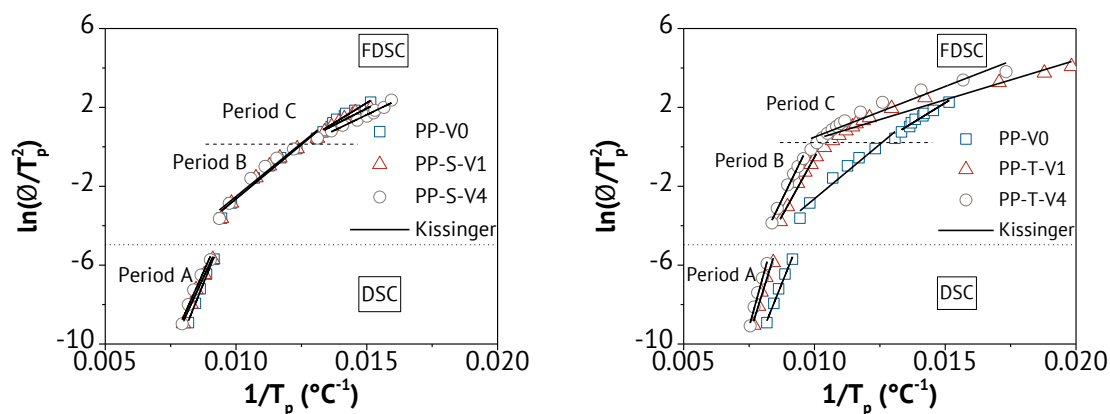


Figure 5.12: Kissinger plots for the evaluation of crystallization activation energy.

In figure 5.12, the data obtained from flash DSC at higher cooling rate are an extension of the conventional DSC. However, the Kissinger plots show a curvature. This indicates that the effective activation energy decreasing at higher cooling rate (lower crystallization temperature). As shown in figure 5.12, three different portions can be defined in order to calculate the activation energy. The results thus obtained are summarized in table 5.7. Since the Kissinger method was formulated for heating experiments (i.e. positive heating rate values), therefore the value of  $\Delta E$  is always negative for the cooling process. As can be seen the absolute values of  $\Delta E$  for  $\text{SiO}_2$ -filled PP are slight smaller than that of neat PP, irrespective of period, which implies that the addition of  $\text{SiO}_2$  into PP probably increases the transportation ability of PP molecular chains during the crystallization process. In contrast, the absolute values of  $\Delta E$  for  $\text{TiO}_2$ -filled PP are greater than that for neat PP at lower cooling rates. However, the absolute value of  $\Delta E$  decreases in a factor of 2 by the presence of the  $\text{TiO}_2$

nanoparticles. The result indicates that at lower cooling rates the PP molecular segments required more energy to rearrange in the presence of TiO<sub>2</sub>, since the TiO<sub>2</sub> might hinder the mobility of chain segments. This may affect the spherulite growth rate of PP during crystallization. In contrast, it helps to increase the transportation ability of PP molecular chains during the crystallization process at higher cooling rates.

Table 5.7: The crystallization activation energies ( $\Delta E$ ) of materials obtained from the Kissinger method

Sample	Period	$\emptyset$ Range, K/s	T Range, °C	$\Delta E$ , kJ/mol
PP-V0	A	0.03-0.67	109-122	398
	B	5-100	81-106	133
	C	150-700	66-76	98
PP-S-V1	A	0.03-0.67	110-125	348
	B	5-100	81-106	132
	C	150-700	63-76	81
PP-S-V4	A	0.03-0.67	111-126	358
	B	5-100	82-107	130
	C	150-700	63-76	77
PP-T-V1	A	0.03-0.67	119-130	512
	B	5-100	99-115	288
	C	150-2500	55-96	48
PP-T-V4	A	0.03-0.67	122-133	578
	B	5-100	104-119	328
	C	150-2500	57-101	62

### Continuous Cooling Transformation

Continuous cooling transformation, CCT, diagrams widely used in metallurgy and solid state phase transformations. These approaches have been applied to predict polymer crystallization under any cooling condition [149-151]. The CCT diagram can be constructed by using the plot of the crystallization peak time and temperature,  $t_p$  and  $T_p$  obtained from various cooling conditions. The CCT diagrams of the materials are shown

in figure 5.13, where the crystallization point as a function of time and temperature is obtained at a constant cooling rate. If the presence of nanoparticle is expected to increase the rate of the crystallization process, then the corresponding CCT curve will shift to a higher temperature.

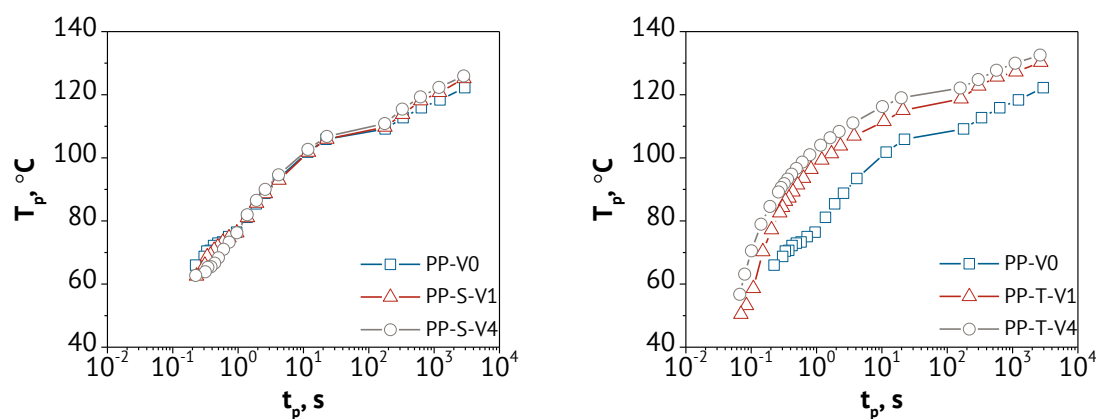


Figure 5.13: CCT diagrams for neat and nanoparticle-filled PP.

In the diagram it can be observed that the crystallization point is reached at higher temperatures for the samples filled with  $\text{TiO}_2$ . This indicates that the  $\text{TiO}_2$  nanoparticles accelerate the crystallization process of PP showing the nucleating effect during the crystallization process. This is a very useful tool for semi-crystalline polymer processing to predict the development of crystallization under any cooling conditions, i.e. under real industrial processing conditions [152].

### 5.2.3 Melting Behaviors and Recrystallization during Heating

It is well known that the shape and the size of crystals formed during cooling is a function of the cooling conditions. The crystal perfection can be indirectly correlated to their melting temperature after non-isothermal crystallization at given cooling rates. Figures 5.14 and 5.15 illustrate the subsequent heating curves of the different PP-

materials after non-isothermal crystallization at various cooling rates measured with conventional and flash DSC, respectively.

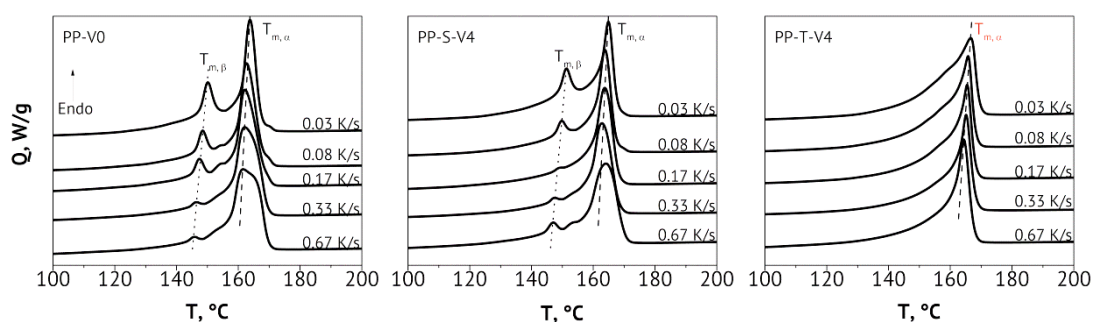


Figure 5.14: Heating curves of neat, SiO<sub>2</sub>- and TiO<sub>2</sub>-filled PP measured with conventional DSC after cooling at various rates.

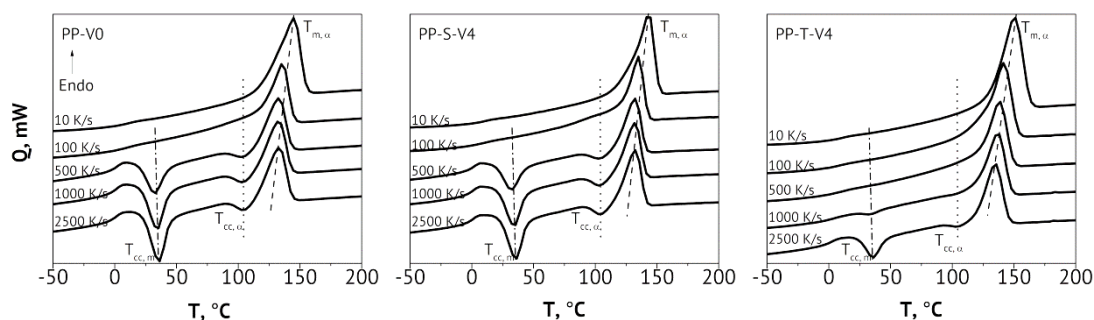


Figure 5.15: Heating curves of neat, SiO<sub>2</sub>- and TiO<sub>2</sub>-filled PP measured with Flash DSC after cooling at various rates.

From the heating curves in figures 5.14 and 5.15, the melting temperature ( $T_m$ ), which is defined as the maximum temperature of the endothermic curve, can be obtained and is plotted in figures 5.16 and 5.17, respectively.

At cooling below 1 K/s as shown in figures 5.14 and 5.16, two dominant endothermic curves can be observed in all materials, except PP-T-V4. The endothermic curve at high temperature (around 160°C) is the melting point of  $\alpha$ -phase ( $T_{m,\alpha}$ ), while the lower one (around 150°C) is the melting temperature of  $\beta$ -phase ( $T_{m,\beta}$ ). It can be seen that a shoulder appears between the  $\alpha$  and  $\beta$  melting points only for neat and SiO<sub>2</sub>-filled PP.

This shoulder is due to the recrystallization of melted  $\beta$ -phase into crystalline  $\alpha$ -phase [20]. As the cooling rate increases, the  $\beta$ -melting peak becomes less pronounced, regardless of the material. However, both the  $\alpha$ - and  $\beta$ -melting peaks increase when the cooling rate decreases, indicating the formation of more perfect or larger crystals [153]. This is because the molecules have enough time to form more perfect crystals at a lower cooling rate.

The  $\beta$ -melting peak seems to be independent of the presence of nanoparticles. However, there is evidence of a trend in which  $T_{m,\alpha}$  increases as the nanoparticles loading increases. The increase in  $T_{m,\alpha}$  of  $\text{TiO}_2$ -filled PP is greater than  $\text{SiO}_2$ -filled PP. It is well known that the stability of crystals can be determined based on the position of the melting temperature. Crystal with greater stability (i.e. thicker lamellae) will melt at a higher temperature [154]. According to the results shown in figure 16, the addition of  $\text{TiO}_2$  provides greater stability of the spherulite compared to neat and  $\text{SiO}_2$ -filled PP.

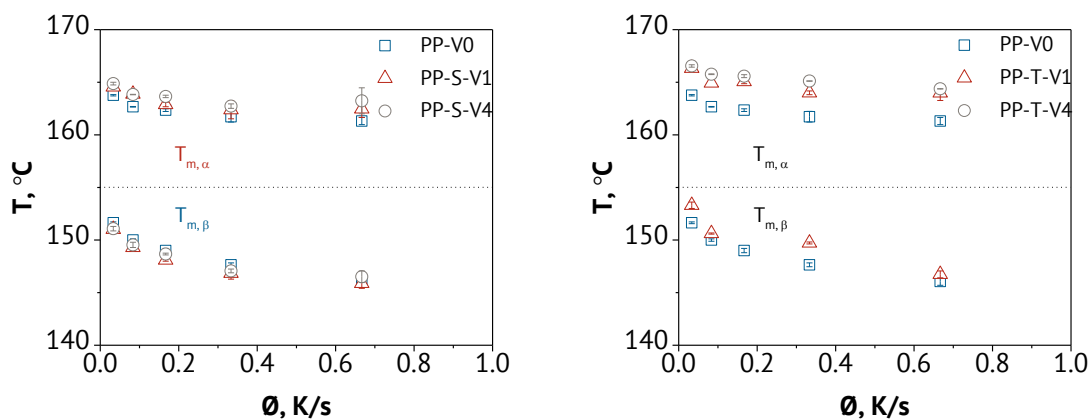


Figure 5.16: Peak of melting temperature as a function of the cooling rate measured with DSC.

From the heating curve measured with flash DSC shown in figure 5.15, only one endothermic peak can be observed after low cooling rates (up to 100 K/s). This peak represents the melting temperature of the  $\alpha$ -phase of PP. After cooling rates higher

than 100 K/s, all the materials except PP-T-V4 exhibit two different exothermic peaks. The first exothermic peak, high temperature, is the crystallization of  $\alpha$ -phase of PP during heating, the so-called cold-crystallization ( $T_{cc,\alpha}$ ). The second one, low temperature, is the formation of mesophase of PP during heating ( $T_{cc,m}$ ) [90, 155]. However, in the case of PP-T-V4 the  $T_{cc,\alpha}$  and  $T_{cc,m}$  can be observed only after very high cooling rates (2500 K/s). All the measured peaks are plotted as a function of cooling rates in figure 5.17. The  $T_{m,\alpha}$  decreases with increasing cooling rate. The  $T_{m,\alpha}$  is barely changed by the presence of  $\text{SiO}_2$  nanoparticles, while it shifts to higher values with increasing  $\text{TiO}_2$  loading. This result is in good agreement with the observation of the DSC analysis in figure 5.14 and 5.16. The incorporation of nanoparticles seems to have no influence on the crystallization of  $\alpha$ -phase and mesophase formation during heating.

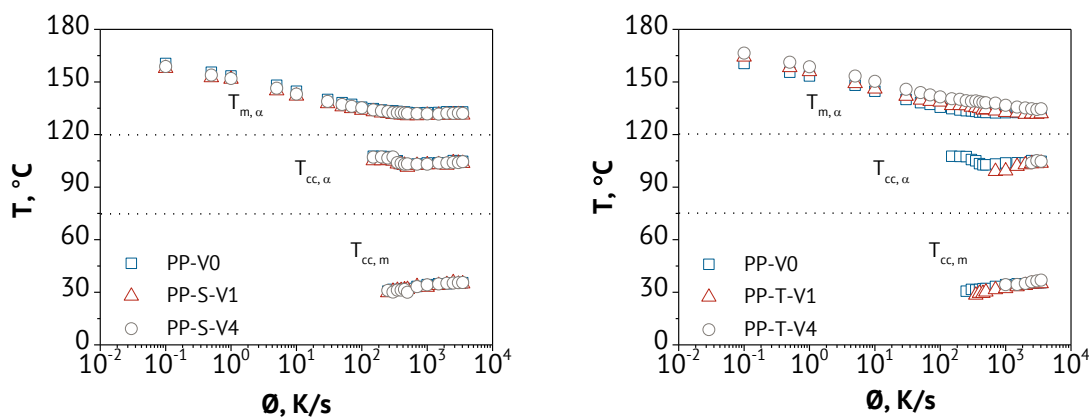


Figure 5.17: Peak of melting temperature and cold-crystallization as a function of the cooling rate measured with flash DSC.

## 5.2.4 Spherulitic Development

### Solidification Process during Non-Isothermal Crystallization

The data obtained from DSC analysis in section 5.2.1 and 5.2.2 prove that crystallization of PP is accelerated by the presence of the nanoparticles. This conclusion can be confirmed by the spherulitic development analysis. Figure 5.18

shows the development of the spherulitic structure of the different materials under polarized light in a hot stage. The pictures are taken during cooling at 0.33 K/s (20 K/min) at a certain temperature.

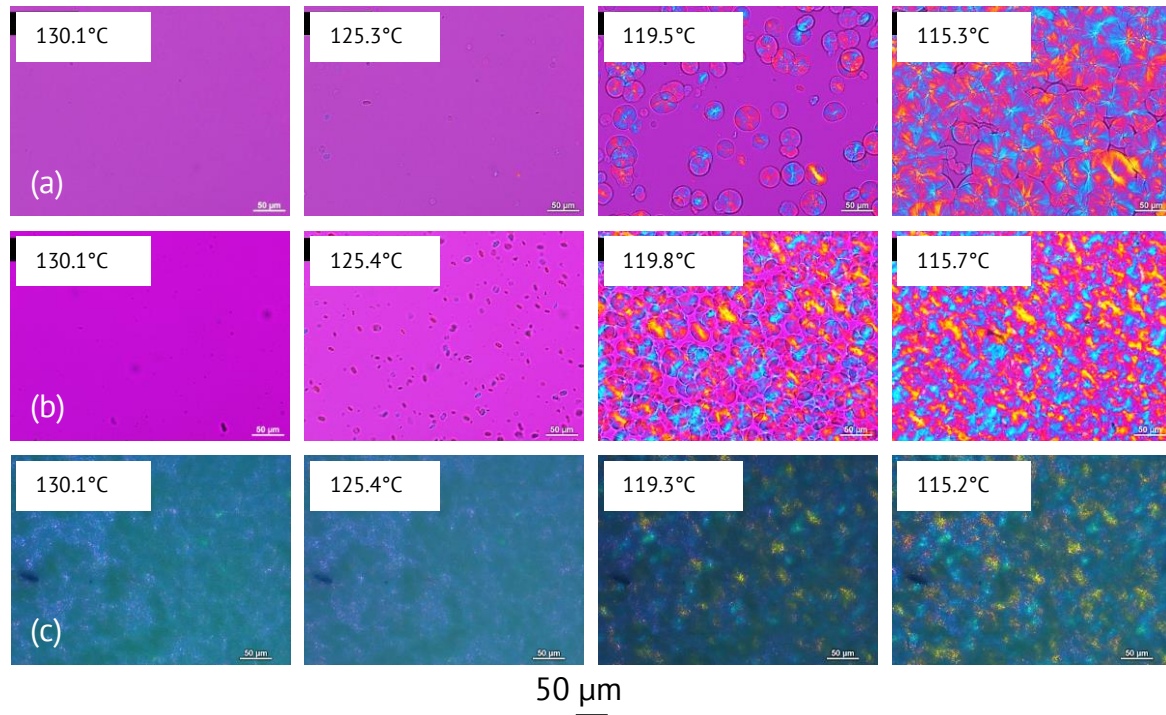


Figure 5.18: Solidification process of (a) PP-V0, (b) PP-S-V4, and (c) PP-T-V4 at a cooling rate of 0.33 K/s.

It can be seen that the first spherulites are visible at about 130°C just with the nanocomposites, whereas the neat PP is still fully molten. In addition, it can be recognized that a higher nanoparticle loading leads to a higher number of spherulites at the same temperature. At about 119°C, the growth of spherulites occurs in all the materials. However, the crystallization of the PP-S-V4 and PP-T-V4 is nearly finished; the higher the filler content the greater the area covered by spherulites taken at the same temperature. Therefore, it seems to be a matter of fact that the nanoparticles facilitate faster solidification, which is caused by the large increase of the heterogeneous nucleation density.

### Isothermal Spherulite Growth Rate

Figure 5.19 shows the plots of the relative isothermal spherulite growth rate, which is defined as the ratio of the growth rate of spherulite PP in the nanocomposite,  $G_{nPP}$  to the growth rate of neat PP,  $G_{PP}$ .

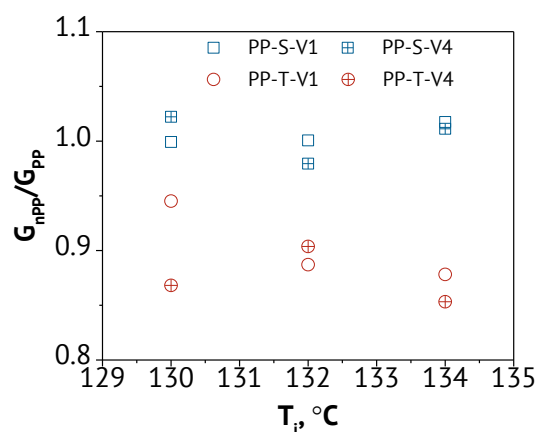


Figure 5.19: Spherulite growth rate of  $\text{SiO}_2$ - and  $\text{TiO}_2$ -filled PP.

The value of  $G_{nPP}/G_{PP}$  is almost 1 with the addition of  $\text{SiO}_2$ , indicating that  $\text{SiO}_2$  has no significant influence on the growth rate of PP. In other words, the growth rate of spherulite PP in  $\text{SiO}_2$ -PP is almost the same as in neat PP. However, the value of  $G_{nPP}/G_{PP}$  of  $\text{TiO}_2$ -filled PP is always lower than 1. This implies that the incorporation of  $\text{TiO}_2$  decreases the growth rate of spherulite PP. The result can be explained by the observation of the variation of the activation energy,  $\Delta E$  of different nanoparticles as described previously in the section 5.2.2. According to table 5.7, crystallization at low cooling rate (less than 1 K/s) occurs at 109-133°C. The  $\Delta E$  value of  $\text{SiO}_2$ -filled PP at this temperature range is so closed to neat PP. Therefore the  $\text{SiO}_2$  does not make any difference in the growth rate of spherulite PP. As for the  $\text{TiO}_2$  nanoparticles, the lower growth rate of PP is related to the larger  $\Delta E$  (about 2 times). This result verifies that  $\text{TiO}_2$  nanoparticles restrict the chain mobility of PP at a low cooling rate/high crystallization temperature.

The analysis of the spherulitic development of samples during slow cooling/low supercooling (high crystallization temperature) confirms that the presence of nanoparticle enhance the overall crystallization process of PP. This enhancement is caused by an increase of the nucleation density/rate, but not an increase of the spherulite growth rate.

### **5.3 Morphology of Injection Molded Samples**

#### **5.3.1 Skin-Core Morphology**

Figure 5.20 shows optical micrographs and a scheme of injection-molded samples of neat and nanoparticle-filled PP, which reveal a typical skin-core morphology. This morphology is typical classified into three [48] or four layers [93, 99-100]. In this work the injection molded plates were prepared by using a film gate. In this case four distinct morphological zones are clearly observed, i.e. a thin and highly oriented skin layer (1), a transition layer A (2), a transition layer B (3), and a spherulitic core layer (4).

The outer skin layer is formed when the molten polymer comes into contact with the cold cavity wall, and is quenched rapidly to solidify. The transition layer A (2) is formed directly on the skin layer. Because the skin layer is very thin, the transition layer is also cooled down rather rapidly and the quick solidification occurs. The molten polymer travelling just next to the solid layer is sheared and the molecules become oriented. The transition layer B (3) is formed when these oriented chains have crystallized. The molten polymer in the core (4) is only transported through the cavity with an essentially low level of orientation or no preferred orientation [99].

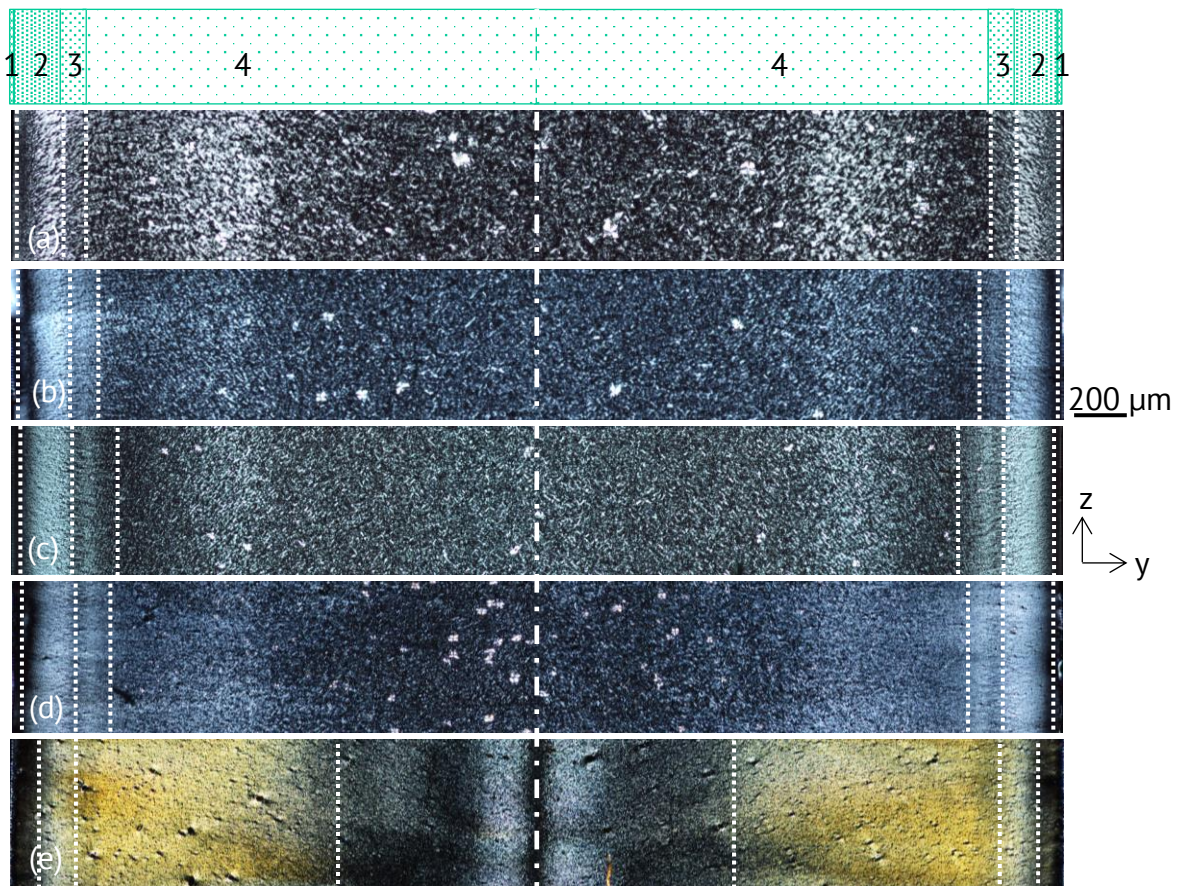


Figure 5.20: The skin-core morphology of injection-molded plates from polarized light microscope of thin section of (a) PP-V0, (b) PP-S-V1, (c) PP-S-V4, (d) PP-T-V1, and (e) PP-T-V4.

It is obvious that the addition of nanoparticles plays an important role in the morphology of the sample by changing the thickness of each layer. It is well known that the crystallization of semi-crystalline polymers is a so-called shear-induced crystallization, which is influenced by the thermo-mechanical history during the injection molding process. For instance, during the filling of a molten polymer into a cavity, the polymer is subjected to high shear stress at the cavity wall, which causes an orientation of the molecular chains and therefore of the supermolecular morphology. This so-called “oriented region” includes a very high and thin oriented skin layer (1), a transition layer A (2), and a transition layer B (3) [156]. Conversely, at the core (4) of the

sample, because of a relatively low cooling rate and low shear stress, the effect of shear on crystallization can be neglected. Therefore, the crystallization of the polymer is considered to take place three-dimensionally under a quiescent condition to form a spherulitic micro-structure with essentially no preferred orientation [48, 93, 96, 102]. Hence, the maximum of orientation occurs at the skin layer and decreases from the skin toward the core layer, with mild orientation or no preferential orientation in the core layer [48, 93, 102].

In order to quantitatively estimate the difference in morphology, the thickness of each layer was evaluated and is listed in table 5.8. The thickness was calculated by the ratio between the thickness of each layer and the thickness of half the injection-molded sample (from core to skin).

Table 5.8: Comparison of the normalized thickness of different layers of neat and nanoparticles-filled PP

<b>Normalized thickness, %</b>					
Layers	Materials				
	PP-V0	PP-S-V1	PP-S-V4	PP-T-V1	PP-T-V4
<b>Orientation</b>	<b>14.3 (±0.1)</b>	<b>15.2 (±0.1)</b>	<b>17.2 (±0.2)</b>	<b>18.0 (±0.1)</b>	<b>64.0 (±0.2)</b>
Skin	0.9 (±0.1)	1.1 (±0.1)	1.4 (±0.1)	1.6 (±0.2)	5.0 (±0.2)
·Transition A	9.0 (±0.2)	9.0 (±0.1)	9.6 (±0.2)	9.6 (±0.1)	6.7 (±0.2)
·Transition B	4.4 (±0.1)	5.1 (±0.2)	6.3 (±0.2)	6.8 (±0.1)	52.4 (±0.2)
<b>Core</b>	<b>85.7(±0.3)</b>	<b>84.8 (±0.1)</b>	<b>82.8 (±0.2)</b>	<b>82.0 (±0.3)</b>	<b>36.0 (±0.4)</b>

The results show that the thickness of the skin layer of the PP filled with both SiO<sub>2</sub> and TiO<sub>2</sub> nanoparticles slightly increased compared to neat PP. Moreover, the thickness of the skin layer increased with increasing nanoparticle loading. A similar observation can be made on the thickness of the transition B layer. However, the increase in the

thickness of the transition B layer of PP filled with TiO<sub>2</sub>-4 vol.% is much more pronounced. On the other hand, the thickness of the core layer of neat PP is higher than those of the PP filled with nanoparticles.

In general, the thickness of the core layer decreases while the thickness of the oriented layer increases with the incorporation of the nanoparticles. This is due to the higher thermal conductivity of PP when incorporating nanoparticles, as revealed also by Radhakrishnan et al. [108]. A higher thermal conductivity results in an enhanced cooling rate, causing a greater thickness of the skin layers of PP filled with SiO<sub>2</sub> composite compared to neat PP. As also described by Meister and Drummer [96], with an increasing cooling rate, the core layer has less time for relaxation and spherulite formation, leading to an increase of the skin layer. A similar observation was reported in the study of PP/clay nanocomposites [109]. In general, a higher cooling rate/lower melt temperature is accompanied by a higher melt viscosity, increasing the resulting orientation in the polymer [95].

### 5.3.2 Distribution of Spherulite Size

Figure 5.21 show the morphology of the different samples at higher magnification. It is important to remark that these micrographs were taken from only a half of the sample thickness, i.e. from the core to the skin. The photographs were taken at the spots marked in the scheme above. With the exception of the skin layer (figures 5.21, right), which is always featureless, the observed morphology is mostly spherulitic in all samples. Beside the main  $\alpha$ -phase spherulites, a small amount of  $\beta$ -phase (brighter spherulites) is observed, mostly in the core layer for all materials, except PP-T-V4. As it is seen in quiescent crystallization analysis (section 5.2), it is also worth noting that the mesophase can be formed somewhere near the skin layer due to the fast cooling [86].

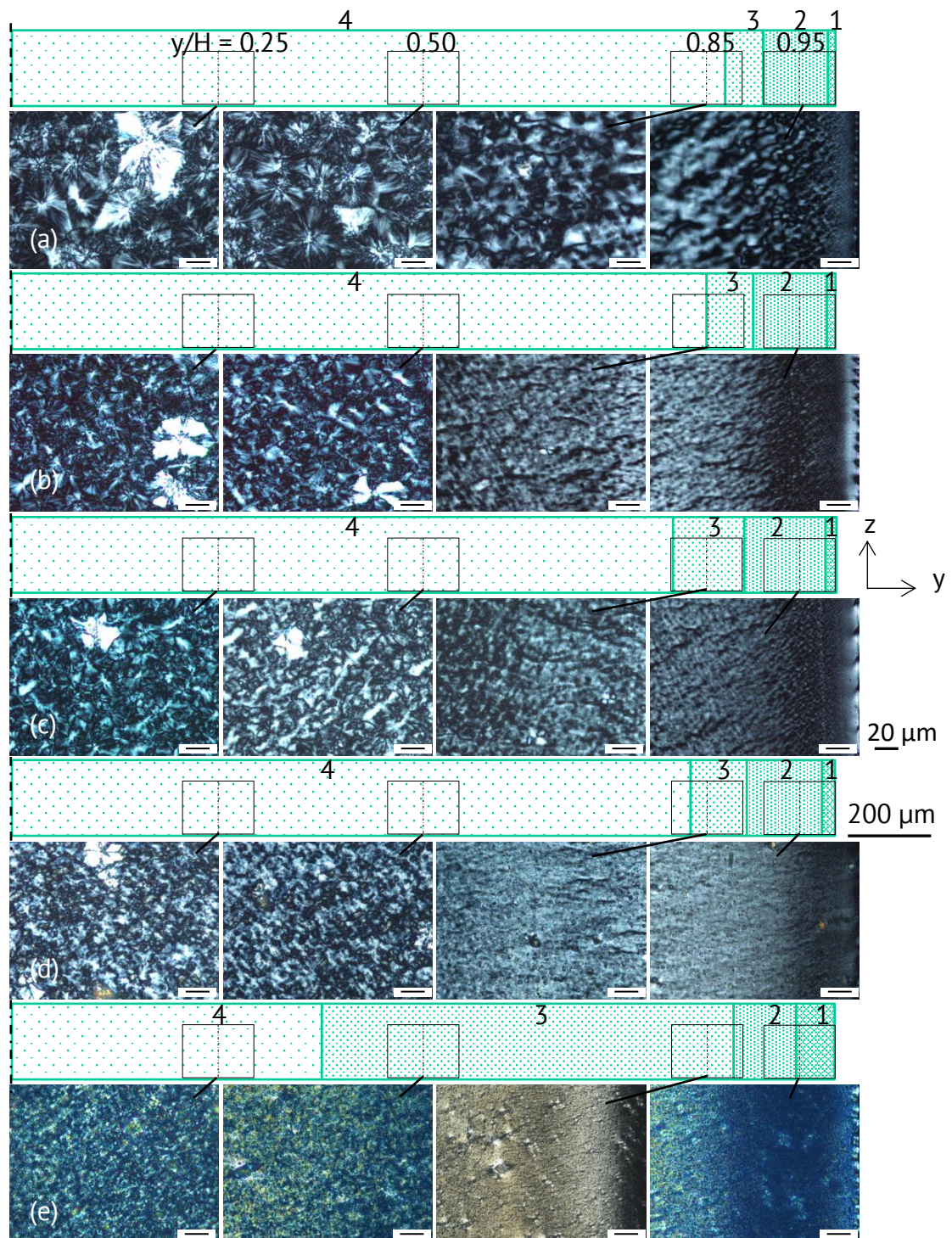


Figure 5.21: Polarized light micrographs of thin sections at various thickness ratio ( $y/H$ ) values of (a) PP-V0, (b) PP-S-V1, (c) PP-S-V4, (d) PP-T-V1 and (e) PP-T-V4. Scale bar of  $20 \mu\text{m}$  and  $200 \mu\text{m}$  are for the micrographs and the schematic of skin-core morphology.

Obviously, a fully developed spherulitic structure appears in the core layer (figures 5.21, left). Variation of the spherulite size in these samples can be clearly observed. There is a gradual decrease in the size of the spherulites from the core layer until they reach the non-spherulitic region somewhere near the skin layer. Large spherulites are found in the core layer, whereas tiny spherulites are formed near the skin layer. It can be seen that the addition of nanoparticles led to a reduction of spherulite size. However, in the case of the addition of 4 vol.% TiO<sub>2</sub> nanoparticles, the spherulitic structure diminished in all layers. This observation is confirmed by optical micrographs of etched samples by using reflecting light as illustrated in figures 5.22.

The spherulitic structure of PP can be clearly seen due to different topographies after chemical etching. The etching solution preferentially attacks the amorphous regions, leaving the crystalline lamellae essentially intact [128-129, 157]. Using the same definition of the distance from the skin as previously described in the thin section sample, the locations of interest were the same, except at  $y/H = 0.95$ . This was because of an artificial morphology at the edge of the sample via etching solution. As expected, the spherulite size decreased with decreasing distance from the core to the skin layer in all samples (figures 5.22) as already observed in the non-etched thin section images. However, the difference in spherulite size is hardly to see for PP filled with TiO<sub>2</sub>-4 vol.%.

At the core layer, a homogeneous polyhedral spherulitic structure with sharp boundaries can clearly be seen in all the samples. However, the spherulitic morphology of the skin layer is distinctly different from the core layer. As discussed above, the molten polymer is subjected to high shear stress at the cavity wall, causing the preferential orientation of the molecular chains during processing [48, 93].

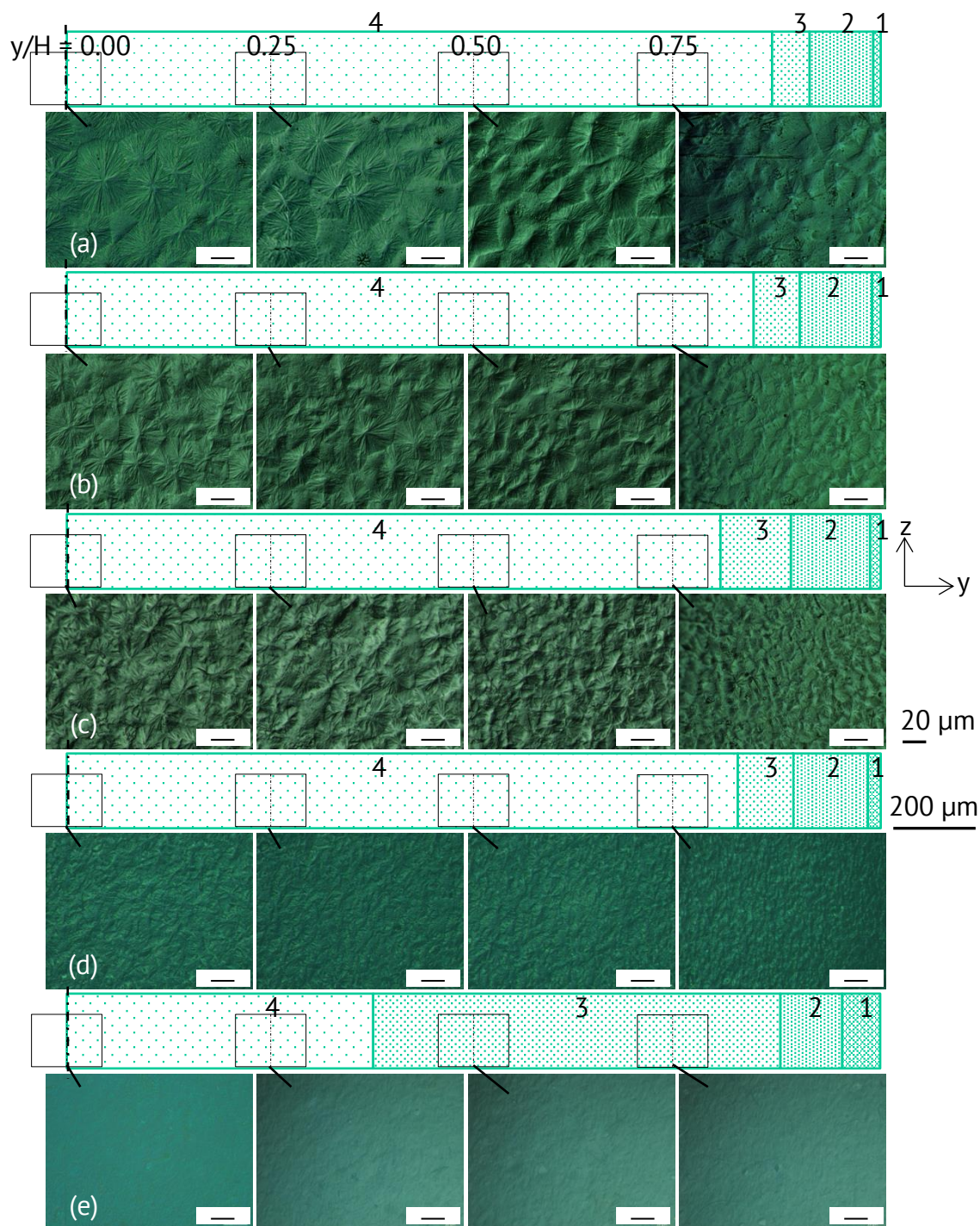


Figure 5.22: Micrographs of etched samples at various thickness ratio ( $y/H$ ) values from the core ( $y/H = 0$ ) to the skin ( $y/H = 1$ ) of (a) PP-V0, (b) PP-S-V1, (c) PP-S-V4, (d) PP-T-V1 and (e) PP-T-V4. Scale bar of 20  $\mu\text{m}$  and 200  $\mu\text{m}$  are for the micrographs and the schematic of skin-core morphology.

For qualitative analysis, the spherulite size was measured according to the ASTM E112-10 standard for grain size determination [158]. The average spherulite size obtained from the thin section images and the etched sample images are illustrated in figure 5.23 (a) and 5.23 (b), respectively.

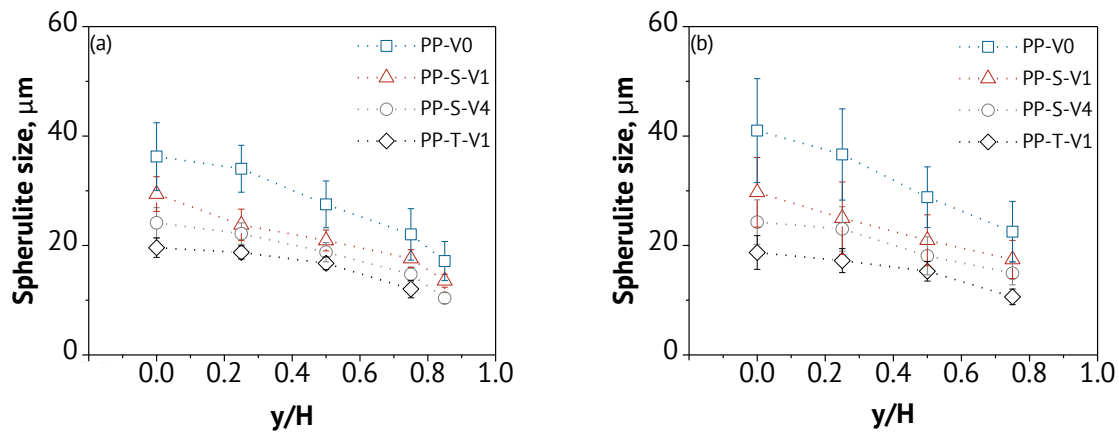


Figure 5.23: Variation of spherulite size with different  $y/H$  values as function of nanoparticle loading obtained from (a) thin sections, and (b) etched samples.

In all cases, the biggest spherulites are found in the core layer and they become smaller from the core to the skin layer [93, 106]. This could be a result of both a different nucleation rate and a different spherulite growth rate, which are controlled by the level of the cooling rate and shear rate in each layer. Equally important, with the incorporation of nanoparticles a higher  $\text{SiO}_2$  nanoparticles loading results in a smaller spherulite size. A great decrease in spherulite size is found with the addition of 1 vol%  $\text{TiO}_2$ . In this case the smallest spherulite size is observed compared with the other materials at the same position. There is very good agreement between the average spherulite sizes measured from the thin sections and etched samples. This indicates that the nanoparticles act as a nucleating agent, where a higher number of nuclei lead to smaller spherulites [159-160]. This can be confirmed by analysis of crystallization behavior and spherulitic development at different supercooling in section 5.2,

suggesting that the faster crystallization process is due to increased heterogeneous nucleation density/nucleation rate but not due to increased spherulite growth rate. A nanoparticle surface reduces frequently the nucleus size (lower free enthalpy barrier) needed for crystal growth. However, the nucleating effect of TiO<sub>2</sub> nanoparticles is more pronounced than SiO<sub>2</sub> nanoparticles.

### 5.3.3 Distribution of Lamellar Morphology

Figure 5.24 shows the lamellar organization in the PP spherulites. The essential appearance and features of the so-called “cross-hatched” morphology for neat PP are revealed. This unique cross-hatched lamellar arrangement is a characteristic of the  $\alpha$ -phase [161].

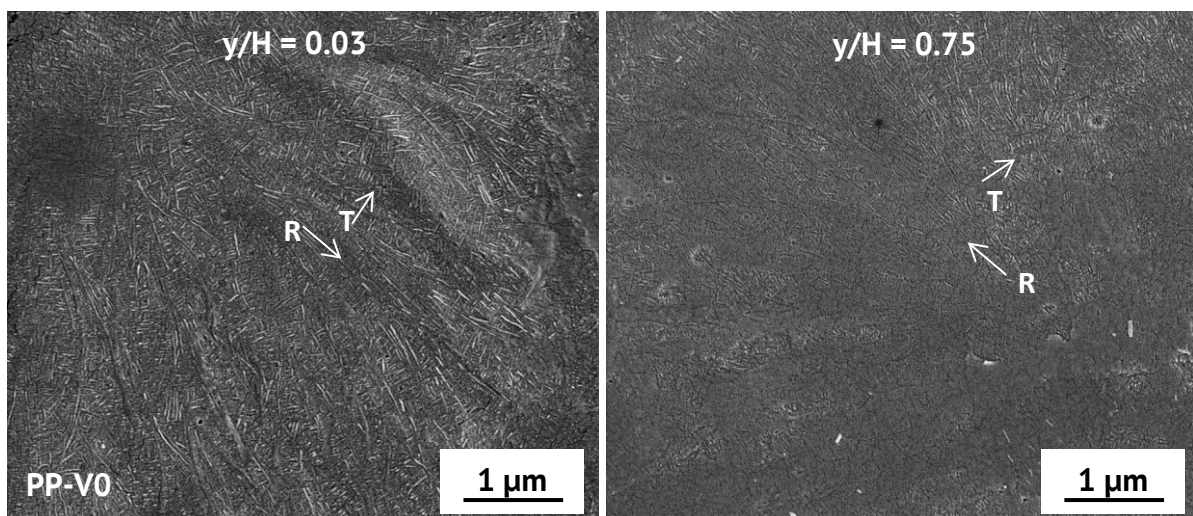


Figure 5.24: The general appearance of the cross-hatched structure in neat PP at two different  $y/H$  values.

In the figure the direction R represents the radial direction within the spherulite whereas the direction T represents the branched, tangential direction. A characteristic of the cross-hatched overgrowth is that the shorter tangential lamellae growing epitaxially on the plane of the radial lamellae. The intercrossing tangential lamellae

are set at angles of approximately  $80^\circ$  with respect to the radial direction. The same feature can be observed in the incorporation of  $\text{SiO}_2$  nanoparticles (figure 5.25), and  $\text{TiO}_2$  nanoparticles (figure 5.26).

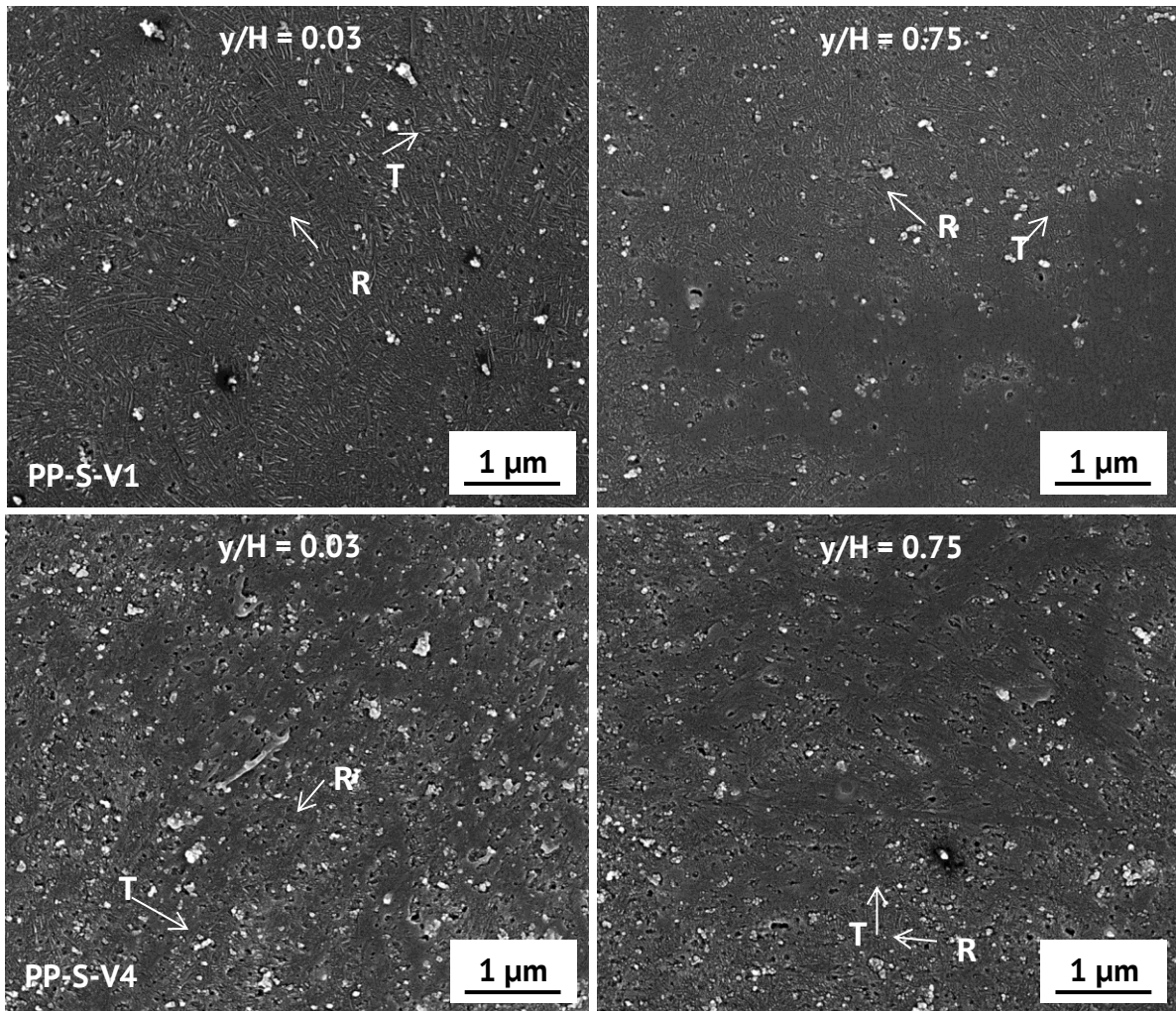


Figure 5.25: The general appearance of the cross-hatched structure in  $\text{SiO}_2$ -filled PP at two different  $y/H$  values.

The distribution of crystalline lamellae thickness through the thickness direction can be observed in Figure 5.24. The thickness of crystalline lamellae is seemingly smaller in the skin region than in the core region in all materials. The high crystallization temperature or low supercooling,  $T$  in the core region leads to a lamellar thickening. This is because of the relatively low cooling rate in the core, resulting in more time for

lamellar thickening. On the other hand, because of the high cooling rate experienced in the skin region, the lamellar thickening proceeds in a very short time at low crystallization temperature or high supercooling, therefore the thickness of the lamellae will be decreased. Thus, it can be understood that the increase of lamellar thickness depends on the distance from the skin to the core. Regarding the influence of nanoparticles, it is hard to see in figure 5.25 and 5.26 and has to be proven by other methods such as X-ray diffraction.

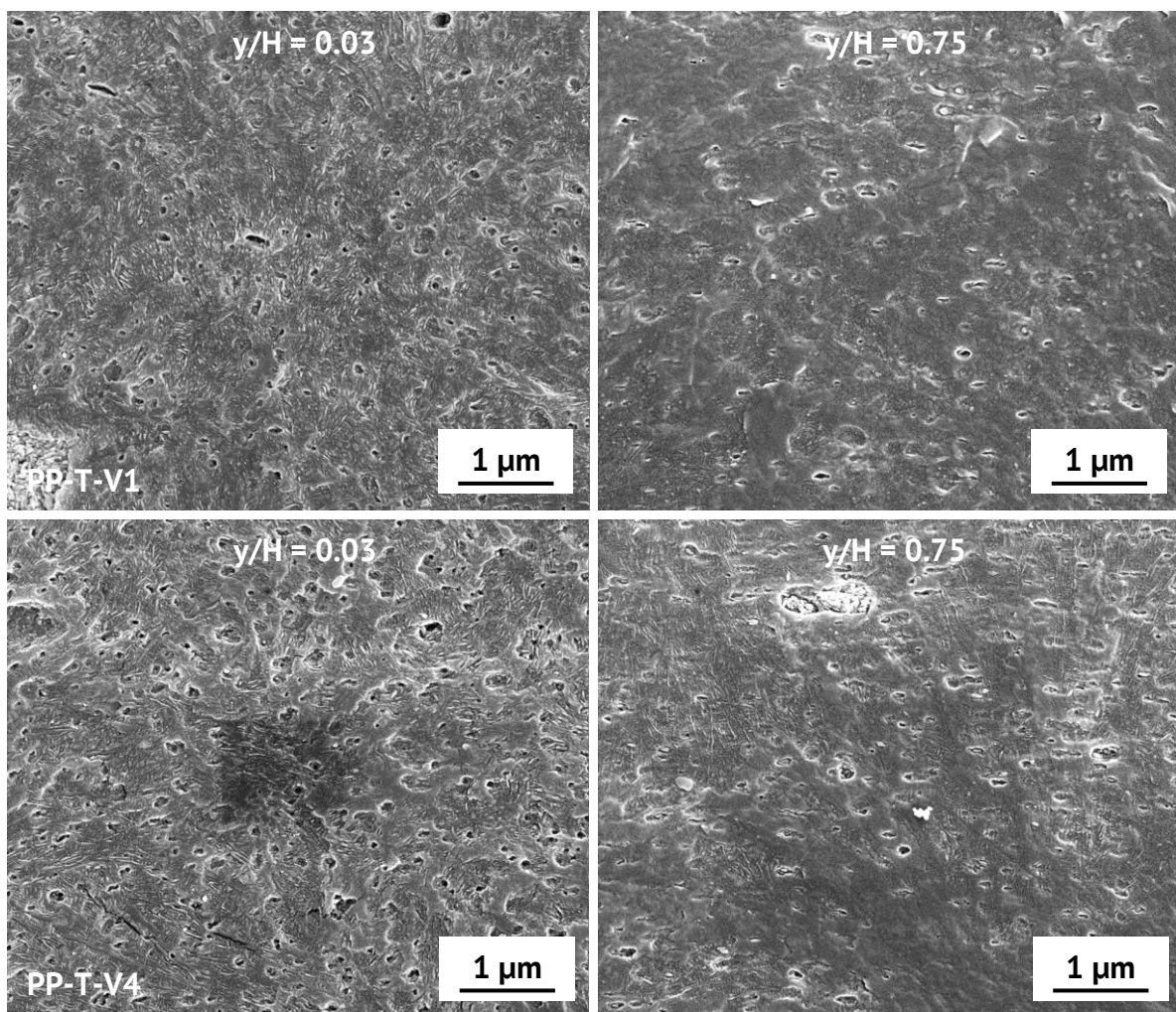


Figure 5.26: The general appearance of the cross-hatched structure in  $\text{TiO}_2$ -filled PP at two different  $y/H$  values.

### 5.3.4 Distribution of Nanoparticles

Figure 5.27 represents the high-resolution SEM of an ion-polished sample where the nanoparticles were uniformly distributed and homogeneously dispersed in the PP matrix.

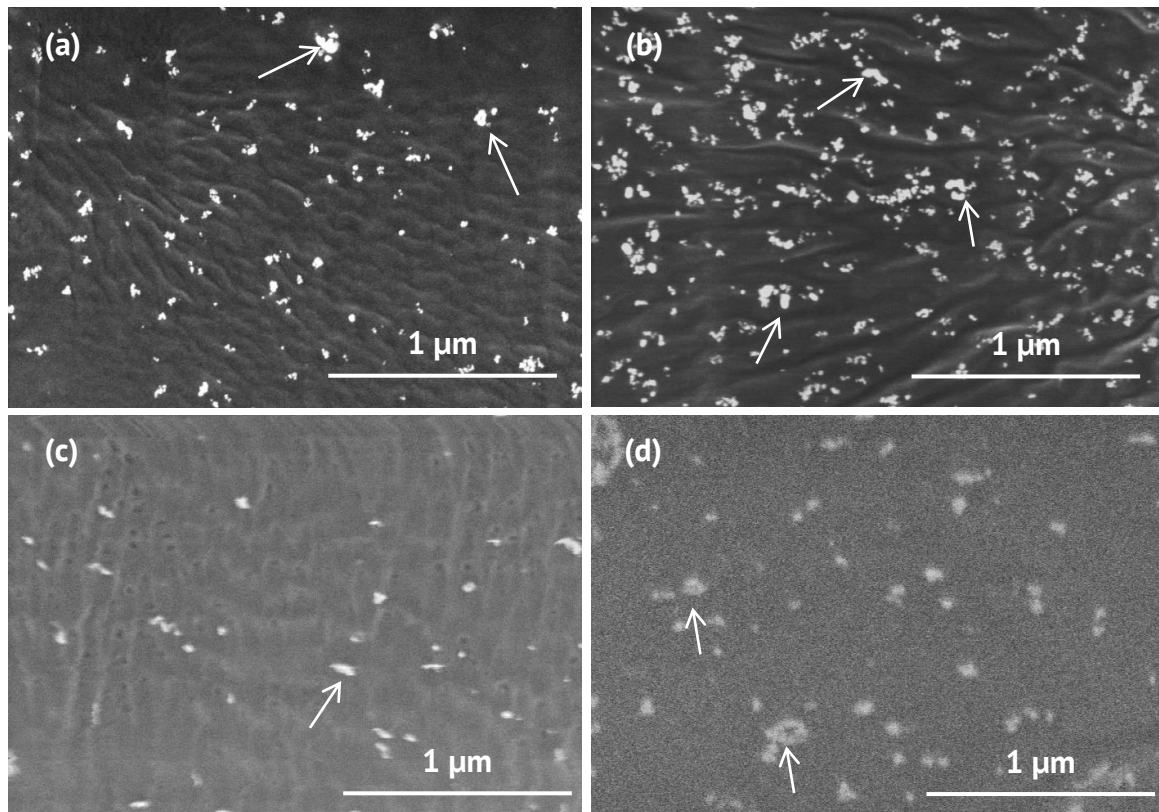


Figure 5.27: SEM images of an ion-polished sample of (a) PP-S-V1, (b) PP-S-V4, (c) PP-T-V1, and (d) PP-T-V4.

The pictures are taken at the core region. These SEM images reveal agglomerates in the size range of 30–100 nm. However, more agglomerates are found for a high nanoparticle loading, i.e. PP-S-V4 and PP-T-V4. This is reasonable considering that at high nanoparticle loadings, the interparticle distance is small, and hence the nanoparticles trend to form agglomerates.

The SEM micrographs of fractured surfaces shown in figure 5.28 also confirm the homogeneous distribution of nanoparticles. This finding signified a good deagglomeration that seemingly originated from the processing of nanocomposites used in this work. In addition, the nanoparticles seem to be floated at fracture surface and no signs of interaction with the matrix are observed. This poor adhesion between the nanoparticle and PP matrix is responsible for the low mechanical properties measured in section 5.4.1.

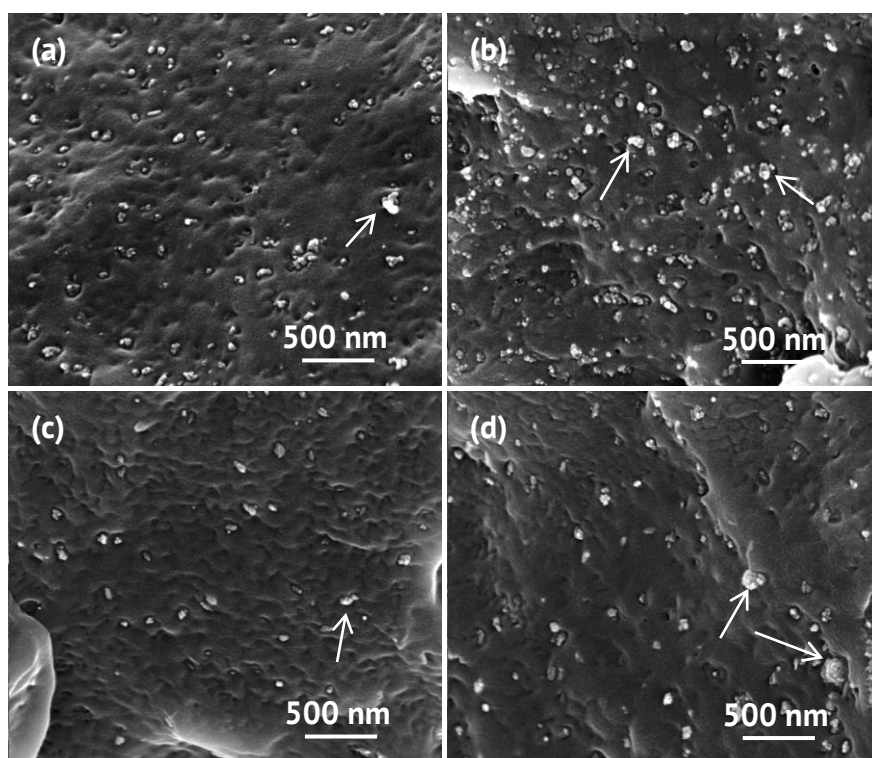


Figure 5.28: High resolution SEM images of fractured surfaces of (a) PP-S-V1, (b) PP-S-V4, (c) PP-T-V1, and (d) PP-T-V4.

Figure 5.29 shows the binary images of ion-polished SEM micrographs analyzed by MATLAB image processing software. These binary images reveal the distribution of nanoparticles along the thickness direction of samples.

The fraction of  $\text{SiO}_2$  nanoparticles shown in figure 5.30 was determined by the area covered by  $\text{SiO}_2$  nanoparticles, as white spots. A greater value of the  $\text{SiO}_2$  fraction is

found in the core region and it becomes smaller from the core to the skin region. Moreover, at the same  $y/H$  the value of the  $\text{SiO}_2$  fraction of PP-S-V4 is almost four times greater than that of PP-S-V1. Moreover, the agglomerated  $\text{SiO}_2$  nanoparticles seem to decrease with decreasing distance from the core to the skin region. The smaller size of the  $\text{SiO}_2$  nanoparticle agglomerates in the skin region is due to the intense shear field.

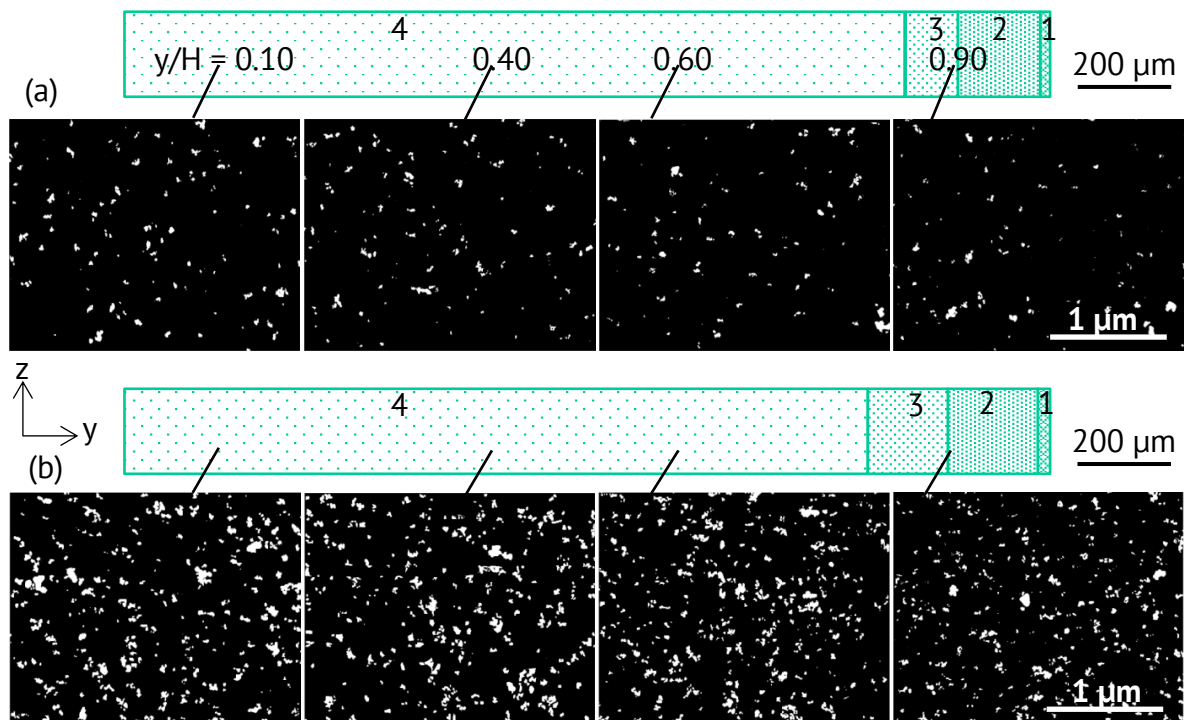


Figure 5.29: Binary images of ion-polished SEM micrographs of (a) PP-S-V1 and (b) PP-S-V4.

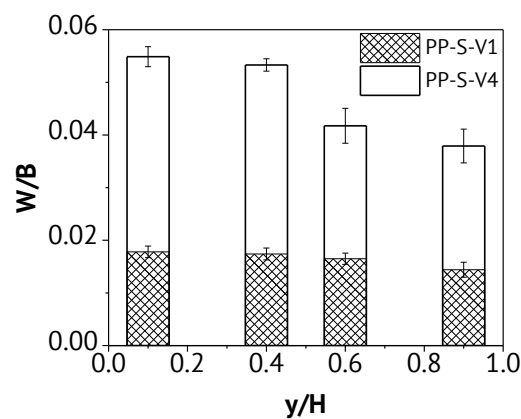


Figure 5.30: The  $\text{SiO}_2$  fraction ( $W/B$ ) as a function of  $y/H$  value.

As shown in figure 5.21 and 5.22 from optical micrographs, the reduction in the size of spherulite is thus considered to be a result of two contributions: the processing effect, in which high shear and cooling result in smaller spherulite; and the nucleation effect of nanoparticles in which high loading of nanoparticles produce a decrease in spherulite size. Even if a higher amount of SiO<sub>2</sub> nanoparticles is found in the core region, a greater spherulite is observed. This implies that processing histories produce a more pronounced effect than the nucleation effect of nanoparticles in this regard.

### 5.3.5 Distribution of the Nanoparticle Orientation

Figure 5.31 shows the SEM images of TiO<sub>2</sub> orientation along the thickness direction of an injection-molded part. Apparently, the TiO<sub>2</sub> nanoparticles in the injection-molded part are aligned irregularly in the PP matrix.

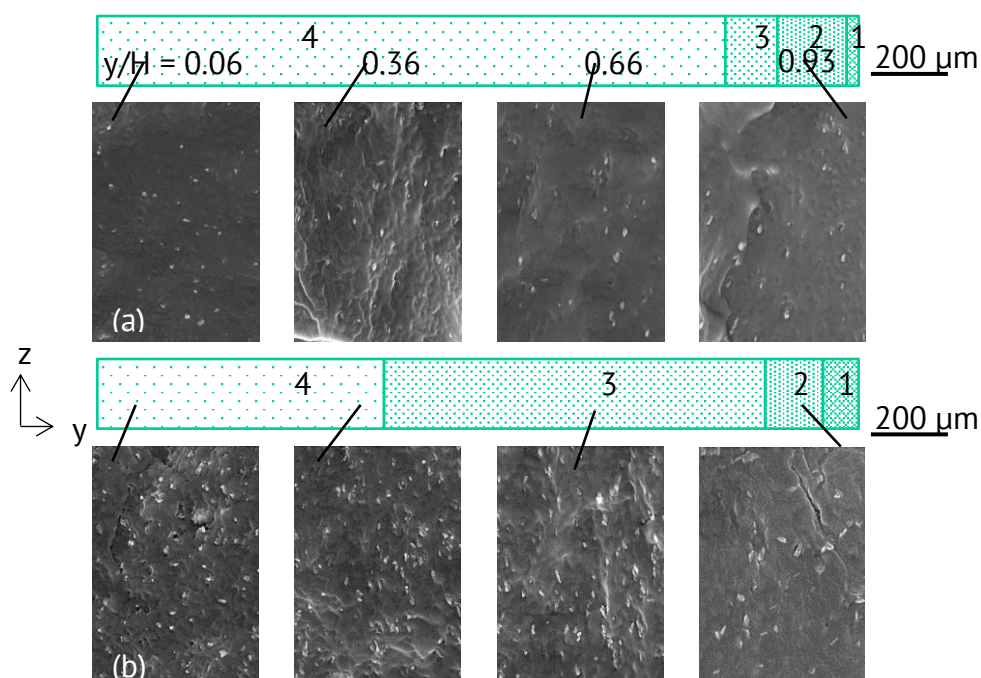


Figure 5.31: High resolution SEM micrographs of the cryofracture samples along thickness of injection molded part of (a) PP-T-V1 and (b) PP-T-V4.

Based on the high resolution SEM images of the cryofracture surface, the orientation of needle-shaped  $\text{TiO}_2$  nanoparticle along the thickness of injection molded part can be determined. The y-orientation is defined as the orientation of nanoparticles whose long axes are between  $-45^\circ$  and  $45^\circ$  in the yz-plane. The other orientation of nanoparticle (between  $-45^\circ$  and  $-90^\circ$  or  $45^\circ$  and  $90^\circ$ ) is described as z-orientation. Figure 5.32 resents the result of the  $\text{TiO}_2$  nanoparticle orientation in PP-T-V1 and PP-T-V4.

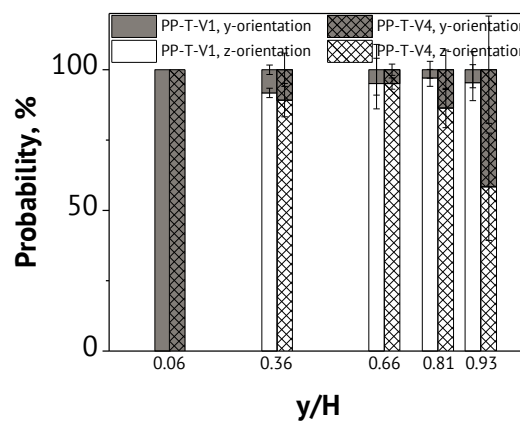


Figure 5.32: Orientation of  $\text{TiO}_2$  nanoparticles along thickness of injection molded part of PP-T-V1 and PP-T-V4.

It is clearly observed that the flow is a key in the orientation of needle-shaped  $\text{TiO}_2$  nanoparticle along thickness of injection molded part. The layer near the cavity wall ( $y/H = 0.93$ ) tends to have  $\text{TiO}_2$  nanoparticles randomly oriented or slightly aligned with the flow (z-orientation) [163], in particular at high  $\text{TiO}_2$  loading. The orientation in this layer may be influenced by a competition of fast cooling and shear flow. Furthermore, the  $\text{TiO}_2$  nanoparticles are mostly aligned in the flow direction (z-orientation) somewhere near the transition B layer ( $y/H = 0.66$ ), and this string alignment is large close to the core. At the core, the  $\text{TiO}_2$  nanoparticles exhibit a random orientation ( $y/H = 0.06$ ) due to the low shear force in the core. This is a somewhat expected result. However, this irregular orientation of  $\text{TiO}_2$  nanoparticles is more pronounced in the

higher TiO<sub>2</sub> loading sample. In filler-reinforced polymer, the mechanical properties of products can be influenced by the orientation of the fillers such as fibers, needle-shape or rod-shape particles, which is governed by the flow during the filling stage. This flow-induced filler orientation can vary significantly across the thickness of the injection-molded parts [162].

### 5.3.6 Distribution of Crystallinity

The crystallinity distribution throughout the thickness of the samples as obtained from DSC analysis is presented in figure 5.33.

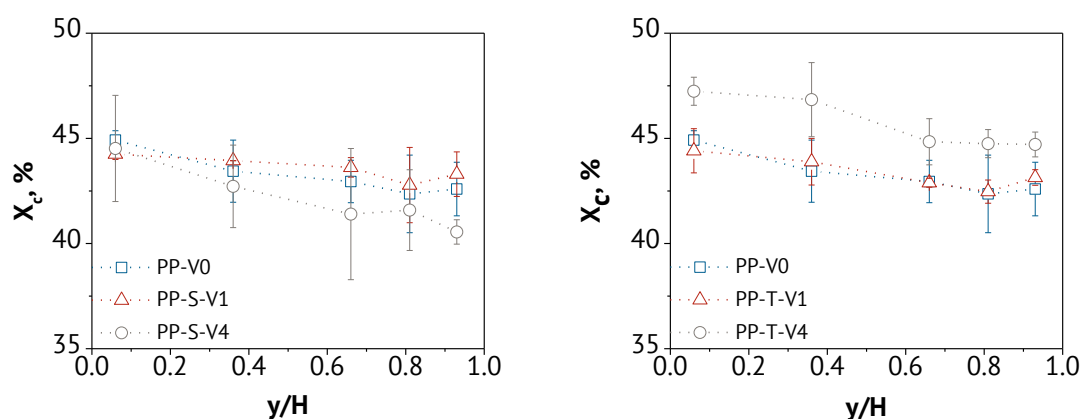


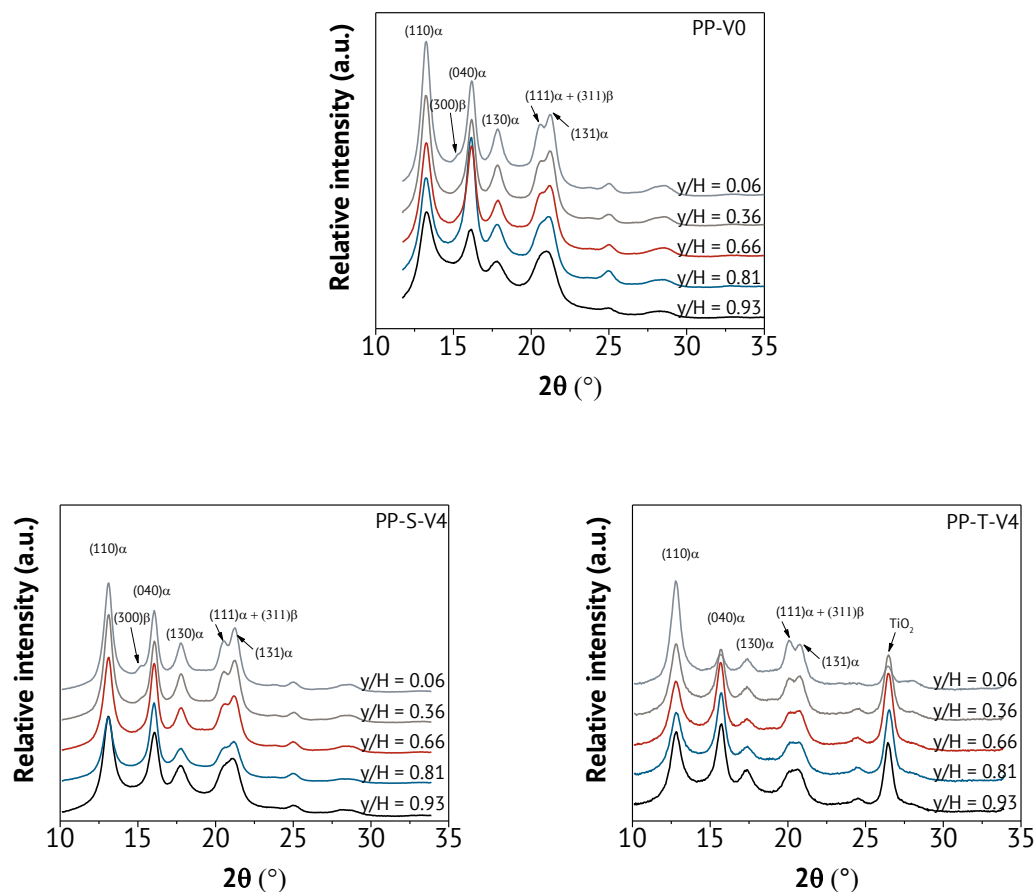
Figure 5.33: Degree of crystallinity distribution along thickness for neat PP and PP filled with nanoparticles.

It was reported that the degree of crystallinity decreased from the core to the skin layer [96]. This phenomenon is also basically observed in this work. It can be seen that a higher degree of crystallinity is found in the core layer for all materials. Due to the low cooling rate and long relaxation, the molecular chains have more time for crystallinity to develop. Furthermore, on average a slight decrease in the degree of crystallinity is found with increasing SiO<sub>2</sub> loading. This could be due to the limitation of the chain

mobility, which has been described in the case of PP filled with core-shell silica hybrid particles [36]. On the contrary, an increased degree of crystallinity is observed with increasing  $\text{TiO}_2$  loading. This is due to the heterogeneous nucleation of the  $\text{TiO}_2$  nanoparticles.

### 5.3.7 Distribution of Spherulite Form

Figure 5.34 shows the distribution of 1D WAXD patterns along the thickness of injection- molded parts.



5.34: WAXD profiles of neat and nanoparticle-filled PP.

It can be seen that the WAXD patterns of both neat and nanoparticle-filled PP present a mainly  $\alpha$ -phase, as the major reflections emerged at  $2\theta = 13.2, 16.1, 17.8, 20.5$  and  $21.2^\circ$ .

In fact, at  $2 = 15.9^\circ$ , the reflection represents the characteristics of  $\beta$ -iPP. However, the  $\beta$ -phase has another reflection at  $2 = 21.0^\circ$ . This peak is overlapped with the reflection of  $\alpha$ -phase at  $2 = 21.0^\circ$  [164, 165]. An additional weak reflection of the  $\beta$ -phase ( $2 = 15.9^\circ$ ) also appears. This reflection is found only in the core layer for all materials except PP-T-V4. This result is parallel to that observed from the microscopy analysis in section 5.3.2.

It was reported that the  $\beta$ -phase was suppressed by the intense shear field in the skin layer [166]. It is a matter of fact that the nucleation rate of  $\beta$ -phase is lower, while the growth rate is higher compared to  $\alpha$ -phase [17]. This can be a reason for the absence of  $\beta$ -phase in the skin layer. A higher cooling rates and intense shear field in the skin layer, the  $\beta$ -phase has insufficient time to form nuclei. In contrast, the appearance of  $\beta$ -phase in the core layer can be ascribed to a combination of the local lower cooling rates and shear rates. More  $\alpha$ -nuclei are induced by the intense shear force and by the heterogeneous nucleation of the nanoparticles.

### 5.3.8 Distribution of Lamellar Thickness

Figure 5.35 plots the scattering data in the form of the Lorenz-corrected SAXS intensity,  $Iq^2$ , versus the scattering vector,  $q$ . The results also show that the position of the scattering peak shifts to a higher  $q$  value with increase of  $y/H$  value.

The neat PP sample shows obvious reflection, which is assigned to the long period corresponding to the sum of thickness of a crystalline component and an amorphous component in the spherulite. The calculated results of the long period and crystalline lamellar thickness are plotted in figure 5.36. The crystalline lamellar thickness increases from the skin to the core. In the nanoparticle-filled PP, the intensities of the reflection tend to become weaker and finally disappear. This may be indicative of the detrimental role of the nanoparticles (i.e.  $\text{SiO}_2$  and  $\text{TiO}_2$ ) on the regular ordering at a

lamellar level and reflects an analogous effect brought about by lamellar nanoparticles [167].

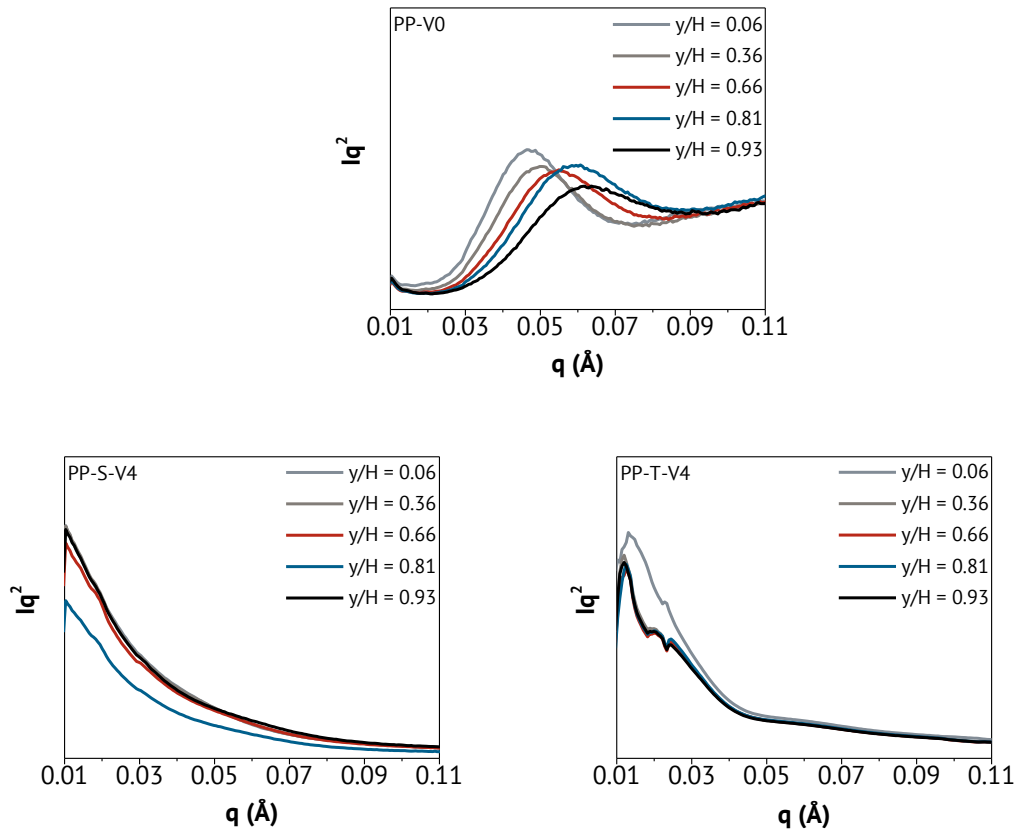


Figure 5.35: Plots of Lorenz-corrected SAXS intensity  $Iq^2$  vs  $q$  of neat and nanoparticle-filled PP.

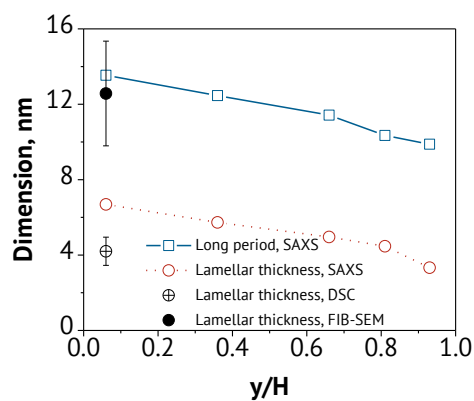


Figure 5.36: Long period and lamellar thickness as a function of  $y/H$  value for neat PP

In addition to SAXS data, the lamellar thickness can be obtained by DSC melting endotherms based on the Gibbs-Thomson equation according to equation (17) and revealed by SEM images measured from figure 5.24. The comparison of lamellar thickness obtained from three different methods was made at the core region of the PP-V0 sample. As it can be seen, the average value of lamellar thickness depends on the method of investigation. With the use of DSC for the determination of the lamellar thickness, the sample is subject to annealing during the DSC experiment [168]. Thus, the determined melting curves may not truly represent the original sample. In addition, the different heating rate used in the DSC experiment can change the width and the position of melting curves. Not to mention the parameters,  $T_m^\circ$  and  $\sigma_e$ , used in the Gibbs-Thomson equation. The use of different values of both parameters results in a large difference in the calculated lamellar thickness [168].

There are three major problems associated with the SEM approach. First, it is assumed that the morphology of the sample is not changed in the sample preparation process, i.e. chemical etching process, which is uncertain in many cases. Second, the contrast of SEM images is always not uniform. This implies that the crystalline lamellae are in different orientation states with respect to the etched surface, thus the obtained lamellar thickness value may not be accurate. Finally, the obtained SEM images are only a small fraction of a bulk sample. Therefore, it may not be complete and precise representative of the real material [168].

## 5.4 Deformation Behavior

### 5.4.1 Tensile Properties

#### Tensile Strength

The tensile strength of a thin section is defined as the maximum stress that the thin section can sustain under uniaxial tensile loading. Figure 5.37 presents the dependence of the tensile strength of thin sections on the thickness ratio,  $y/H$ . It is worth noting that there is no normal or shear stresses in the direction perpendicular to the thin section surface. Therefore, thin section exhibits a plane stress state and therefore the behavior of bulk sample (three-dimensional stress state) might be different.

It can be seen that neat PP exhibits an increasing tendency of tensile strength as the  $y/H$  decreases. The reason for the increase in the tensile strength from the skin to the core is related to the morphology formation during injection molding as described in section 5.3. The mechanical properties of semi-crystalline polymer are strongly dependent of their crystallinity, spherulite size and lamellar thickness, which depend on the processing conditions. As a lower cooling and shear rate, higher crystallinity at the core results in a higher tensile strength [169]. It is well known that it is the crystalline rather than the amorphous components that are strong and more difficult deformed. In addition, the larger the spherulite sizes the higher are the tensile strength [2, 169]. In the absence of a foreign substance, in general, an increase in the degree of crystallinity from the skin to the core is usually accompanied by an increased spherulite size and lamellae thickness [122]. In this case, It is interesting, but rather difficult, to separate the respective effects of the main morphological parameters, such as degree of crystallinity, spherulite size and lamellae thickness.

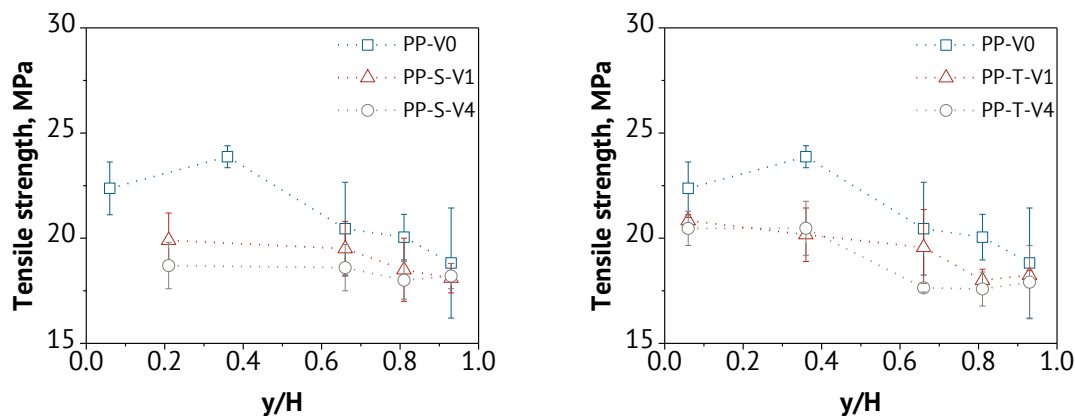


Figure 5.37: Tensile strength of neat and nanoparticle-filled PP.

For nanoparticle-filled PP, tensile strength relies on the effectiveness of stress transfer between polymer matrix and nanoparticles. The same tendency as neat PP is observed in both SiO<sub>2</sub>- and TiO<sub>2</sub>-filled PP samples, the tensile strength increases as the  $y/H$  decreases. However, at the same  $y/H$  value, a reduction in the tensile strength is observed with the incorporation of nanoparticles. The higher nanoparticle loading gives a lower tensile strength. This reduction in tensile properties of nanoparticle-filled PP could be associated with a poor interfacial adhesion between the nanoparticle and PP matrix. This can be confirmed by high resolution SEM images of cryofracture surface in section 5.3.4 and 5.3.5. Because there is not sufficient interfacial adhesion between the nanoparticle and PP, interfacial debonding takes place. This induces the generation of stress concentration at the nanoparticle/PP interface [170]. Therefore, the applied stress cannot be properly transferred from the matrix into nanoparticles, resulting in a drop in tensile properties.

Moreover, by increasing the amount of nanoparticles, larger agglomerates of nanoparticles can be formed as shown in figures 5.27 and 5.28. This indicates that the tensile strength decreases with decreasing surface area of the higher particle loading (larger agglomerates) through a less efficient stress transfer mechanism [27, 170]. In

addition, due to the fact that thin sections can present cutting defects, which cause the breakage of the agglomerates. In consequence, it makes easier to crack initiation.

In addition to the enhancement of the flow-induced morphology, the nucleation ability of nanoparticles is concerned in the case of nanoparticle-filled PP. Optical microscopy analysis reveals the reduction in the size of spherulites with the incorporation of nanoparticles. Small spherulites generally cause a lower tensile strength [2, 169]. Although, the tensile strength increases with the degree of crystallinity in neat PP, the enhancement of the degree of crystallinity in PP-T-V4 is not effective to increase the tensile strength.

From the above discussion, the tensile strength of nanoparticle-filled PP is determined not only by nanoparticle/matrix interfacial adhesion and nanoparticle loading, but also the main morphological parameters, such as degree of crystallinity and spherulite size, not to mention spherulite form. The interplay between these factors cannot always be separated.

### **Elongation at Break**

The elongation at break of materials is shown in Figure 5.35. The rupture behavior was observed only for PP-S-V4, PP-T-V1 and PP-T-V4 due to the limitation of the instrument. On the other hand, no observation of rupture behavior of neat PP indicates the much higher elongation at break compared to the nanoparticle-filled PP.

For PP-S-V4, it can be seen that the elongation at break seems to increase as the  $y/H$  values increases, but the large standard deviation should be noted. The addition of the  $\text{TiO}_2$  nanoparticles also shows an increasing tendency of the elongation at break from the core to the skin. With increasing  $\text{TiO}_2$  loading, the elongation at break decreases. These results are consistent with the concept that the spherulite size plays an

important role in determining ultimate elongation. A decrease in the spherulite size results in an increase in the ultimate elongation [2]. In contrast, the larger the spherulite size the fewer are the interspherulitic links, resulting in a more brittle behavior. However, the faster cooling rate and the higher shear rate at the skin layer required for the greater nucleation rate/higher number of nuclei to give small spherulites also result in a coarse and poorly formed spherulitic structure which does not give the best mechanical properties [117].

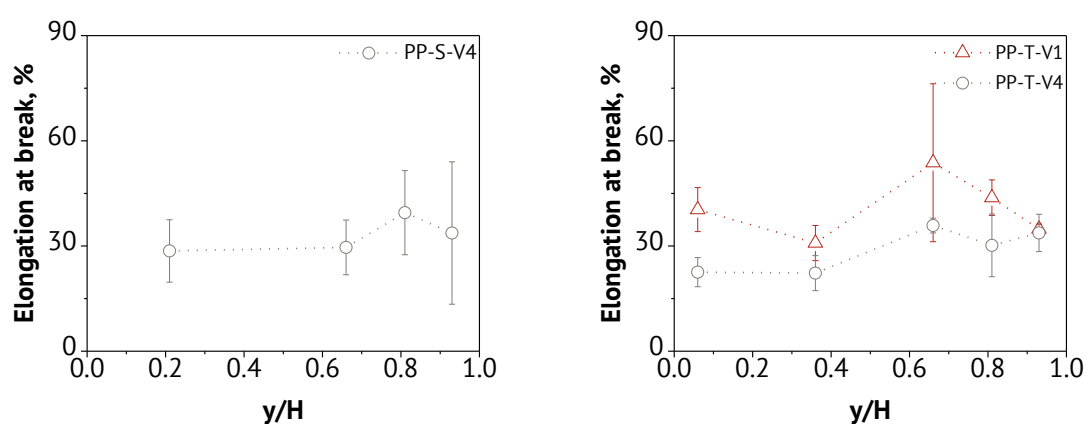


Figure 5.38 Elongation at break of SiO<sub>2</sub> and TiO<sub>2</sub>-filled PP.

One can compare the elongation at break of PP-S-V4 to PP-T-V4 in figure 5.38. With the addition of SiO<sub>2</sub>, the elongation at break seems to be higher than the addition of TiO<sub>2</sub>. Furthermore, at 1 vol.% of nanoparticle, the rupture behavior can be seen in PP-T-V1, but no observation of the rupture behavior in PP-S-V1. This implies that PP-S-V1 might give a higher the elongation at break than PP-T-V1.

In general, the higher tensile strength and lower failure elongation are indications that the fibers are preferentially oriented in the flow direction. The significantly lower elongation at break of the alignment direction compared to the transverse direction is due to the strain limit of the fibers. This low capacity of the fibers in straining results in a low ductility of the composite [171]. In this work, the opposite results are observed.

The tensile strength and elongation at break are more dominated by the matrix morphology and/or interfacial property.

## 5.4.2 Spherulitic Deformation

### Neat Polypropylene

During micro-tensile tests different deformation develop from the skin to the core region. Figure 5.39 shows the deformation of neat PP for xy-plane samples when these thin sections were drawn at different elongations. The deformation of semi-crystalline polymers is usually considered in terms of a spherulitic structure. When the elongation is about 3%, spherulitic deformation is not detected under the optical microscope in all  $y/H$  values. However, it is reported that the initial deformation is considered to occur via deformation of the interlamellar amorphous component, which are the tie molecules [112, 116]. As the elongation increases to 20% (slightly beyond the yield stage), at somewhere in the core region ( $y/H = 0.06, 0.36$  and  $0.66$ ), cracks are formed preferentially through the spherulite centers and the spherulites boundaries which are perpendicular to the tensile direction. The inhomogeneity of spherulite deformation is due to a variation of local stress concentration within the spherulites. The high stress concentration in the center and the boundaries of the spherulite is responsible for the premature of spherulite deformation [117, 119]. These two deformation areas (i.e. spherulite center and boundaries) appear to be the weak points in the spherulites and have been previously noted in several semi-crystalline polymers [112, 114, 172]. With further stretching at an elongation of 40%, more cracks form and existing cracks are widened.

In contrast, near the skin ( $y/H = 0.81$  and  $0.93$ ), no obvious cracks can be observed and the spherulites are only elongated. However, the lamellae inside the spherulites may

breakdown under tensile stress [173]. When the elongation increases to 40%, only a few cracks appear and the elongated spherulites are widened at  $y/H = 0.81$ , whereas no cracks are formed at  $y/H = 0.93$ .

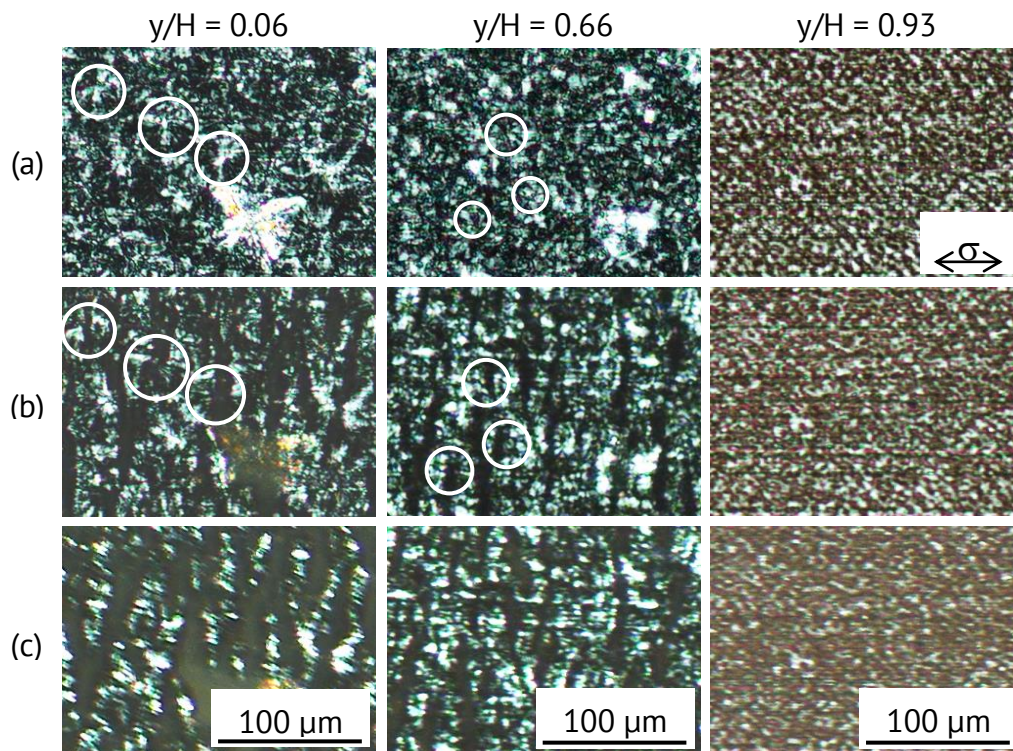


Figure 5.39: Optical micrographs from the polarized light microscope for different thickness ratios ( $y/H$ ) of the neat PP samples as a function of macroscopic elongation (a) 3%, (b) 20 and 40%. The black arrows indicate the direction of the tensile axis  $\sigma$ . The white circles represent of spherulites.

The distinct morphological deformation behaviors of neat PP at different  $y/H$  values can be attributed to the different morphologies along the thickness of the injection-molded part. This is due to the spherulites at the core being larger than at the skin, and because the sizes of spherulite boundaries at the core, which are usually considered as the weak point when being deformed, is also obviously smaller than at the skin [173]. Slower cooling rates at the core result in the segregation of impurities and the

formation of contraction voids at the boundaries, consequently weakening these regions and having a detrimental effect on the whole structure [122].

### PP/Nanoparticle Systems

As shown in Figures 5.40 and 5.41, the morphological deformation of PP filled with nanoparticles is quite different from neat PP. Figure 5.40 shows comparatively homogeneous surface morphology with an agglomeration of SiO<sub>2</sub> (white arrows).

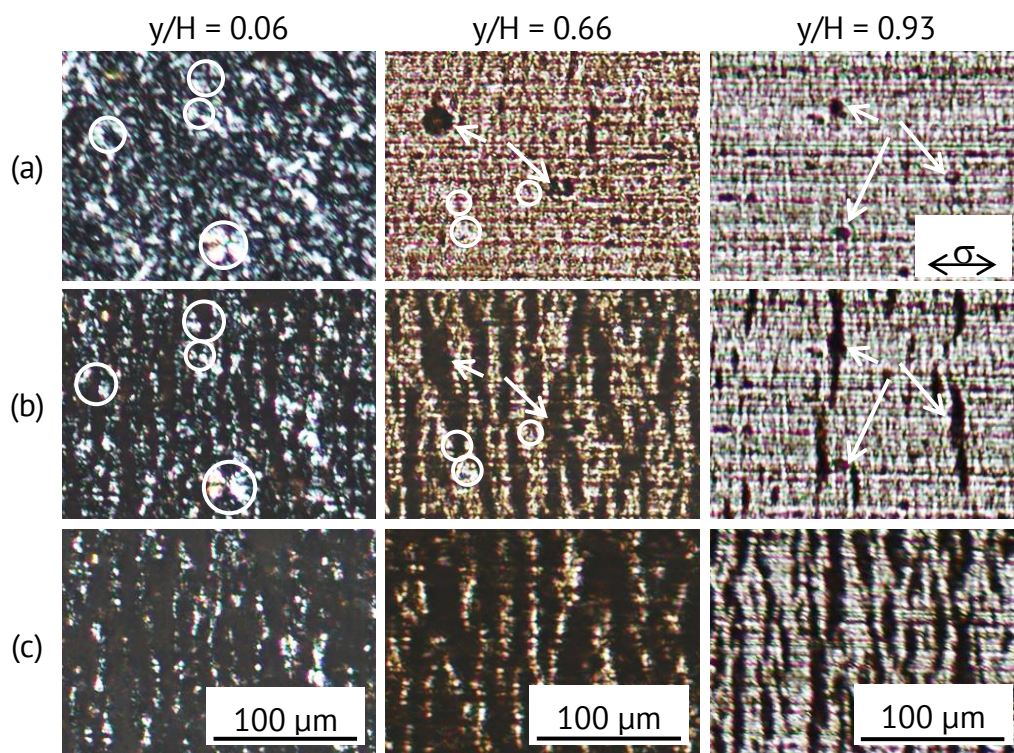


Figure 5.40: Optical micrographs from the polarized light microscope for different thickness ratios ( $y/H$ ) of the PP-S-V4 samples as a function of macroscopic elongation (a) 3%, (b) 10 and 20%. The black arrows indicate the direction of the tensile axis  $\sigma$ . The white circles represent of spherulites.

In Figure 5.41, on the other hand, large and elongated cavities (white arrows) are seen along the tensile direction in the PP-T-V4, suggesting a weak interfacial adhesion

between  $\text{TiO}_2$  and PP. In this case, debonding can easily occur and can introduce cracks of considerable sizes. Cracks mostly initiate at interface debonding at the elongation of 3%. As the elongation increases to 10% and 20%, more cracks are observed and the spherulites are broken. As the nanoparticle loading increases, more cracks emerge. Moreover, as compared to the core region, fewer cracks are observed at the skin region in all materials. By the investigation of thin sections, it is clear that the surface deformation of nanoparticle-filled PP is accompanied by interface debonding and spherulite breakdown.

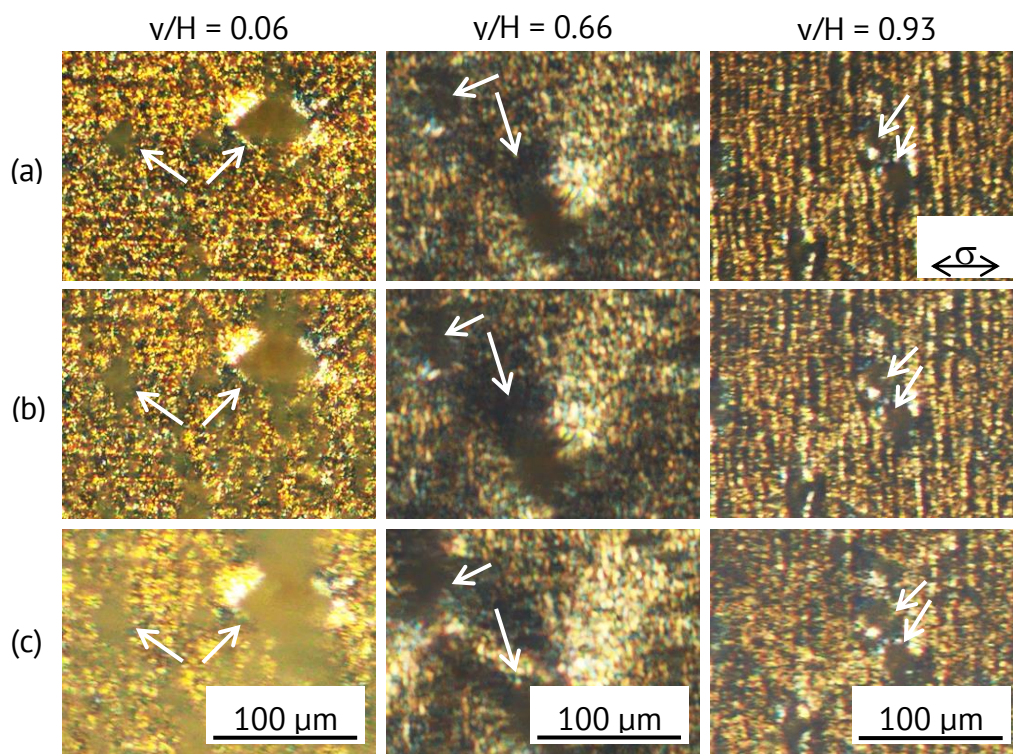


Figure 5.41: Optical micrographs from the polarized light microscope for different thickness ratios ( $v/H$ ) of the PP-T-V4 samples as a function of macroscopic elongation (a) 3%, (b) 10 and 20%. The black arrows indicate the direction of the tensile axis  $\sigma$ .

In present work, the deformation of PP is considered in terms of a spherulitic structure. It needs to emphasize that the practical consideration carried out on thin section, which is all observation and deduction were made on two-dimensional spherulities. This

---

leaves the question of whether the deformation noted can be applied to bulk sample, which exhibit three-dimensional spherulitic structure. However, the results enable us to understand the local behavior of microstructures in relation to macroscopic deformation of the bulk sample.

## 6. Summary

This present work focuses on the investigation of the morphological development of PP containing different types of nanoparticles, i.e. SiO<sub>2</sub> and TiO<sub>2</sub>. The nanocomposites were prepared by melt compounding followed by injection molding.

Investigations of crystallization by mean of flash DSC allow for a closer look to crystallization processes at industrially relevant conditions. It is found that the  $\alpha$ -phase, which is essentially formed, occurs most frequently over a wide of cooling rate, while  $\beta$ -phase only forms on cooling at rates lower than about 1 K/s. A cooling rate faster than 100K/s leads to the formation of the mesophase.

In comparison to neat PP the presence of nanoparticles only affects the crystallization of  $\alpha$ -phase. This supports the idea that crystallization of  $\alpha$ -phase is governed by heterogeneous nucleation, while the homogeneous nucleation dominates the crystallization of mesophase. Furthermore, the mesophase of PP is not influenced by the SiO<sub>2</sub> nanoparticles, while it is obstructed by the presence of high TiO<sub>2</sub> nanoparticle loadings. However, the increase of the overall crystallization rate is related to increases of the nucleation rate, and not an increase of the crystal growth rate. Based on the isothermal experimental results a simple mathematical model can be introduced to describe the relationship between temperature, filler loading, and crystallization rate, whereas the relationship between cooling rate, filler loading, and crystallization temperature are also proposed based on the non-isothermal crystallization.

The analysis of melting behaviors obtained after each undercooling reveals that crystal perfection increases significantly with the incorporation of TiO<sub>2</sub> nanoparticles, while it is not influenced by the SiO<sub>2</sub> nanoparticles.

The analysis of the morphological distribution throughout the thickness of samples shows that nanoparticles have a profound influence on the morphology of injection-molded parts. The relative thickness of the oriented region increases with the incorporation of nanoparticles. The spherulite size of PP significantly shifts to lower values from the core toward the skin layer in both neat PP and PP nanocomposites. Additionally, the spherulite size decreases with increasing nanoparticle loading. Moreover, the DSC analysis proved that the degree of crystallinity of both neat PP and PP nanocomposites decreased from the core to the skin layer. The presence of SiO<sub>2</sub> nanoparticles decreases the degree of crystallinity of PP. In contrast, the degree of crystallinity increases with increasing TiO<sub>2</sub> nanoparticle loading.

The micro-tensile testing results exhibit significant dependence of the tensile properties on the location along the wall thickness. The investigation was performed under plain stress condition. Neat PP shows an increasing tendency of the tensile strength as the normalized thickness decreases. This is due to the presence of a higher amount of crystallinity with a greater spherulite size at the core of the samples. Also for nanoparticle-filled PP, the results show an increasing tendency of the tensile strength and a decrease in the elongation at break from the skin to the core. In this case, the tensile properties are thus considered to be a result of two contributions: the microstructure effect, in which slower cooling results in greater crystallinity and thus greater spherulite strength, and the nucleation effect, in which higher nanoparticle loading results in smaller spherulites.

## 7. References

- [1] Chrissafis, K. and Bikiaris, D.: Can Nanoparticles Really Enhance Thermal Stability of Polymers? Part I: An Overview on Thermal Decomposition of Addition Polymers. *Thermochimica Acta* 523 (2011), pp. 1-24.
- [2] Chan, C. M., Wu, J., Li, J. X. and Cheung, Y. K.: Polypropylene/Calcium Carbonate Nanocomposites. *Polymer* 43 (2002), pp. 2981-2992.
- [3] Pustak, A., Pucić, I., Denac, M., Švab, I., Pohleven, J., Musil, V. and Šmit, I.: Morphology of Polypropylene/Silica Nano- and Microcomposites. *Journal of applied polymer science* (2013), pp. 3099-3106.
- [4] Zhou, Z., Wang, S., Lu, L., Zhang, Y. and Zhang, Y. Isothermal Crystallization Kinetics of Polypropylene with Silane Functionalized Multi-Walled Carbon Nanotubes. *Journal of Polymer Science: Part B: Polymer Physics* 45 (2007), 1616-1624.
- [5] Ruksakulpiwat, Y., Suppakarn, N., Sutapun, W. and Thomthong, W.: Vetiver – Polypropylene Composites: Physical and Mechanical Properties. *Composites Part A: Applied Science and Manufacturing* 38 (2002), pp. 590-601.
- [6] Altan, M. and Yildirim, H.: Mechanical and Morphology Properties of Polypropylene and High Density Polyethylene Matrix Composites Reinforced with Surface Modified Nano Sized TiO<sub>2</sub> Particles. *World Academy of Science, Engineering and Technology* 4 (2010), pp. 246-251.
- [7] Zhou, T. H., Ruan, W. H., Mai, Y. L., Rong, M.Z. and Zhang, M. Q.: Performance Improvement of Nano-Silica/Polypropylene Composites Through In-situ Cross-

- linking Approach. *Composites Science and Technology* 68 (2008), pp. 2858-2863.
- [8] Kanig, G.: Neue elektronenmikroskopische Untersuchungen über die Morphologie von Polyäthylenen. *Progress in Colloid and Polymer Science* 57 (1975), pp. 176-191.
- [9] Katti, S. S. and Schultz, J. M.: The Microstructure of Injection-Molded Semicrystalline Polymers: A Review. *Polymer Engineering and Science* 22 (1982), pp. 1001-1017.
- [10] Ajayan, P.M., Braun, P.V., Schadler, L.S.: *Nanocomposite Science and Technology*. Weinheim: Wiley-VCH 2003.
- [11] Sun, C.: *Controlling the Rheology of Polymer/Silica Nanocomposites*. PhD. Thesis. Eindhoven University of Technology, The Netherlands. 2010.
- [12] Kumar, A. P., Depan, D., Tomer, N. S. and Singh, R. PP.: Nanoscale Particles for Polymer Degradation and Stabilization-Trends and Future Perspectives. *Progress in Polymer Science* 34 (2009), pp. 479-515.
- [13] Natta, G. and Danusso, F.: *Stereoregular Polymers and Stereospecific Polymerizations: The Contributions of Giulio Natta and His School to Polymer Chemistry Volume 1*. London, 1967.
- [14] Stournara, M. E. and Ramprasad, R.: A First Principles Investigation of Isotactic Polypropylene. *Journal of Materials Science* 45 (2010), pp. 443-447.
- [15] Padden Jr., F. J. and Keith, H. D.: Spherulitic Crystallization in Polypropylene. *Journal of Applied Physics* 30 (1959), pp. 1479-1484.
- [16] Crissman, J. M.: Mechanical Relaxation in Polypropylene as a Function of Polymorphism and Degree of Lamella Orientation. *Journal of Polymer Science: Part A-2* 7 (1969), pp. 389-404.

- [17] Lovinger, A. J., Chua, J. O. and Gryte, C. C.: Studies on the  $\alpha$  and  $\beta$  Forms of Isotactic Polypropylene by Crystallization in a Temperature Gradient. *Journal of Polymer Science: Polymer Physics Edition* 15 (1977), pp. 641-656.
- [18] Dragaun, H., Hubeny, H. and Muschik, H.: Shear-Induced  $\beta$ -Form Crystallization in Isotactic Polypropylene. *Journal of Polymer Science: Polymer Physics Edition* 15 (1977), pp. 1779-1789.
- [19] Varga, J. and Karger-Kocsis, J.: Direct Evidence of Row-Nucleated Cylindric Crystallization in Glass Fiber-Reinforced Polypropylene Composites. *Polymer Bulletin* 30 (1993), pp. 105-110.
- [20] Jacoby, P., Bersted, B. H., Kissel, W. J. and Smith, C. E.: Studies on the  $\beta$ -Crystalline Form of Isotactic Polypropylene. *Journal of Polymer Science: Part B: Polymer Physics* 24 (1986), pp. 461-491.
- [21] Varga, J.: Review Supermolecular Structure of Isotactic Polypropylene. *Journal of Materials Science* 27 (1992), pp. 2557-2579.
- [22] Varga, J., Mudra, I. and Ehrenstein, G. W.: Highly Active Thermally Stable  $\beta$ -Nucleating Agents for Isotactic Polypropylene. *Journal of Applied Polymer Science* 74 (1999), pp. 2357-2368.
- [23] Turner Jones, A., Aizlewood, J. M. and Beckett, D. R.: Crystalline Forms of Isotactic Polypropylene. *Die Makromolekulare Chemie* 75 (1964), pp. 134-158.
- [24] Zhang, Q.-X., Yu, Z.-Z., Xie, X.-L. and Mai Y.-W.: Crystallization and Impact Energy of Polypropylene/CaCO<sub>3</sub> Nanocomposites with Nonionic Modifier. *Polymer* 45 (2005), pp. 5985-5994.
- [25] Zuiderduin, W. C. J., Westzaan, C., Huétink, J. and Gaymans, R. J.: Toughening of Polypropylene with Calcium Carbonate Particles. *Polymer* 44 (2003), pp. 261-275.

- [26] Schlarb, A. K., Suwitaningsih, D. N., Kopnarski, M. and Niedner-Schatteburg, G.: On the Supermolecular Morphology of Polypropylene Filled with Nanosized Silica. *Journal of Applied Polymer Science* 131 (2014), 39655 (1-8).
- [27] Bikiaris, D. N., Papageorgiou, G. Z., Pavlidou, E., Vouroutzis, N., Palatzoglou, P. and Karayannidis, G. P.: Preparation by Melt Mixing and Characterization of Isotactic Polypropylene/SiO<sub>2</sub> Nanoparticles Containing Untreated and Surface-Treated Nanoparticles. *Journal of Applied Polymer Science* 100 (2006), pp. 2684–2696.
- [28] Vladimirov, V., Betchev, C., Vassiliou, A., Papageorgiou, G. and Bikiaris, D.: Dynamic Mechanical and Morphological Studies of Isotactic Polypropylene/Fumed Silica Nanocomposites with Enhanced Gas Barrier Properties. *Composites Science and Technology* 66 (2006), pp. 2935-2944.
- [29] Mikešová, J., Šlouf, M., Gohs, U., Popelková, D. Vacková, T., Vu, N. H., Kratochvíl, J. and Zhigunov, A.: Nanocomposites of Polypropylene/Titanate nanotubes: Morphology, Nucleation Effects of Nanoparticles and Properties. *Polymer Bulletin* 71 (2014), pp. 795-818.
- [30] Zohrevand, A., Ajji, A. and Mighri, F.: Morphology and Properties of Highly Filled iPP/TiO<sub>2</sub> nanocomposites. *Polymer Engineering and Science* (2014), pp. 874-886.
- [31] Technical Bulletin Fine Particles 11, Evonik Degussa GmbH, Hanau, Germany (2006).
- [32] Davis, K. A.: Titanium Dioxide. *Chemical of the Month, The Culver Academies* 59 (1982), pp. 158-159.
- [33] Tang, H., Prasad, K., Sanjinès, R., Schmid, P. E. and Lévy, F.: Electrical and Optical Properties of TiO<sub>2</sub> Anatase Thin Film. *Journal of Applied Physics* 75 (1994), pp. 2042-2047.

- [34] Ahmadpoor, P. Nateri, A. S., Motaghitalab, V.: The Optical Properties of PVA/TiO<sub>2</sub> Composites Nanofibers. *Journal of Applied Polymer Science* (2013), pp. 78-85.
- [35] Knör, N., Hauptert, F. and Schlarb, A. K.: Nanoverbundwerkstoffe - eine neue Materialklasse mit verbesserter Steifigkeits-/Zähigkeitsrelation. IVW-Kolloquium 2008, Kaiserslautern, 16./17. September 2008.
- [36] Zheng, J. Z., Zhou, X. P., Xie, X. L. and Mai, Y. W.: Silica Hybrid Particles with Nanometre Polymer Shells and Their Influence on the Toughening of Polypropylene. *Nanoscale* 2 (2010), pp. 2269-2274.
- [37] Avella, M., Cosco, S., Di Lorezo, M. L., Di Pace, E., Errico, M. E., Gentile, G.: Nucleation Activity of Nanosized CaCO<sub>3</sub> on Crystallization of Isotactic Polypropylene, in Dependence on Crystal Modification, Particle Shape, and Coating. *European Polymer Journal* 42 (2006), pp. 1548-1557.
- [38] Asuka, K. Liu, B., Terano, M. and Nitta, K. H.: Homogeneously Dispersed Poly(propylene)/SiO<sub>2</sub> Nanocomposites with Unprecedented Transparency. *Macromolecular Rapid Communications* 27 (2006), pp. 910-913.
- [39] Chen, M., Tian, G., Zhang, Y., Wan, C. And Zhang, Y.: Effect of Silican Dioxide on Crystallization and Melting Behavior of Polypropylene. *Journal of Applied Polymer Science* 100 (2006), pp. 1889-1898.
- [40] Wunderlich B.: *Macromolecular Physics, Vol. 2 Crystal Nucleation, Growth, Annealing*; Acedemic Press: New York, 1976.
- [41] Young R. J. and Lovell P. A.: *Introduction to Polymer*; Chapman & Hall: London, 1991.
- [42] Ehrenstein, G. W. *Polymeric Materials: Structure-Properties-Applications*.
- [43] D. C. Bassett, "Polymer Morphology - Pure and applied," *Journal of Macromolecular Science, Part B*, vol. 35, no. 3, pp. 277-294, 1996.

- [44] Keith H. D. and Padden F. J. J.: Spherulitic Crystallization from the Melt. I. Fractionation and Impurity Segregation and Their Influence on Crystalline Morphology. *Journal of Applied Physics* 35 (1964), pp. 1270-1285.
- [45] Keith H. D. and Padden F. J. J.: Spherulitic Crystallization from the Melt. II. Influence of Fractionation and Impurity Segregation on the Kinetics of Crystallization. *Journal of Applied Physics* 35 (1964), pp. 1286-1296.
- [46] Supaphol P. and Spruiell J. E. J.: Application of Avrami, Tobin, Malkin, and Simultaneous Avrami Macrokinetic Models to Isothermal Crystallization of Syndiotactic Polypropylenes. *Journal of Macromolecular Science, Part B: Physics* 39 (2000), pp. 257-277.
- [47] University of Virginia, Introduction to the Science and Engineering of Materials, Chapter 15. Polymer Structures (2004), <http://www.virginia.edu/>
- [48] Kantz, M. R., Newman, H. D. and Stigale, F. H.: The Skin-Core Morphology and Structure-Property Relationships in Injection-Molded Polypropylene. *Journal of Applied Polymer Science* 16 (1972), pp. 1249-1260.
- [49] Guo, X., Isayev, I. and Gou, L.: Crystallinity and Microstructure in Injection Moldings of Isotactic Polypropylenes. Part 1: A New Approach to Modeling and Model Parameters. *Polymer Engineering and Science* 39 (1999), pp. 2096-2114.
- [50] Al-Mulla A.: Isothermal Crystallization Kinetics of Poly(ethylene terephthalate) and Poly(methyl methacrylate) Blends. *Express Polymer Letters* 1 (2007), pp. 334-444.
- [51] Avalos F., Lopez-Manchado M. A. and Arroyo M.: Crystallization Kinetics of Polypropylene: 1. Effect of Small Additions of Low-density Polyethylene. *Polymer* 37 (1996), pp. 5681-5688.

- 
- [52] Avrami M. J.: Kinetics of Phase Change. I General Theory. The Journal of Chemical Physics 7 (1939), pp. 1103-1112.
- [53] Avrami M. J.: Kinetics of Phase Change. II Transformation Time Relations for Random Distribution of Nuclei. The Journal of Chemical Physics 8 (1940), pp. 212-224.
- [54] Avrami M. J.: Granulation, Phase Change, and Microstructure Kinetics of Phase Change. III. The Journal of Chemical Physics 9 (1941), pp. 177-183.
- [55] Tobin M. C. J.: Theory of Phase Transition Kinetics with Growth Site Impingement. I. Homogeneous Nucleation. Journal of Polymer Science: Polymer Physics Edition 12 (1974), pp. 399-406.
- [56] Tobin M. C. J.: The Theory of Phase Transition Kinetics with Growth Site Impingement. II. Heterogeneous Nucleation. Journal of Polymer Science: Polymer Physics Edition 14 (1976), pp. 2253-2257.
- [57] Tobin M. C. J.: Theory of Phase Transition Kinetics with Growth Site Impingement. III. Mixed Heterogeneous- Homogeneous nucleation and Nonintegral Exponents of the Time. Journal of Polymer Science: Polymer Physics Edition 15 (1977), pp. 2269-2270.
- [58] Malkin A. Y., Beghishev V. P., Keapin I. A. and Bolgov S. A.: General Treatment of Polymer Crystallization Kinetics-Part 1. A New Macrokinetic Equation and its Experimental Verification. Polymer Engineering Science 24 (1984), pp. 1396-1401.
- [59] Hillier I. H. J.: Modified Avrami Equation for the Bulk Crystallization Kinetics of Spherulitic Polymers. Journal of Polymer Science Part A: Polymer Chemistry 3 (1965), pp. 3067-3078.

- [60] Price F. P. J.: A Phenomenological Theory of Spherulitic Crystallization: Primary and Secondary Crystallization Processes. *Journal of Polymer Science Part A: Polymer Chemistry* 3 (1965), pp. 3079-3086.
- [61] Ravindranath K. and Jog J. P.: Polymer Crystallization Kinetics: Poly (ethylene terephthalate) and Poly ( phenylene sulfide). *Journal of Applied Polymer Science* 49 (1993), pp. 1395-1403.
- [62] Hay J. N.: Application of the Modified Avrami Equations to Polymer Crystallisation Kinetics. *British Polymer Journal* 3 (1971), pp. 74-82.
- [63] Bicerano J.: Crystallization of Polypropylene and Poly(Ethylene Terephthalate). *Journal of Macromolecular Science, Part C: Polymer Reviews* 38 (1998), pp. 391-479.
- [64] Lauritzen, J. I. and Hoffman, J. D.: Extension of Theory of Growth of Chain-Folded Polymer Crystals to Large Undercoolings. *Journal of Applied Physics* 44 (1973), pp. 4340-4352.
- [65] Papageorgiou, G. Z., Achilias, D. S., Bikiaris, D. N. and Karayannidis, G. P.: Crystallization Kinetics and Nucleation Activity of Filler in Polypropylene/Surface-Treated SiO<sub>2</sub> Nanocomposites. *Thermochimica Acta* 427 (2005), pp. 117-128.
- [66] Patel, R. M. and Spruiell, J. E.: Crystallization Kinetics during Polymer Processing- Analysis of Available Approaches for Process Modeling. *Polymer Engineering and Science* 31 (1991), pp. 730-738.
- [67] Zhou, W. Y., Duan, B., Wang, M. and Cheung, W. L.: Isothermal and Non-isothermal Crystallization Kinetics of Poly(L-Lactide)/Carbonated Hydroxyapatite Nanocomposites Microspheres. *Advances in Diverse Industrial Applications of Nanocomposites* (2011), Dr. Boreddy Reddy (Ed.), pp. 231-260.

- [68] Rabello, M. S. and White, J. R.: Crystallization and melting behavior of photodegraded polypropylene-II. Re-crystallization of degraded molecules. *Polymer* 38 (1997), pp. 6389-6399.
- [69] Hoffman, J. D. and Weeks, J. J.: Melting Process and the Equilibrium Melting Temperature of Polychlorotrifluoroethylene. *Journal of Research of the National Bureau of Standards-A. Physics and Chemistry* 66A (1962), pp. 13-28.
- [70] Murphy, C. J., Henderson, JR. G. V. S., Murphy, E. A., and Sperling, L. H.: The Relationship Between the Equilibrium Melting Temperature and the Supermolecular Structure of Several Polyoxetanes and Polyethylene Oxide. *Polymer Engineering and Science* 27 (1987), 781-787.
- [71] Aziz, M. S. A., Naguib, H. F. and Saad, G. R.: Non-isothermal Crystallization Kinetics of Bacterial Poly(3-hydroxybuturate) in Poly(3-hydroxybutyrate-co-butylene adipate) Urethanes. *Thermochimica Acta* 591 (2014), pp. 130-139.
- [72] Ding, Z. and Spruiell, J. E.: Interpretation of the Nonisothermal Crystallization Kinetics of Polypropylene Using a Power Law Nucleation Rate Function. *Journal of Polymer Science: Part B Polymer Physics* 35 (1997), pp. 1077-1093.
- [73] Yuan, Q., Awate, S. and Misra, R. D. K.: Nonisothermal Crystallization Behavior of Polypropylene-Clay Nanocomposites. *European Polymer Journal* 42 (2006), pp. 1994-2003.
- [74] Kissinger, H. E.: Variation of Peak Temperature with Heating Rate in Differential Thermal Analysis. *Journal of Research of the National Bureau of Standards* 57 (1956), pp. 217-221.
- [75] Zhang, Z. Chen, J. Liu, H. And Xiao, C.: Applicability of Kissinger Model in Nonisothermal Crystallization Assessed using a Computer Simulation Method. *Journal of Thermal Analysis and Calorimetry* 117 (2014), pp. 783-787.

- [76] Brucato, V. Piccarolo, S. Carrubba, V. L.: An Experimentat Methodology to Study Polymer Crystallization under Processing Conditions. The Influence of High Cooling Rates. *Chemical Engineering Science* 57 (2002), pp. 4129-4143.
- [77] Minakov, A. A. and Schick, C.: Ultrafast Thermal Processing and Nanocalorimetry at Heating and Cooling Rates up to 1MK/s. *Review of Scientific Instruments* 78 (2007), pp. 073902-073902-10.
- [78] Schick, C.: Differential Scanning Calorimetry (DSC) of Semicrystalline Polymers. *Analytical and Bioanalytical Chemistry* 395 (2009), pp. 1589-1611.
- [79] Mathot, V., Pyda, M., Pijpers, T., Poel, G. V., van de Kerkhof, E., van Herwaarden, S. van Herwaarden, F. and Leenaers, A.: The Flash DSC1, a Power Compecsation Twin-Type, Chip-Based Fast Scanning Calorimeter (FSC): First Findings on Polymers. *Thermochimica Acta* 522 (2011), pp. 36-45.
- [80] Kolesov, I., Mileva, D., Androsch, R. and Schick, C.: Structure Formation of Polyamide 6 from the Glassy State by Fast Scanning Chip Calorimetry. *Polymer* 52 (2011), pp. 5156-5165.
- [81] Kolesov, I., Androsch, R., Mileva, D., Lebek, W., Benhamida, A., Kaci, M. and Focke, W.: Crystallization of a Polymide 11/Organo-Modified Montmorillonite Nanocomposite at Rapid Cooling. *Colloid and Polymer Science* 291 (2013), pp. 2541-2549.
- [82] Mollova, A., Androsch, R., Mileva, D., Schuck, C. and Benhamida, A.: Effect of Supercooling on Crystallization of Polyamide 11. *Macromolecules* 46 (2013), pp. 828-835.
- [83] Schawe, J. E. K.: Influence of Processing Conditions on Polymer Crystallization Measured by Fast Scanning DSC. *Journal of Thermal Analysis and Calorimetry* 116 (2014), pp. 1165-1173.

- [84] Wurm, A., Herrmann, A., Cornelius, M., Zhuravlev, E., Pospiech, D., Nicula, R. and Schick, C.: Temperature Dependency of Nucleation Efficiency of Carbon Nanotubes in PET and PBT. *Macromolecular Materials and Engineering* 300 (2015), pp. 637-649.
- [85] Androsch, R. and Lorenzo, M. L. D.: Kinetics of Crystal Nucleation of Poly(L-lactic acid). *Polymer* 54 (2013), pp. 6882-6885.
- [86] Cocca, M., Androsch, R., Righetti, R. C., Malinconico, M. and Lorenzo, M. L. D.: Conformationally Disordered Crystals and Their Influence on Material Properties: The Cases of Isotactic Polypropylene, Isotactic Poly(1-butene), and Poly(L-lactic acid). *Journal of Molecular Structure* 1078 (2014), pp. 114-132.
- [87] Bosq, N., Guigo, N., Zhuravlev, E. and Sbirrazzuoli, N.: Nonisothermal Crystallization of Polytetrafluoroethylene in a Wide Range of Cooling Rates. *The Journal of Physical Chemistry B* 117 (2013), pp. 3407-3415.
- [88] Stolte, I., Androsch, R., Lorenzo, M. L. D. and Schick, C.: Effect of Aging the Glass of Isotactic Polybutene-1 on Form II Nucleation and Cold Crystallization. *The Journal of Physical Chemistry B* 117 (2013), 15196-15203.
- [89] Mollova, A., Androsch, R., Mileva, D., Gahleitner, M. and Funari, S.: Crystallization of Isotactic Polypropylene Containing Beta-Phase Nucleating Agent at Rapid Cooling. *European Polymer Journal* 49 (2013), pp. 1057-1065.
- [90] Schawe, J. E. K.: Analysis of non-isothermal crystallization during cooling and reorganization during heating of isotactic polypropylene by fast scanning DSC. *Thermochimica Acta* 603 (2015), pp. 85-93.
- [91] Schawe, J. E. K., Vermeulen, P. A. and van Drongelen, M.: A new Crystallization Process in Polypropylene Highly Filled with Calcium Carbonate. *Colloid and Polymer Science* 293 (2015), pp. 1607-1614.

- [92] Luijsterburg, B. J., de Kort, G. W., van Drongelen, M., Govaert, L. E. and Goossens, J. G. P.: Fast Cooling of (non)-Nucleated Virgin and Recycled Poly(propylene): Effect of Processing Conditions on Structural and Mechanical Properties. *Thermochimica Acta* 603 (2015), pp. 94-102.
- [93] Tan, V. and Kamal, M. R.: Morphological Zones and Orientation in Injection-Molded Polyethylene. *Journal of Applied Polymer Science* 22 (1978), pp. 2341-2355.
- [94] Devaux, N., Monasse, B., Haudin, J. M., Moldenaers, P. and Vermant, J.: Rheo-optical Study of the Early Stages of Flow Enhanced Crystallization in Isotactic Polypropylene. *Rheologica Acta* 43 (2004), pp. 210-222.
- [95] Schrauwen, B. A. G., Breemen, L. C. A. V., Spoelstra, A. B., Govaert, L. E., Peters, G. W. M. and Meijer, H. E. H.: Structure, Deformation, and Failure of Flow-Oriented Semicrystalline Polymers. *Macromolecules* 37 (2004), pp. 8618-8633.
- [96] Meister, S. and Drummer, D.: Influence of Mold Temperature on Molding Filling Behaviour and Part Properties in Micro Injection Molding. *International Polymer Processing* 28 (2013), pp. 550-557.
- [97] Drummer, D. and Meister, S.: Correlation of Processing, Inner Structures, and Part Properties of Injections Moulded Thin-Wall Parts on Example of Polyamide 66. *International Journal of Polymer Science* 2014 (2014), pp. 1-8.
- [98] Fitchmun, D. R. and Mencik, Z.: Morphology of Injection-Molded Polypropylene. *Journal of Polymer Science* 11 (1973), pp. 951-971.
- [99] Housmans, J. W., Gahleitner, M., Peters, G. W. M. and Meijer, H. E. H.: Structure-Property Relations in Molded, Nucleated Isotactic Polypropylene. *Polymer* 50 (2009), pp. 2304-2319.

- [100] Zhang, Y., Zhang, J., Qian, X., Deng, P. and Shen, K.: Morphology Evolution Including Formation of Cylindrulite in Isotactic Polypropylene Devided from Periodical Shear Field. *Polymer* 53 (2012), pp. 4318-4327.
- [101] Hegler, R. P., Altstädt, V., Ehrenstein, G. W. and Mennig, G.: Einfluss stofflicher Parameter auf die Faserorientierung beim Verarbeiten. kurzfaserverstärkter Thermoplaste, *Kunststoffe* 9 (1986), 766-771.
- [102] Jarus, D., Scheibelhoffer, A., Hiltner, A. and Baer, E.: The Effect of “Skin-Core” Morphology on the Heat-Deflection Temperature of Polypropylene. *Journal of Applied Polymer Science* 60 (1996), pp. 209-219.
- [103] Wenig, W. and Herzog, F.: Injection Molding of Polypropylene: X-Ray Investigation of the Skin-Core Morphology. *Journal of Applied Polymer Science* 50 (1993), pp. 2163-2171.
- [104] Zhu, P. W., Tung, J., Phillips, A. and Edward, G.: Morphological Development of Oriented Isotactic Polypropylene in the Presence of a Nucleating Agent. *Macromolecules* 39 (2006), pp. 1821-1831.
- [105] Liu, G., Zhu, P. W. and Edward, G.: Morphology Distribution and Processing History of Injection Moulded Polypropylenes. *Macromolecular Symposia* 185 (2002), pp. 327-340.
- [106] Pantani, R., Speranzu, V., Coccorullo, I. and Titomanlio, G.: Morphology of Injection Molded iPP Samples. *Macromolecular Symposia* 185 (2002), pp. 309-326.
- [107] Pantani, R. Balzano, L. and Peters, G. W. M.: Flow-Induced Morphology of iPP Solidified in a Shear Deice. *Macromolecular Materials and Engineering* 297 (2012), pp. 60-67.

- [108] Radhakrishnan, S., Sonawane, P. and Pawaskar, N.: Effect of Thermal Conductivity and Heat Transfer on Crystallization, Structure, and Morphology of Polypropylene Containing Different Fillers. *Journal of Applied Polymer Science* 93 (2004), pp. 615-623.
- [109] Moretti, F., Favaro, M. M., Branciforti, M. C. and Bretas, R. E. S.: Optical Monitoring of the Injection Molding of Intercalated Polypropylene Nanocomposites. *Polymer Engineering and Science* 50 (2010), pp. 1326-1339.
- [110] Somnuk, U., Suppakarn, N., Sutapun, W. and Ruksakulpiwat, Y.: Shear-Induced Crystallization of Injection Molded Vetiver Grass-Polypropylene Composites. *Journal of Applied Polymer Science* 113 (2009), pp. 4003-4014.
- [111] Ferreiro, V., Pennec, Y., Séguéla, R. and Coulon, G.: Shear Banding in Polyamide 6 Films as Revealed by Atomic Force Microscopy. *Polymer* 41 (2000), pp. 1561-1569.
- [112] Butler, M. F. and Donald, A. M.: Deformation of Spherulitic Polyethylene Thin Films. *Journal of Materials Science* 32 (1997), pp. 3675-3685.
- [113] Geil, P. H.: Polymer Deformation. II. Drawing of Polyethylene Single Crystals. *Journal of Polymer Science. Part A 2* (1964), pp. 3813-3833.
- [114] Hay, I. L. and Keller A.: Polymer Deformation in Term of Spherulites. *Kolloid-Zeitschrift und Zeitschrift für Polymere* 204 (1965), pp. 43-73.
- [115] Bowden, P. B. and Young, R. J.: Review Deformation Mechanism in Crystalline Polymers. *Journal of Materials Science* 9 (1974), pp. 2034-2051.
- [116] Lin, L. and Argon, A. S.: Review Structure and Plastic Deformation of Polyethylene. *Journal of Materials Science* 29 (1994), pp. 294-323.
- [117] Way, J. L. and Atkinson, J. R.: Some Studies of Deformation Processes in Fully-Spherulitic Polypropylene. *Journal of Materials Science* 6 (1971), pp. 102-109.

- [118] Weynant, E. and Haudin, J. M.: In situ Observation of the Spherulite Deformation in Polybutene-1 (Modification I). *Journal of Materials Science* 15 (1980), pp. 2677-2692.
- [119] Haas, T. W. and Mac Rae P. H.: Microscopic Observations of Fracture in Spherulitic Films of Polybutene-1. *Polymer Engineering and Science* 9 (1969), pp. 423-427.
- [120] Zhou, H. and Wilkes, G. L.: Orientation-Dependent Mechanical Properties and Deformation Morphologies for Uniaxially Melt-Extruded High-Density Polyethylene Films Having an Initial Stacked Lamellar Texture. *Journal of Materials Science* 33 (1998), pp. 287-303.
- [121] Starkweather JR., H. W. and Brook R. E.: Effect of Spherulites on the Mechanical Properties of Nylon 66. *Journal of Applied Polymer Science* 1 (1959), pp. 236-239.
- [122] Way, J. L., Atkinson, J. R. and Nutting, J.: The Effect of Spherulite Size on the Fracture Morphology of Polypropylene. *Journal of Materials Science* 9 (1974), pp. 293-299.
- [123] Maiti, S. N. and Mahapatro, P. K.: Crystallization of PP in PP/Ni Composites and its Correlation with Tensile Properties. *Journal of Applied Polymer Science* 37 (1989), pp. 1889-1899.
- [124] Steger, T. R. and Nielsen, L. E.: Microvoid Formation during Deformation of High Impact Polystyrene. *Journal of Polymer Science: Polymer Edition* 16 (1978), pp. 613-625.
- [125] Lin, L.: Processing Controlled Properties of Thermoplastic-Based Nanocomposites. Kaiserslautern, PhD Thesis (2013)
- [126] Evonik, Product Information Aerosil R8200, [www.aerosil.com](http://www.aerosil.com)

- [127] Huntsman, Product Information, Hombitec RM 130 F, [www.sachtleben.de](http://www.sachtleben.de)
- [128] Bassett, D.C. and Olley, R.H.: On the Lamellar Morphology of Isotactic Polypropylene Spherulites . *Polymer* 25 (1984), pp. 935–943.
- [129] Shahin, M.M., Olley, R. H. and Blissett, M. J.: Refinement of Etching Techniques to Reveal Lamellar Profiles in Polyethylene Banded Spherulites. *Journal of Polymer Science Part B: Polymer Physics* 37 (1999), pp. 2279-2286.
- [130] Liu, X., Dai, K., Hao, X., Zheng, G., Liu, C., Schubert, D. W. and Shen, C.: Crystalline Structure of Injection Molded  $\beta$ -Isotactic Polypropylene: Analysis of the Oriented Shear Zone. *Industrial & Engineering Chemistry Research* 52 (2013), pp. 11996-12002.
- [131] Garcia, M., van Vliet, G. V., Jain, S., Schrauwen, B. A. G., van Zyl, W. E. and Boukamp, B.: Polypropylene/SiO<sub>2</sub> Nanocomposites with Improved Mechanical Properties. *Reviews on Advanced Materials Science* 6 (2004), pp. 169-175.
- [132] Lu, L. Alamo, R. G. and Mandelkern, L.: Lamellar Thickness Distribution in Linear Polyethylene and Ethylene Copolymer. *Macromolecules* 27 (1994), pp. 6571-6576.
- [133] Clark, E. J. and Hoffman, J. D.: Regime III Crystallization in Polypropylene. *Macromolecules* 17 (1984), pp. 878-885.
- [134] Schawe, J. E. K.: Practical Aspects of the Flash DSC 1: Sample Preparation for Measurements of Polymers. *Mettler Toledo Thermal Analysis UserCom* 36 (2012), pp. 17-24.
- [135] Poel, G. V., Istrate, D. Magon, A. and Mathot, V.: Performance and Calibration of the Flash DSC 1, a new MEMS-Based Fast Scanning Calorimeter. *Journal of Thermal Analysis and Calorimetry* 110 (2012), pp. 1533-1546.

- [136] Androsch R., Lorenzo M. L. D., Schick C., Wunderlich B.: Mesophase in Polyethylene, Polypropylene, and Poly(1-butene). *Polymer* 51 (2010), pp. 4639-4662.
- [137] Griffith J. H. and Ranby B. G. J. Crystallization Kinetics of Isotactic Polypropylene. *Journal of Polymer Science* 38 (1959), pp. 107-116.
- [138] Lim G. B. A. and Lloyd D. R.: Isothermal Crystallization of Isotactic Polypropylene in Dotriacontane. I: Effect of Nucleating Agent Addition on Overall Crystallization Kinetics. *Polymer Engineering Science* 33 (1993), pp. 513-521.
- [139] Albano C., Papa J., Ichazo M., González J. and Usrariz C.: Application of Different Macrokinetic Models to the Isothermal Crystallization of PP/talc Blends. *Composite Structures* 62 (2003), pp. 291–302.
- [140] Avramov, I, Avramova, K. and Rüssel, C.: New Method to Analyze Data on Overall Crystallization Kinetics. *Journal of Crystal Growth* 285 (2005), pp. 394-399.
- [141] Sun, N. X., Liu, X. D. and Lu, K.: An Explanation to the Anomalous Avrami Exponent. *Scripta Materialia* 34 (1996), pp. 1201-1207.
- [142] Xing, S., Tang, P. and Yang, Y.: Poly(styrene-co-maleic anhydride) Ionomers as Nucleating Agent on the Crystallization Behavior of Poly(ethylene terephthalate). *Journal of Applied Polymer Science* (2015), pp. 41240(1-12).
- [143] Xu, J., Srinivas, S. and Marand, H.: Equilibrium Melting Temperature and Undercooling Dependence of the Spherulitic Growth Rate of Isotactic Polypropylene. *Macromolecule* 31 (1998), pp. 8230-8242.
- [144] Arroyo, M., Lopez-Manchado, M. A., Avalos, F.: Crystallization kinetics of polypropylene: II. Effect of the addition of short glass fibres. *Polymer* 38 (1997), pp. 5587-5593.

- [145] Somnuk, U., Eder, G., Phinyocheep, P., Suppakarn, N., Sutapun., and Ruksakulpiwat, Y. Quiescent crystallization of natural fibers-polypropylene composites. *Journal of Applied Polymer Science* 106 (2007), pp. 2997-3006.
- [146] Mucha, M. and Królikowski, Z.: Application of DSC to Study Crystallization Kinetics of Polypropylene Containing Fillers. *Journal of Thermal Analysis and Calorimetry* 74 (2003), pp. 549-557.
- [147] Freire, E., Bianchi, O., Martins, J. N., Monteiro, E. E. C. and Forte, M. M. C.: Non-isothermal Crystallization of PVDF/PMMA Blends Processed in Low and High Shear Mixers. *Journal of Non-Crystalline Solids* 358 (2012), pp. 2674-2681.
- [148] Puente, J. A. S., Esposito, A., Chivrac, F. and Dargent, E.: Effects of Size and Specific Surface Area of Boron Nitride Particles on the Crystallization of Bacterial Poly(3-hydroxybutyrate-co-3-hydroxyvalerate). *Macromolecular Symposia* 328 (2013), pp. 8-19.
- [149] Spruiell, J. E. and White, J.: Structure Development during Polymer Processing: Studies of the Melt Spinning of Polyethylene and Polypropylene Fibers. *Polymer Engineering and Science* 15 (1975), pp. 660-667.
- [150] Hsiung, C. M., Cakmak, M. and White, J. L.: Crystallization Phenomena in the Injection Molding of Poly Ether Ether Ketone and Its Influence on Mechanical Properties. *Polymer Engineering and Science* 30 (1990), pp. 967-980.
- [151] Alvarez, V. A., Stefani, P. M. and Vázquez, A.: Non-isothermal Crystallization of Polyvinylalcohol-co-ethylene. *Journal of Thermal Analysis and Calorimetry* 79 (2005), pp. 187-193.
- [152] Pérez, C. J., Alvarez, V. A., Stefani, P. M. and Vázquez, A.: Non-isothermal Crystallization of MaterBi-Z/Clay Nanocomposites. *Journal of Thermal Analysis and Calorimetry* 88 (2007), 825-832.

- [153] Marco, C. Gómez, M. A., Ellis, G. and Arribas, J. M.: Activity of a  $\beta$ -Nucleating agent for Isotactic Polypropylene and Its Influence on Polymorphic Transitions. *Journal of Applied Polymer Science* 86 (2002), pp. 531-539.
- [154] Charoenphol, P. and Supaphol, P.: nonisothermal Melt-Crystallization Kinetics of Syndiotactic Polypropylene Compounded with Various Nucleating Agents. *Journal of Applied Polymer Science* 95 (2005), pp. 245-253.
- [155] Mileva, D., Androsch, R., Zhuravlev, E. Schick, C. and Wunderlich, B.: Isotropization, perfection and reorganization of the mesophase of isotactic polypropylene. *Thermochimica Acta* 522 (2011), pp. 100-109.
- [156] Liu, F., Guo, C., Wu, X., Qian, X., Liu, H. and Zhang, J.: Morphological Comparison of Isotactic Polypropylene Parts Prepared by Micro-Injection Molding and Conventional Injection Molding. *Polymer Advance Technologies* 23 (2012), pp. 686-694.
- [157] Sawyer, L. D., Grubb, D. T. and Meyers, G. F.: *Polymer Microscopy*. Springer, New York 2008.
- [158] N.N.: ASTM E112-10 Standard Test Methods for Determining Average Grain Size.
- [159] He, Y. and Inoue, Y.:  $\alpha$ -Cyclodextrin-Enhanced Crystallization of Poly(3-Hydroxybutyrate). *Biomacromolecules* 4 (2003), pp. 1865-1867.
- [160] Nam, J. Y., Okamoto, M., Okamoto, H., Nakano, M., Usuki, A. and Matsuda, M.: Morphology and Crystallization Kinetics in a Mixture of Low- Molecular Weight Aliphatic Amide and Polylactide. *Polymer* 47 (2006), pp. 1340-1347.
- [161] Norton, D. R. and Keller, A.: The Spherulitic and Lamellar Morphology of Melt-Crystallized Isotactic Polypropylene. *Polymer* 26 (1985), pp. 704-716.

- [162] Gupta, M. and Wang K. K.: Fiber Orientation and Mechanical Properties of Short-Fiber-Reinforced Injection-Molded Composites: Simulated and Experimental Results. *Polymer Composites* 14 (1993), pp. 367-382.
- [163] Gerard, P., Raine, J. and Pabiot, J.: Characterization of Fiber and Molecular Orientations and Their Interaction in Composite Injection Molding. *Journal of Reinforced Plastics and Composites* 17 (1998), pp. 922-934.
- [164] Feng, M., Gong, F., Zhao, C., Chen, G., Zhang, S., Yang, M. and Han, C. C.: The  $\beta$ -Crystalline Form of Isotactic Polypropylene in Blends of Isotactic Polypropylene and Polyamide-6/Clay Nanocomposites. *Journal of Polymer Science: Part B: Polymer Physics* 42 (2004), 3428-3438.
- [165] Favaro, M. M., Branciforti, M. C. and Bretas, R. E. S.: A X-Ray Study of  $\beta$ -Phase and Molecular Orientation in Nucleated and Non-Nucleated Injection Molded Polypropylene Resins. *Materials Research* 12 (2009), pp. 455-464.
- [166] Chen, Y. H., Huang, Z. Y., Li, Z. M., Tang, J. H. and Hsiao, B. S.: Simultaneous Improvement of Strength and Toughness in Fiber Reinforced Isotactic Polypropylene Composites by Shear Flow and a  $\beta$ -Nucleating Agent. *Royal Society of Chemistry* 4 (2014), pp. 14766-14776.
- [167] Causin, V., Yang, B. Y., Marega, C., Goh, S. H. and Marigo, A.: Nucleation, Structure and Lamellar Morphology of Isotactic Polypropylene Filled with Polypropylene-Grafted Multiwalled Carbon Nanotubes. *European Polymer Journal* 45 (2009), pp. 2155-2163.
- [168] Zhou, H. and Wilkes, G. L.: Comparison of Lamellar Thickness and Its Distribution Determined from d.s.c., SAXS, TEM and AFM for High-Density Polyethylene Films Having a Stacked Lamellar Morphology. *Polymer* 38 (1997), pp. 5735-5747.

- 
- [169] Popli, R. and Mandelkern, L.: Influence of Structural and Morphological Factors on the Mechanical Properties of the Polyethylenes. *Journal of Polymer Science: Part B: Polymer Physics* 25 (1987), pp. 441-483.
- [170] Fu, S. Y., Feng, X. Q., Lauke, B. and Mai Y. W.: Effects of Particle Size, Particle/Matrix Interface Adhesion and Particle Loading on Mechanical Properties of Particulate-Polymer Composites. *Composites: Part B* 39 (2008), pp. 933-961.
- [171] Mortazavian, S. and Fatemi, A.: Effects of Fiber Orientation and Anisotropy on Tensile Strength and Elastic Modulus of Shot Fiber Reinforced Polymer Composites. *Composites: Part B* 72 (2015), pp. 116-129.
- [172] O'Leary, K. and Geil, P. H.: Polymer Deformation XIII. Deformation of Thin Films of Polyoxymethylene. *Die Makromolekulare Chemie* 118 (1968), pp. 77-87.
- [173] Peng, H., Wang, B., Gai, J., Chen, J., Yang, F., Cao, Y., Li, H., Kang, J. and Xiang, M.: Morphology and Mechanical Behavior of Isotactic Polypropylene with Different Stereo-Defect Distribution in Injection Molding. *Polymer Advance Technology* 25 (2014), pp. 1464-1470.

## List of Publications

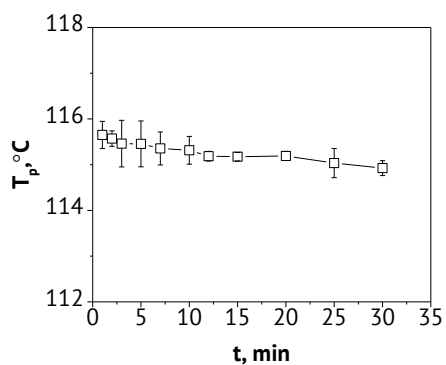
1. Suksut, B. and Schlarb, A. K.: Influence of TiO<sub>2</sub> nanoparticles on nonisothermal crystallization of PP in a wide range of cooling rates analyzed by fast scanning DSC. *Journal of Applied Polymer Science*. DOI: 10.1002/APP.43944 (2016).
2. Suksut, B. and Schlarb, A. K.: Influence of TiO<sub>2</sub> nanoparticles on crystallization of PP in a wide range of temperatures by fast scanning DSC. The 2016 International Conference on Advanced Energy Materials(ICAEM 2016), Kuala Lumpur, July 14-18, 2016. Accepted.
3. Suksut, B. and Schlarb, A. K.: Influence of nanofillers on crystallization of polypropylene at rapid cooling. *Proceeding of the Young Researchers Symposium – YRS 2016, Kaiserslautern, April 14-15, 2016*.
4. Nomai, J., Suksut B. and Schlarb, A. K.: Crystallization behavior of poly(lactic acid)/titanium dioxide nanocomposites. *KMUTNB International Journal of Applied Science and Technology, Vol.8 (2015), pp. 251-258*.
5. Schlarb, A. K., Lin, L.Y., Suwitaningsih, D. and Suksut, B.: Process-morphology-relationships of titania-filled polypropylene nanocomposites. *Proceeding of the International Conference on Advances in Civil, Structural and Mechanical Engineering - ACSM (2015), Bangkok, February 21-22, 2015*.
6. Thanomchat, S., Srikulkit , K., Suksut B. and Schlarb, A. K.: Morphology and crystallization of polypropylene/microfibrillated cellulose composites. *KMUTNB International Journal of Applied Science and Technology, Vol.7 (2014), pp. 23-34*.

7. Suksut, B. and Schlarb, A. K.: Analysis of the morphology of injection molded plates of PP/SiO<sub>2</sub>-nanocomposites. *Journal of Plastics Technology*. Vol. 10 (2014), pp. 69-85.
8. Lin, L.Y., Suksut, B. and Schlarb, A.K.: Process–structure–property relationships in semi-crystalline polymer-based nanocomposites; In: Mittal V. (ED): *Manufacturing of Nanocomposites with Engineering Plastics*, pp. 279-298. Cambridge: Woodhead Publishing, 2015. DOI: 10.1016/B978-1-78242-308-9.00012-4

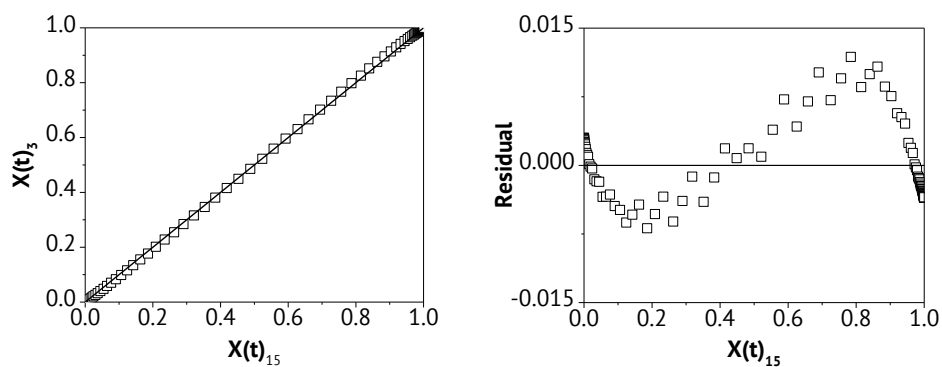
## Directed Thesis

1. Schimmelpfennig, V.: Untersuchung des morphologiebedingten Verformungsverhaltens von Nanokompositen auf Basis von Polypropylene. Bachelorarbeit, 2016.
2. Tilgner, K.: Study of the spherulite growth rate of TiO<sub>2</sub>-filled polypropylene. Studienarbeit, 2016.
3. Le Corre, R.: Study of the spherulitic development of PP nanocomposites at different cooling rates. Projektarbeit, 2016.

## Appendix



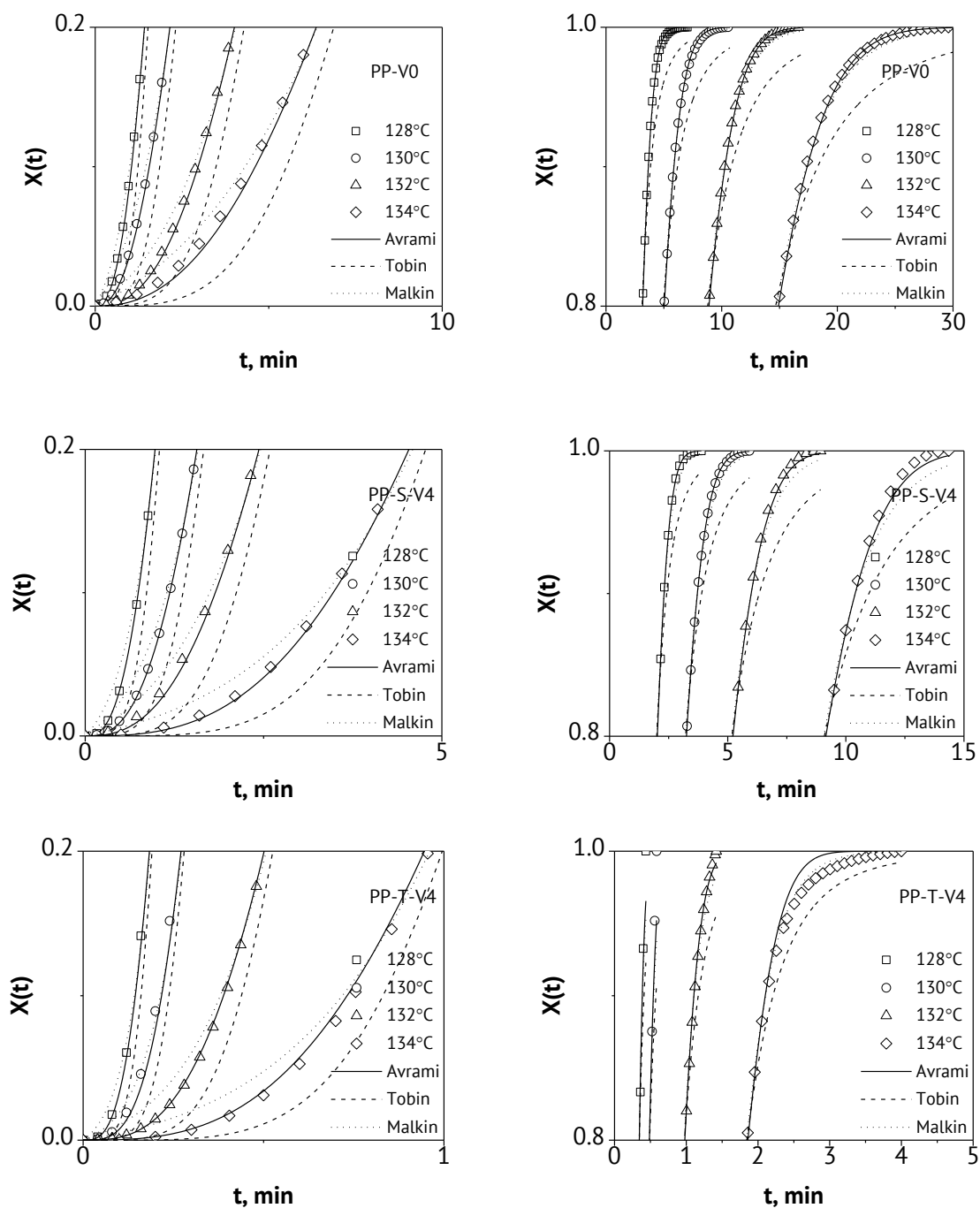
A:  $T_p$  at holding temperatures of 220°C as a function of holding time for neat PP



B: Plot of  $X(t)$  at holding time of 3 minutes versus 15 minutes at 220°C for neat PP, the experimental data, shown as square, were fitted according to a linear equation, shown as line (left). Plot of the residual versus  $X(t)$  at holding time of 15 minutes as independent variable (right).

C: Half time of crystallization of all measured PP and its nanocomposites, unit in second

T <sub>i</sub> , °C	Designation				
	PP-V0	PP-S-V1	PP-S-V4	PP-T-V1	PP-T-V4
Flash DSC					
5	0.232				
10	0.124		0.103		
15	0.073	0.050	0.070		
20	0.055	0.040	0.050	0.050	
25	0.053	0.040	0.040	0.040	
30	0.051	0.040	0.040	0.040	
35	0.053	0.040	0.040	0.040	
40	0.062	0.040	0.050	0.050	
45	0.091	0.060	0.060	0.060	
50	0.168	0.110	0.097	0.060	
55	0.216	0.160	0.130	0.050	
60	0.186	0.160	0.130	0.050	
65	0.165	0.170	0.120	0.040	
70	0.146	0.170	0.120	0.040	
75	0.135	0.150	0.120	0.040	
80	0.127	0.150	0.120	0.040	
85	0.133	0.150	0.130	0.040	0.010
90	0.152	0.160	0.140	0.050	0.010
95	0.228	0.210	0.180	0.070	0.020
100	0.389	0.350	0.280	0.110	0.030
105	0.794	0.690	0.507	0.210	0.050
110	1.730		1.030	0.408	0.103
115	3.819				0.239
120					0.689
DSC					
128	138	114	90	28	16
130	210	198	144	49	23
132	384	336	228	55	44
134	624	570	408	183	83



D: Relative crystallinity as a function of time of PP-V0, PP-S-V4, and PP-T-V4 fit with well known macrokinetic models. The left diagrams show the  $X(t) = 0$  to 0.2, and the right one show the  $X(t) = 0.8-1$ .

## E: Peak of crystallization temperature of all measured PP and its nanocomposites

$\emptyset$ , K/s	Designation				
	PP-V0	PP-S-V1	PP-S-V4	PP-T-V1	PP-T-V4
DSC					
0.03	122.2	125.1	125.9	130.3	132.6
0.08	118.4	120.7	122.3	127.2	130.0
0.17	115.9	118.1	119.3	125.6	127.8
0.33	112.7	113.8	115.4	122.8	124.8
0.67	109.2	109.8	110.9	118.7	122.1
Flash DSC					
5	105.9	105.9	106.8	115.1	119.0
10	101.8	101.8	102.7	111.5	116.2
30	93.4	92.9	94.6	106.9	111.1
50	88.8	88.7	90.0	103.8	108.4
70	85.4	85.6	86.5	101.3	106.4
100	81.1	81.1	82.0	99.3	104.0
150	76.5	76.3	76.3	96.4	101.0
200	75.0	74.7	73.3	93.5	98.6
250	73.3	73.2	71.0	91.4	96.6
300	73.0	71.8	68.3	89.2	94.8
350	72.2	70.7	66.6	87.3	93.2
400	70.7	69.2	65.5	86.3	91.8
450	70.5	68.7	65.3	84.3	90.6
500	68.8	66.0	63.9	82.6	89.2
700	66.0	62.6	62.7	77.2	84.6
1000				70.3	79.0
1500				58.6	70.5
2000				53.2	63.2
2500				50.4	56.8

F: Peak of mesophase formation of all measured PP and its nanocomposites

$\emptyset$ , K/s	Designation		
	PP-V0	PP-S-V1	PP-S-V4
Flash DSC			
100	36.7		
150	33.2		33.5
200	29.3	30.0	30.0
250	26.2	27.0	26.9
300	23.8	24.4	24.9
350	22.8	24.0	23.5
400	21.8	23.4	22.2
450	20.9	21.8	21.9
500	19.7	20.5	20.7
700	13.0		12.7

G:  $T_{cc,\alpha}$  and  $T_{cc,m}$  of all measured PP and its nanocomposites

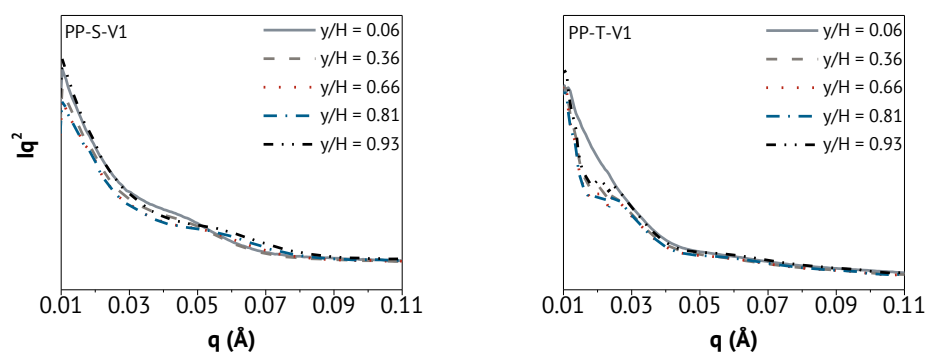
$\emptyset$ , K/s	Designation									
	PP-V0		PP-S-V1		PP-S-V4		PP-T-V1		PP-T-V4	
	$T_{cc,\alpha}$	$T_{cc,m}$								
Flash DSC										
150		107.6		105.1		107.1				
200		107.5		105.1		107.2				
250	30.6	107.4	29.8	105.4	31.0	106.6				
300	31.6	105.7	30.6	104.9	30.1	107.2				
350	31.3	105.0	31.1	103.3	31.2	104.0	28.4			
400	31.6	103.4	31.0	102.8	31.2	103.6	29.4			
450	32.0	102.7	31.4	102.5	31.6	103.1	29.4			
500	32.1	102.7	31.6	101.4	30.0	103.3	30.2			
700	33.3	103.2	33.3	102.5	33.2	103.1	31.5	99.0		
1000	34.3	103.8	32.9	102.8	34.2	103.1	32.1	99.3	34.4	
1500	34.9	103.9	33.9	102.9	34.7	103.8	33.2	101.9	34.5	
2000	34.9	103.8	34.4	102.6	35.1	103.8	34.0	102.8	35.1	
2500	35.4	105.1	35.5	104.0	35.2	104.1	34.8	103.4	36.0	103.9
3000	35.5	104.9	34.6	103.7	35.4	104.0	34.9	103.4	36.5	105.1
3500	35.5	104.7	34.8	103.6	35.6	104.5	35.0	103.7	37.0	104.7

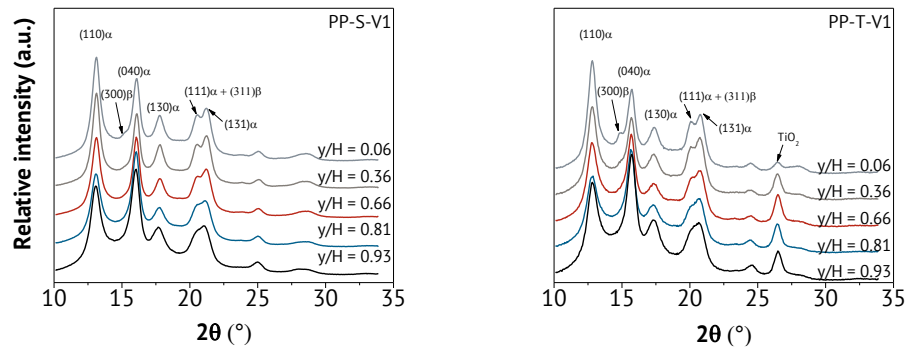
H: Crystallization melting temperature of all measured PP and its nanocomposites

$\emptyset$ , K/s	Designation				
	PP-V0	PP-S-V1	PP-S-V4	PP-T-V1	PP-T-V4
DSC					
0.03	163.8	164.6	164.9	166.3	166.6
0.08	162.7	163.9	163.8	164.9	165.8
0.17	162.4	162.9	163.7	165.1	165.6
0.33	161.7	162.4	162.7	164.0	165.1
0.67	161.3	162.5	163.2	164.0	164.4
Flash DSC					
1	153.4	151.6	152.0	155.9	158.6
5	148.1	145.0	146.4	149.1	153.3
10	144.7	142.0	143.1	146.0	150.3
30	140.0	137.7	138.9	141.9	145.8
50	138.2	135.9	137.2	139.7	143.9
70	137.2	134.9	136.1	139.0	142.6
100	135.6	133.9	135.3	138.6	141.5
150	134.8	133.1	134.1	136.6	140.4
200	134.0	132.4	133.5	136.6	140.1
250	133.6	132.1	133.1	136.5	139.3
300	133.5	131.6	132.5	135.7	139.0
350	133.2	131.5	132.5	135.4	139.2
400	132.8	131.2	132.5	135.0	138.7
450	132.9	131.2	132.3	134.0	138.3
500	132.6	130.8	132.1	134.3	138.1
700	132.4	130.8	132.0	133.5	137.9
1000	132.5	131.1	131.8	132.7	136.7
1500	132.6	131.1	131.7	132.4	135.7
2000	133.0	131.1	132.2	131.6	135.2
2500	132.7	131.3	132.1	131.8	134.7
3000	133.0	131.4	132.3	131.6	134.3
3500	132.9	131.2	132.1	131.9	134.7

## I: Tensile properties of all measured PP and its nanocomposites

Designation	y/H	Tensile strength, MPa	Elongation at break, %
PP-V0	0.06	22.4±1.3	NA
	0.36	23.9±0.5	NA
	0.66	20.5±2.2	NA
	0.81	20.0±1.1	NA
	0.93	18.8±2.6	NA
PP-S-V1	0.21	19.9±1.3	NA
	0.66	19.5±1.3	NA
	0.81	18.5±1.5	NA
	0.93	18.1±0.7	NA
PP-S-V4	0.21	18.7±1.1	28.6±8.9
	0.66	18.6±1.1	29.6±7.8
	0.81	18.0±0.9	39.5±12.0
	0.93	18.2±0.6	33.7±20.3
PP-T-V1	0.06	20.8±0.2	40.4±6.3
	0.36	20.2±1.3	30.8±5.0
	0.66	19.6±1.8	53.7±22.5
	0.81	18.0±0.5	43.8±5.1
	0.93	18.2±0.2	34.8±1.4
PP-T-V4	0.06	20.5±0.8	22.5±4.1
	0.36	20.5±1.3	22.3±5.0
	0.66	17.6±0.2	35.8±2.1
	0.81	17.6±0.8	30.2±8.9
	0.93	17.9±1.7	33.7±5.3

J: Plots of Lorenz-corrected SAXS intensity  $Iq^2$  vs  $q$  of PP-S-V1 and PP-T-V1



K: WAXD profiles of PP-S-V1 and PP-T-V1

## Curriculum Vitae

### Personal Data

Name: Buncha Suksut

### Education

06/2012-04/2015: PhD student at the Chair of Composite Engineering, University of Kaiserslautern, Kaiserslautern, Germany

05/2007-11/2009: Master of Engineering (M.Eng.), Polymer Engineering, Suranaree University of Technology, Nakhon Ratchasima, Thailand

05/2003-04/2007: Bachelor of Engineering (B.Eng.), Polymer Engineering, Suranaree University of Technology, Nakhon Ratchasima, Thailand

### Professional Experience

05/2015-07/2016: Research assistant at the Chair of Composite Engineering, University of Kaiserslautern, Kaiserslautern, Germany

### Languages

Thai, English